UNIVERSITÀ
POLITECNICA
DELLE MARCHE

PhD in Biomedical, Electronics and Telecommunication Engineering
Department of Information Engineering
Università Politecnica delle Marche
Ancona, Italy, 2022

Modern techniques to process micro-Doppler signals from mmWave Radars

Candidate
Gianluca Ciattaglia

Thesis Advisor
Prof. Ennio Gambi

"Remember that all models are wrong; the practical question is how wrong do they have to be to not be useful."

George Box

Abstract

mmWave Radar systems are becoming very common on vehicles and their capabilities, in terms of range and velocity, make them suitable for another classical radar application, the one related to the micro-Doppler effect.
From the processing of mmWave radar signals, the micro-Doppler effect can be exploited, making so possible to extract interesting information on the observed targets. With the huge bandwidth and the short signal transmission time, the micro-Doppler effect can be used for different purposes such as target vibration measurements or targets classification.
Thanks also to the advance of Machine Learning techniques, their combination with radar signal processing is an interesting field to explore and can be used to provide solutions to different radar problems.

The Micro-Doppler effect has a long story in Radar systems, a lot of literature can be found on this topic but most of them consider non-commercial devices so is quite away from a practical case. In this dissertation, different techniques to process the micro-Doppler signals coming from automotive radars will be presented, with the purpose of classifying them and extracting vibration information from the target. The main contribution of this work is the proposal of novel techniques that can be applied on a commercial sensor and makes them suitable for the micro-Doppler application.

Contents

List of Figures

List of Tables

1
Introduction

Advanced Driver Assistance Systems (ADAS) is one of the main research tasks in automotive technology, that has provided more powerful sensors and Frequency Modulated Continuous Wave (FMCW) Radars are one of them. To perform good measurements and support assistance systems, Radars need huge bandwidth and small Chirp Repetition Time (CRT) but these features can be powerful also to extract micro-Doppler (mD) signals. To understand how is possible, first of all, the mD must be introduced, only at this point why such sensors are useful in mD applications can be discussed [1].

In this chapter, I will review the:

- Introduction to micro-Doppler effect;
- 77 GHz FMCW Automotive Radar sensors;
- Common techniques to extract range, velocity and angle of arrival in automotive Radars.

1.1 Introduction to micro-Doppler effect

Radar systems can detect the velocity of a target thanks to the Doppler effect, this is a frequency shift in the echo signal and is directly related to the target's velocity. In general, a target, is not an ideal "point" but is composed by different parts, such as propellers for a drone or legs for a human, these produces an effect called mD which is a distinctive characteristic of that particular target.The micro-movements of these parts produce an additional Doppler shift which is the mD effect. This signature can be used in military or civilian applications to discriminate targets, identify human motion and many others. The mD effect can be observed with many Radar modulation schemes, the most simple is for example the Continuous Wave (CW). In this case, no modulation is added to the signal and the Radar

transmits continuously, the echo is then multiplied with the source and the mD can be extracted. Also with Automotive FMCW radars is possible to extract mD signatures and this is one task in this dissertation.
Many examples of applications can be found in literature, in [2, 3, 4] the effect used to study and identify different types of aircraft and drones while in [5, 6, 7] to study human behaviours. For the purpose of this work we introduce the modeling of the mD in two particular cases:

- The effect generated by a vibrating target;
- The effect generated by a target who is moving in front of the Radar.

Starting from how the mD appears in the echo generated by a vibrating target, it is possible to resort to the model described in [1, 8]. We can consider a situation likes the one depicted in Fig. 1.1.

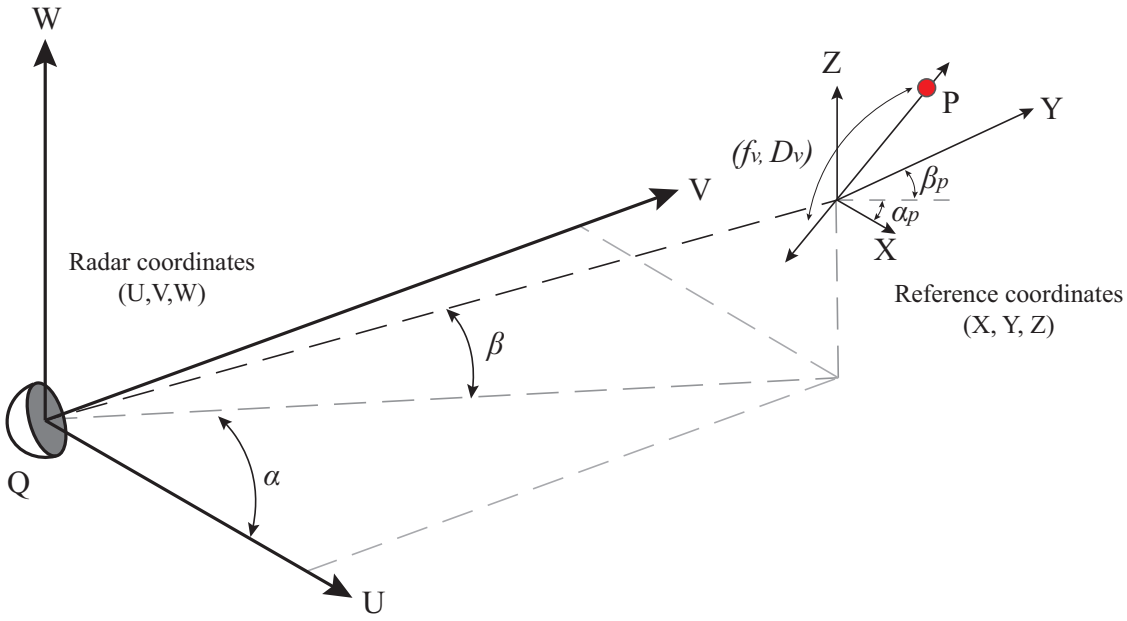

Figure 1.1: Example of a Radar and a vibrating point target. The Radar is situated in position Q, and the target in P.

The mathematical model can be derived from the classical Doppler formulation and the Radar can detect vibrations only along a radial direction. For the sake of simplicity, we suppose that the target vibrates only in this direction with a main vibration frequency f_v and a displacement D_v. In general, for a real vibrating target, the frequency is not a single tone but, it is possible to use a simplified model. Accordingly with [1], supposing the angles β and α_p zero we can model the displacement $D(t)$:

$$D(t) = D_v sin(2\pi f_v t) cos(\beta) cos(\alpha_p) = D_v sin(2\pi f_v t) \tag{1.1}$$

The angles β and α_p represent, respectively, the elevation angle of the Radar system with respect to the plane (U,V), and α_p is the radial direction of the displacement. If we denote by R_0 the distance between the Radar and the target, the range distance

can vary according to the law $R(t) = R_0 + D_v(t)$. At this point, the received signal becomes:

$$s(t) = \rho \cdot exp[j(2\pi f_0 t + 4\pi \frac{R(t)}{\lambda})] = \rho \cdot exp[j(2\pi f_0 t + \Psi(t)] \tag{1.2}$$

where ρ is the backscattering coefficient, f_0 is the carrier frequency and λ is the wavelength. As defined above, $R(t)$ is the displacement of the target so it is possible to substitute these terms inside equation 1.2, and the result is a new formulation of $s(t)$:

$$s(t) = \rho \cdot exp[j(4\pi \frac{R_0}{\lambda}) \cdot exp[j2\pi f_0 t + D_v sin(2\pi f_v t) \cdot \frac{4\pi}{\lambda}] \tag{1.3}$$

The equation is composed by two terms, the former is related to the main distance of the target R_0, the latter is related to the vibrational movement of the target. It is now easy to extract the phase of this signal and evaluate the mD part of the total Doppler effect. By indicating the quantity $2\pi f_v$ with ω_v, it is possible to re-write the micro-Doppler expression as:

$$f_{mD} = \frac{\omega_v D_v}{\pi \lambda} cos(\omega_v t) \tag{1.4}$$

As specified above, this model doesn't take into account the direction of the vibrations. In a more general model, β and α_p, are not zero and the equation must include also these terms. But for the aims of this work, it is enough to understand the principle of the vibration analysis performed with a Radar system. At this point, it is possible also to understand how the wavelength plays a key role in the detection of small vibrations. This parameter identifies the vibration resolution capability of the system: an higher carrier frequency provides a better displacement resolution. For example, by using a mmWave Radar it is possible to detect vibrations with a displacement in the order of microns.
In the case of a more generic moving target composed of different parts, such as a drone or a person, the modeling can be more complex. Each element can produce a mD component accordingly the movement models described in [1] and the result is the sum of them. The mD model can be in this cases extracted in different ways: in [9, 10] the target is modeled as a series of points and the related mD is derived applying Doppler models on each point. A comparison between simulations and real Radar data can be found in [11].
In general in these cases the most simple way to analyze the mD is to extract them from the Radar signal and apply processing techniques to extract information or performing a target classification.

1.2 77 GHz FMCW Automotive Radar sensors

Autonomous driving is an important task in future vehicles, most manufacturers have invested a lot in its development. The Society of Automotive Engineers (SAE) has classified the autonomous driving systems into five levels and that are:

- Level 0: No Driving Automation;
- Level 1: Driver Assistance;
- Level 2: Partial Driving Assistance;
- Level 3: Conditional driving Automation;
- Level 4: High Driving Automation;
- Level 5: Full Driving Automation.

A full description on the meaning of each level can be found in [12, 13, 14]. Autonomous driving will involve sensor like Lidars, Global Positioning System (GPS), Cameras and Radars and an overview on their coverage area can be found in Fig. 1.2.

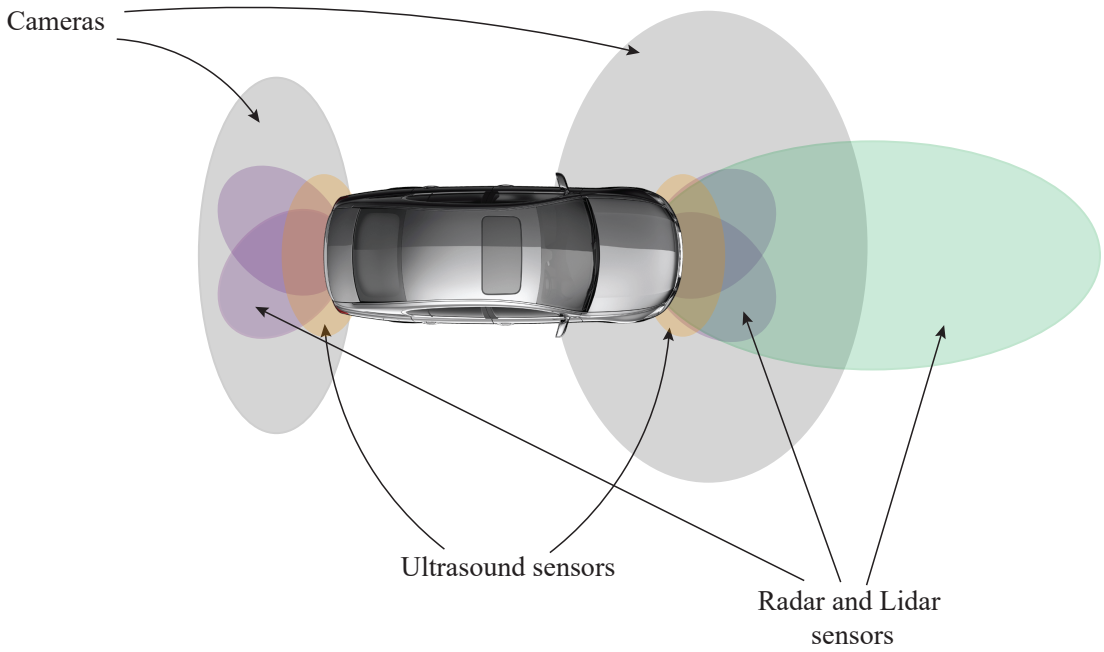

Figure 1.2: Overview on ADAS sensors.

One of the most important sensors in the development of these technologies is the FMCW Radar who, by following the European Telecommunications Standards Institute (ETSI) regulation works at 79 GHz [15]. The interest of the automotive market in Radar sensors makes it possible to find in the market very interesting Radars with a small form factor and very powerful capabilities. This makes them interesting also for other applications, such as the one related to the mD.
Radar is a device that uses electromagnetic waves to determine the location of objects by performing operations on received reflected waves. The term Radar is an acronym for radio detection and ranging [16, 17] and a basic scheme of a mono-static Radar sensor is depicted inside Fig. 1.3.

The transmitted signal is generated by a waveform generator and in the receiving process is combined with the received one to obtain the target position or velocity. In most applications, the Radar should be designed to meet specific performance requirements. These requirements include the maximum range, range resolution, maximum velocity, velocity resolution, the covered field of view in the angular space,

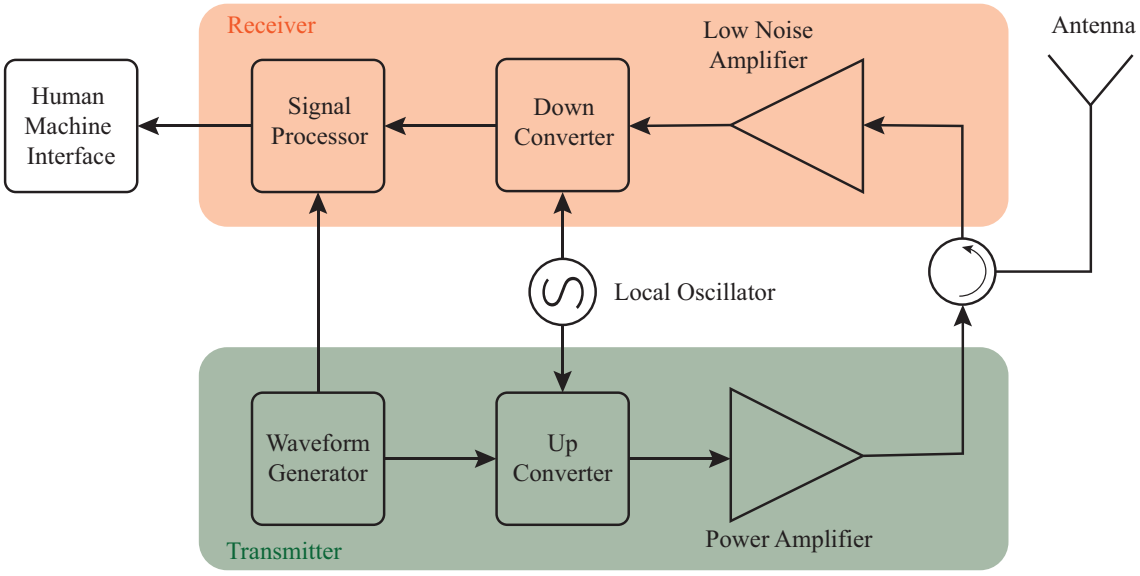

Figure 1.3: Components of a simplified mono-static Radar system.

and many other additional demands. The same requirements are also placed on the Radar in automotive applications. To meet these system requirements, the fundamental performance characteristics are determined by what is referred to as the Radar equation [16]. The amount of collected power can be modeled as:

$$P_r = \frac{P_t G_t G_r \lambda^2 \sigma_s}{(4\pi)^3 R^4} = \frac{P_t G_t A_e \sigma_s}{(4\pi)^2 R^4} \tag{1.5}$$

where P_r is the received power, P_t the transmitted power, λ the wavelength of the transmitted signal, σ_s the Radar Cross Section (RCS) of the target, R the distance of the target, G_t and G_r the gains of the transmitter and receiver antennas, $A_e = \frac{G_r \lambda^2}{4\pi}$ is the effective aperture of the receivers' antenna. By reverting the formula is possible to calculate the maximum detectable range where the minimum detectable power by the receiver can be indicated as S_{min}.

$$R = \sqrt[4]{\frac{P_t G_t A_e \sigma_s}{S_{min}(4\pi)^2}} \tag{1.6}$$

Both equation 1.5 and 1.6 are valid in all Radar system so also in FMCW and must take into account during the sensor development. A basic classification of automotive Radars can be done on the range detection capability and this is reported inside Tab. 1.1, [18, 19].

Table 1.1: Classification of automotive radars based on range measurement capability.

Radar Type	Long-Range Radars	Medium-range Radars	Short-Range Radars
Frequency Band [GHz]	76 - 77	77 - 81	77 - 81
Bandwidth [MHz]	600	600	4000
Range [m]	10 - 250	1 - 100	0.15 - 30
Azimuthal feld of view [deg.]	±15	±40	±80
Elevation feld of view [deg.]	±5	±5	±10
Example Applications	Automotive cruise control	Lane change assist	Park assist

1.2.1 FMCW Automotive Radar sensor

To understand how an FMCW Radar works, we can start from the block scheme, which is depicted inside Fig. 1.4.

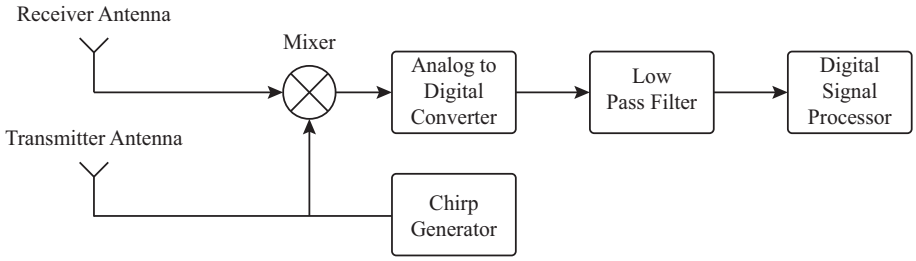

Figure 1.4: FMCW Radar block scheme.

FMCW Radars transmit signals called chirps, these signals change their frequency over time. This modulation scheme is an evolution of the CW Radars who transmit only not modulated signals (a sinusoid) and are not able to estimate the distance of a target. In linear chirp signals, the frequency change linearly with time so we can have up-chirp when the slope is positive and down-chirp when is negative, in the case of automotive Radars only up-chirps are present. The received signal is then multiplied by the mixer with the received one and the result is sampled by an analog-to-digital converter (ADC) after a low-pass filtering. The sampled signal is called the Beat signal and on them is possible to perform computations able to extract Range targets distances, velocities, and also Angle of Arrival (AoA). The mixing operation and the obtained Beat signal are summarized in Fig. 1.5.
The Beat signal can be calculated only in the overlap area of the transmitted and received signal, their frequency is strictly related to the round trip of the signal so from the Echo Delay. If we suppose an ideal condition where only one target is present, the Echo Delay provides a Beat signal with a frequency derived from:

$$f_B = f_2 - f_1; \tag{1.7}$$

The mixing operation generates also the sum component but this can easily be filtered out. All the targets present in the observed area can generate an Echo so the Beat signal in a real environment is the sum of all the f_B generated from each one. As the Echo delay can be written as $\tau = 2R/c$, where R is the target distance

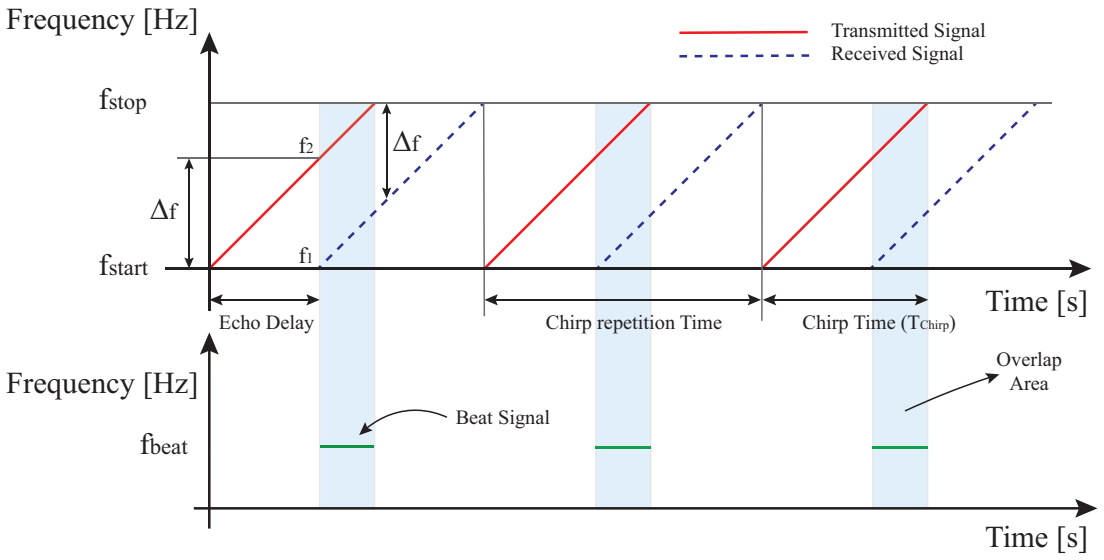

Figure 1.5: Chirp Transmission scheme.

and c the speed of light, we can model the Beat signal in terms of transmitted signal parameters [20, 18]:

$$f_B = \frac{2R\Delta_f}{cT} + f_D \tag{1.8}$$

where T is the sampling time, Δ_f the difference bandwidth and we can also indicate the slope of the chirp frequency as $Slope = \Delta_f/T$. The Doppler shift f_D can be calculated as function of the velocity v:

$$f_D = \frac{2v}{\lambda} \cdot cos\psi \tag{1.9}$$

We need the term $cos\psi$ in order to take into account only radial velocity components. From equation 1.8 we can see a fundamental parameter which is T, if we decrease this value we can sample higher Beat frequency so the sensor can detect a longer range. This is a practical limit in our devices; remembering equation 1.6, not only S_{min} is important but also T. Is possible to receive a power bigger than S_{min} but if we not sample with a correct value we can detect only targets in a lower range. The Beat signal can be now modeled as [21]:

$$s(t,l) = exp(j2\pi(f_B t - f_D \cdot l \cdot T_{Chirp} + \phi) \tag{1.10}$$

where t is the time, also called fast-time, l the chirp number, T_{Chirp} is the chirp duration and ϕ the signal phase. To calculate the distances of the detected targets we can perform a Fast Fourier Transform (FFT) on the complex samples coming from the ADC. This computation reveals all the frequency components of the Beat signal and each one is related to a range distance. An example of this result is depicted inside Fig. 1.6. Referring to Fig. 1.5, the FFT is computed for the samples of the Beat signal collected in the overlap zone. On this computation, many aspects can be discussed, for example, the ones related to the resolution capability. These topics are outside our discussion as this introduction wants only to provide basic

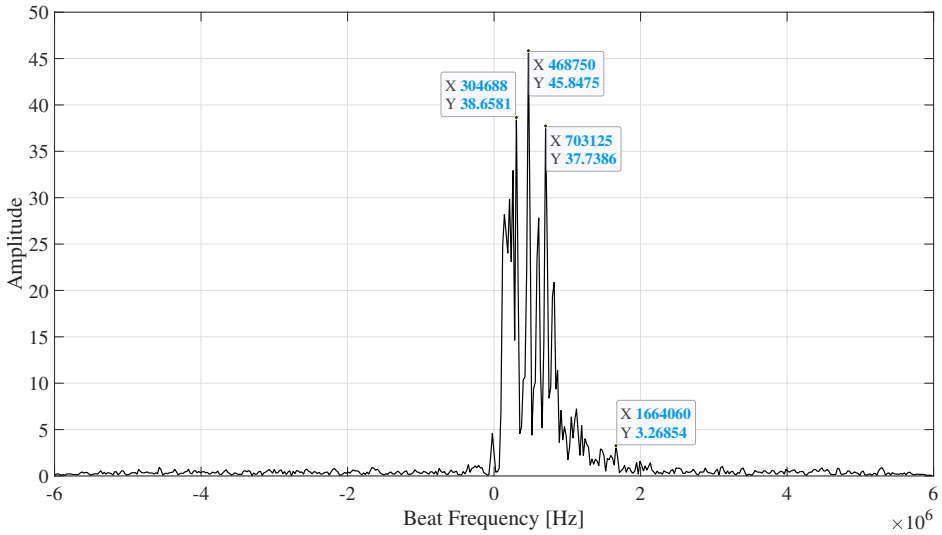

Figure 1.6: Example of FFT used to calculate the target distances.

concepts useful to understand the work we did. An exhaustive, deeper discussion can be found in [22, 23, 24]. The conversion from frequency to range (R) follows:

$$R = \frac{f_B c}{2Slope} \tag{1.11}$$

where following the Nyquist theorem the maximum detectable Beat frequency f_B can be $f_{sampling}/2$ with $f_{sampling}$ the sampling frequency of the ADC. Of course the negative part is a result of the computation and can be neglected.
The other parameter which can be calculated is the velocity, this can be revealed only by observing two or more adjacent chirps as the Doppler effect changes the argument of the signal, described by equation 1.10, from a chirp to another. To calculate the velocity, a common procedure is to collect the samples of the Beat signal inside a matrix and perform a bi-dimensional FFT on them [25, 26]. A schematization of the procedure can be found in Fig. 1.7.
In general Automotive Radars transmit frames of chirps, this contains a certain number of chirps useful to calculate the range and the velocity information. As depicted inside Fig. 1.7, the time axis along the rows is called slow-time and each bin has a duration of a chirp time. To obtain the velocity is possible to convert the "slow-time frequency" with the relation:

$$v = \frac{f_{slow-time} \cdot \lambda}{2} \tag{1.12}$$

An important performance criterion is the resolution or separability of speed and distance between two targets. From [27], the distance resolution Δ_R and velocity resolution Δ_v can be calculated with:

$$\Delta_R = \frac{c}{2\Delta_f} \tag{1.13}$$

$$\Delta_v = \frac{\lambda}{2T} \tag{1.14}$$

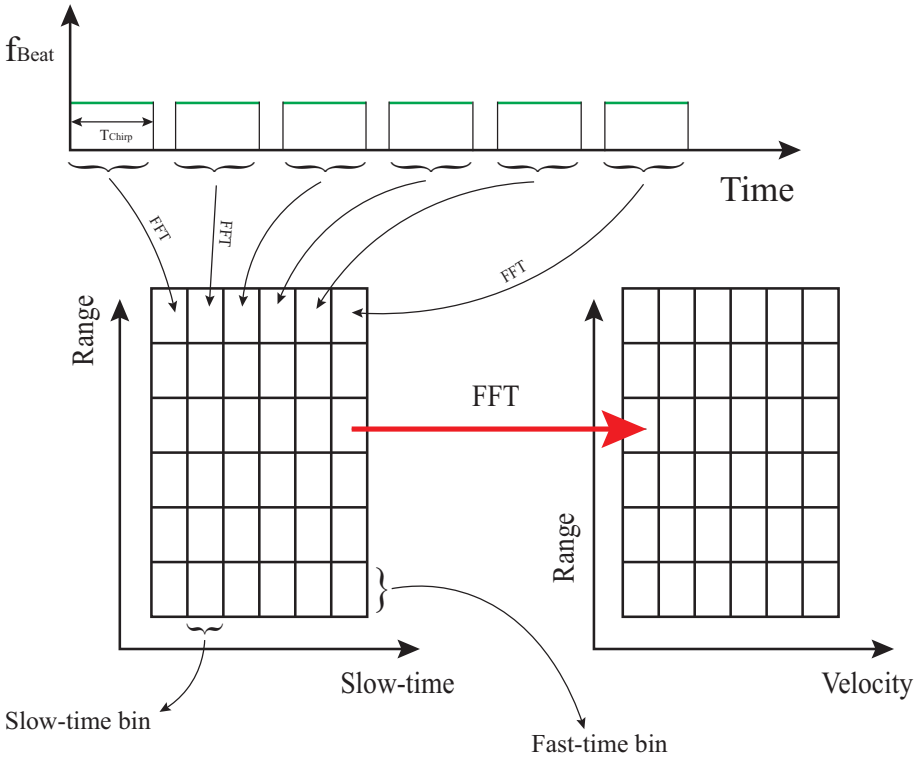

Figure 1.7: Calculation procedure of the range-Doppler map.

With a bigger bandwidth Δ_f we have a smaller Δ_R, which means that the range resolution capability can be improved by using a bigger bandwidth as Δ_R decrease. These two parameters are inverse-proportional related, a bigger resolution capability means a lower value of Δ_R. The same thing is true for the velocity resolution, is possible to increase this Radar capability by using a longer chirp time T. In real devices the *Slope* is limited so to obtain a bigger Δ_f we must increase the T but this leads to a lower Δ_v and vice versa. This is a compromise due to the commercial devices considered in our work.

The last parameter that can be derived is the AoA, this can be obtained by exploiting the MIMO technology. A basic scheme of an FMCW MIMO Radar can be found in Fig. 1.8.

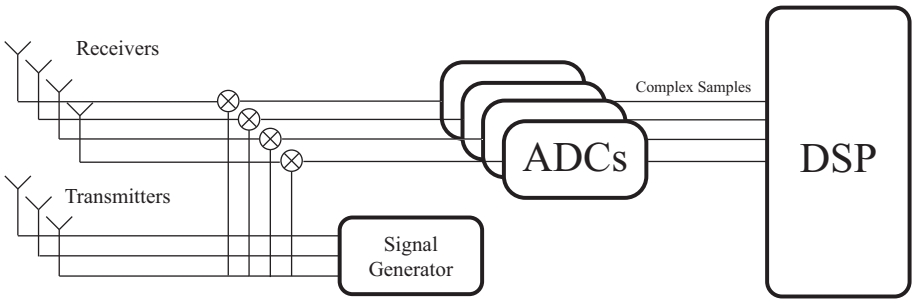

Figure 1.8: MIMO Radar block scheme.

The basic idea is to measure the phase difference between signals at a receiver array.

This is possible by performing an FFT along the spatial axis, using the signals' samples. In Fig. 1.9 this principle is depicted by using two receiver antennas and two transmitters. It is important to specify that the target must be in far-field so the paths travelled by the reflected signals can be considered as parallel [28, 29].

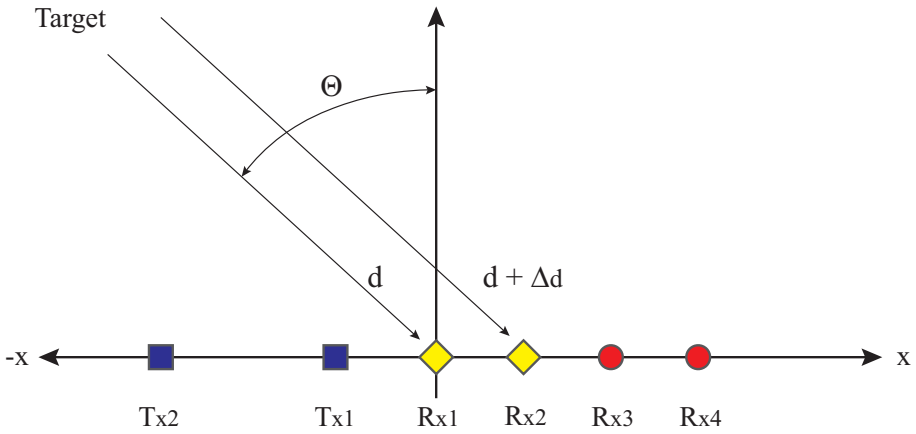

Figure 1.9: Generic 2×2 MIMO antenna of an automotive radar system. The blue squares are the transmitters, the yellow diamonds the receivers, and the red circles the virtual elements of the array.

In Fig. 1.9 only the transmitters and the Rx1 and Rx2 receivers are real elements of the antenna; Rx3 and Rx4 are virtual elements. The phase difference Δ_ϕ at each receiver antenna depends on the distance Δ_d between the elements and can be calculated from:

$$\Delta_\phi = \frac{2\pi\Delta_d}{\lambda} \tag{1.15}$$

The Δ_ϕ changes if the transmitter is Tx1 or Tx2, so, considering the receiver elements spaced by a distance of $\lambda/2$, and Tx2 at a distance of λ from Tx1, the Δ_ϕ at Rx1 is 0 when Tx1 transmits, and $2\Delta_\phi$ when Tx2 transmits. The same happens for Rx2, where the phase difference is Δ_ϕ when Tx1 transmits, and $3\Delta_\phi$ when Tx2 transmits. For this reason it is possible to extend the MIMO array with two additional elements, and the new array is called Virtual Array. The elements Rx3 and Rx4 are virtual and generated by the phase delay. This way, it is possible to improve the angular resolution, but with a smaller antenna.
As described in [30], for a target with an angle of arrival equal to Θ, the reflected signal arriving at the receivers has a spatial frequency equal to:

$$\omega_1 = \frac{2\pi d sin(\Theta)}{\lambda} \tag{1.16}$$

A second target can have the same spatial frequency but the sine argument is $(\Theta + \Delta_\Theta)$ so the difference between these two spatial frequencies can be calculated as:

$$\Delta_\omega = \omega_1 - \omega_2 = \frac{2\pi d}{\lambda}(sin(\Theta + \Delta_\Theta) - sin(\Theta) = \frac{2\pi d}{\lambda}(cos(\Theta) \cdot \Delta_\Theta) \tag{1.17}$$

These two spatial frequencies are separated by Δ_Θ and this value is visible inside the FFT computation. The number of points used in the FFT depends on the number of

virtual elements. The radar condition to resolve two targets in the angular domain is:

$$\Delta_\omega > \frac{2\pi}{N} \Rightarrow \frac{2\pi d}{\lambda}(cos(\Theta) \cdot \Delta_\Theta) > \frac{2\pi}{N} \Rightarrow \Delta_\Theta > \frac{\lambda}{Ndcos(\Theta)} \tag{1.18}$$

where N is the number of virtual elements of the receiver antenna. The presence of $d \cdot cos(\Theta)$ means that the angular resolution capability of the sensor decrease if we look towards the sides of the array. For such simplicity, we can consider $\Theta = 0$, but the model can be considered valid only at the boresight line. In general, the receiver antenna elements are spaced by a $\lambda/2$ distance so, at the end, the angular resolution for an FMCW MIMO radar is:

$$\Delta_\Theta = \frac{2}{N} \tag{1.19}$$

Observing equation 1.19 it is possible to understand why the use of the MIMO technique is important. In order to attain better angular resolution, the device needs more receiver elements, but this is a drawback in terms of physical dimensions of the device. By implementing MIMO, it is possible to improve the virtual elements of the array while maintaining a small form factor at the same time. There are a lot of algorithms that can be used to increase the angular resolution without increasing the number of antennas, this is an interesting field of research and we refer to literature for a better deepening [31, 32, 33].

As a conclusion, an Automotive MIMO Radar for each transmitted frame generates a so-called datacube [34, 35], whose axis are the fast-time, the slow-time, and spatial sampling provided by the MIMO. The computation of a 3D-FFT gives us the information about range distance, velocity, and AoA. The final target identification in terms of these three parameters can be obtained applying the Constant False Alarm Rate (CFAR) threshold. Again is not a purpose of this work to provide informations on this technique and some review on the argument can be found in [36, 37, 37, 38].

1.2.2 AWR1642 setup and configuration

In this section, we will discuss how a real automotive FMCW Radar device works and in particular the AWR1642 of Texas Instruments [39]. All the work described in the next chapters is based on this sensor so when we will refer to the system calling them “radar system” or “sensor” we will refer only to this device. Also the setup configuration is the same so will be described only in this section.
The AWR1642 is a Frequency Modulated Continuous Wave (FMCW) Radar that utilizes waves in the frequency span of 76 - 81 GHz, with a maximum bandwidth of 4 GHz. It is designed to work from 76 to 77 GHz for long-range applications and from 77 to 81 GHz for short-range applications. Is equipped with two transmitters and four receivers so is possible to obtain a receiver virtual array composed of eight elements. The board equipped with the AWR1642 sensor is depicted inside Fig. 1.10. The AWR1642 contains not only the radio frequency frontend but also the Digital Signal Processor (DSP) and the Micro Controller Unit (MCU) as the system is

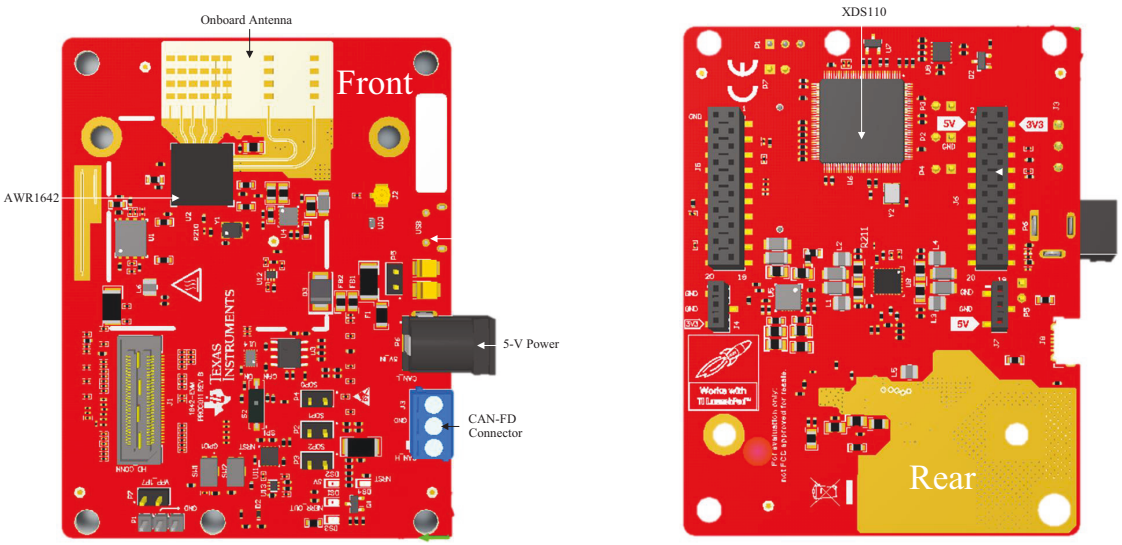

Figure 1.10: AWR1642 development board.

designed to be a single-chip device. Signals coming from the antenna array are pre-processed in the board and for this reason, it is impossible to access the raw collected data. By using a Field Programmable Gate Array (FPGA) equipped daughterboard, called DCA 1000 EVM [40], we can gain access to raw samples extracted from the Beat signal too. The daughterboard connects to the Radar using a Low Voltage Differential Signaling (LVDS) bus, and to a computer using an Ethernet connection. The samples are sent with User Datagram Protocol (UDP) and in this way, we can process raw data on a workstation in order to extract the relevant information. A block scheme of the complete Radar system is depicted in Fig. 1.11.

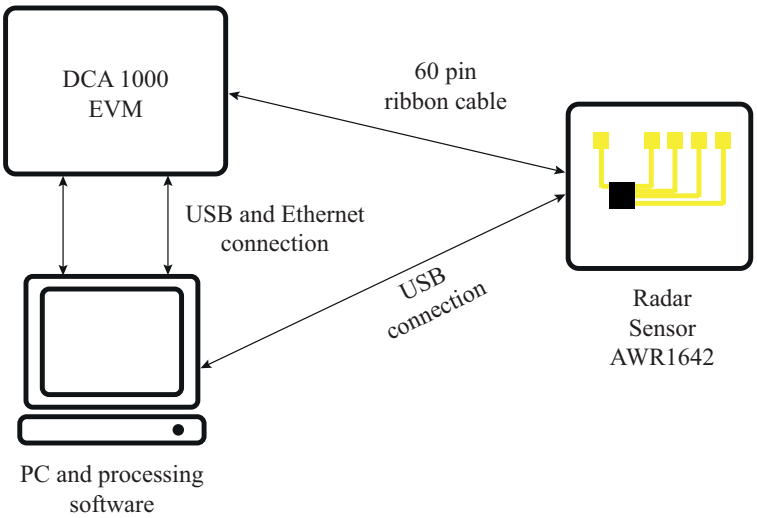

Figure 1.11: Block diagram of the AWR1642 Radar system

The configuration of the sensors and the DCA1000 can be done with a proprietary software provided by Texas Instruments and called mmWave Studio [41]. The main configuration requires the setup of the chirp generation, as we mention in the pre-

vious section this type of sensors transmits in general only up-chirps so the main parameters are related to this signal.

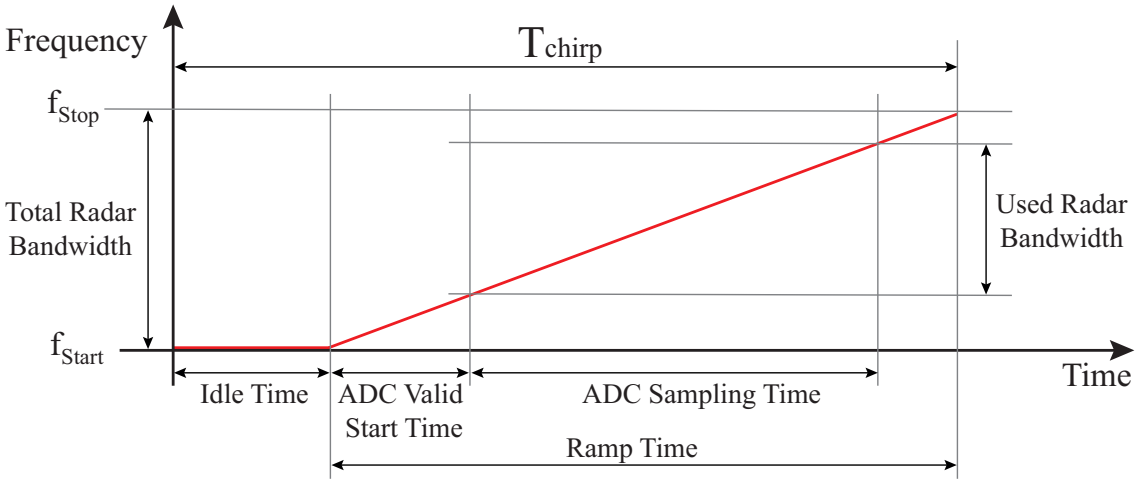

Figure 1.12: Chirp time graphical representation.

Fig. 1.12 shows how the sensor generates the chirps and the description of the parameters follows:

- Idle Time: time required for the ramp generator to return to its original state;
- ADC Valid Start Time: idle time used to remove data at the very beginning of the ramp. The ramp generator at the beginning is not linear and this produces a distortion in the beat signal. We neglect these samples to avoid distortions;
- ADC Sampling Time: the amount of time during which ADC samples the beat signal. In this time duration, we can introduce a configurable number of samples accordingly to the sampling frequency of the ADC;
- Used Radar Bandwidth: effective Radar bandwidth after the initial part of the ramp has been removed.

Frames are used to organize chirps transmission. Each frame can contain at least 1 chirp up to a maximum of 255. Fig. 1.13 shows how chirps are transmitted in time.

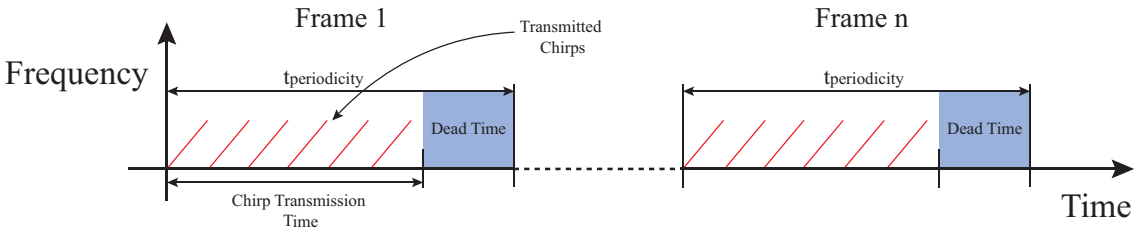

Figure 1.13: Chirps transmission within frames.

In Fig. 1.13, we can see the transmission scheme used by the sensor, this is valid only for this particular device, maybe other automotive radars use different working mode. The device transmits inside what we call "Chirp Transmission Time" and after that, there is a sort of "Dead Time" useful for example for processing the

datacube [42]. This parameter can be controlled by the user during the configuration of the device. Inside the Chirp Transmission Time, the sensor can transmit with both antennas following the configured transmission scheme. The total frame duration is called $t_{periodicity}$ and is a parameter who can be set from mmWave Studio.

This is a brief introduction to the Radar system used to perform the work described in the next chapters. Only a the end we propose a comparison with a different sensor but is also an FMCW radar so the rules described in 1.2.1 remain valid.

1.3 Thesis Contribution

The contribution of this dissertation is on the study of different signal processing techniques, able to extract information from mD signals. This processing is focused on two different applications:

- Classification of things based on mD features extraction;
- Object's vibrations detection with the mD effect.

The developed methodologies are based on commercial radar sensor, the one described in this chapter, making these topics more suitable for an industrial application. Also, the obtained performances are in line or even better than other works found in the literature. As the proposed techniques are based on a commercial device, the work we did is more suitable for an industrial application.

2

Application of Machine Learning to micro-Doppler Signals

From chapter 1 we know how the mD is an effect independent from the Radar technology and their extraction can be done with different signal processing techniques. Examples on how mD can be used with Ultra Wide Band (UWB) and CW radars can be found in [43, 44, 45, 46]. In mmWave FMCW Radars, the mD can be extracted in two ways and these methods will be discussed in this chapter. For a classification problem, modern Machine Learning (ML) algorithms provide a very powerful tool, there are many ways to extract features and classify signals with different performances and computational costs.
In this chapter different developed pipelines will be presented and their performances in different contexts will be discussed.

2.1 FMCW signals pre-processing

In chapter 1 we describe how the sensor sample the Beat signal and the radar system sends this information to a computer. As the sensor is suited with four receivers, the beat signals are at maximum four and are referred to the MIMO configuration of the device. To process and classify the mD only one beat signal can be used, but by summing together the four-receiver lines we can improve the signal-to-noise ratio and reach better performances. After this, the samples are reorganized in a form of a complex matrix where along the rows are stored the samples of a single chirp and along the columns the samples of different chirps. The obtained matrix contains the samples of the global acquisition. This preliminary step is depicted inside Fig. 2.1.

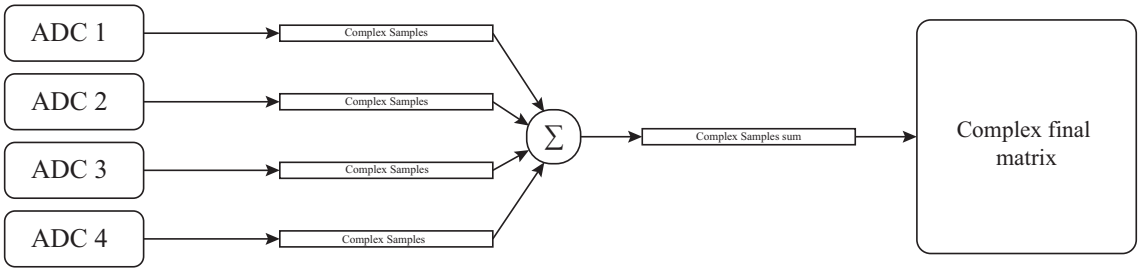

Figure 2.1: Pipeline used to obtain the initial complex matrix.

The original mD information can be stored in two different types of matrices, in one

the information is compressed along the time, this is called range-Doppler map of the global acquisition; in the other the compression is made along the range, the information is extracted with a Short Time Fourier Transform (STFT) and is stored in a Doppler-time map. Both approaches can be used to solve the classification problem.
To calculate the range-Doppler map[1], we can use a bi-dimensional FFT. This process is summarized inside Fig. 2.2.

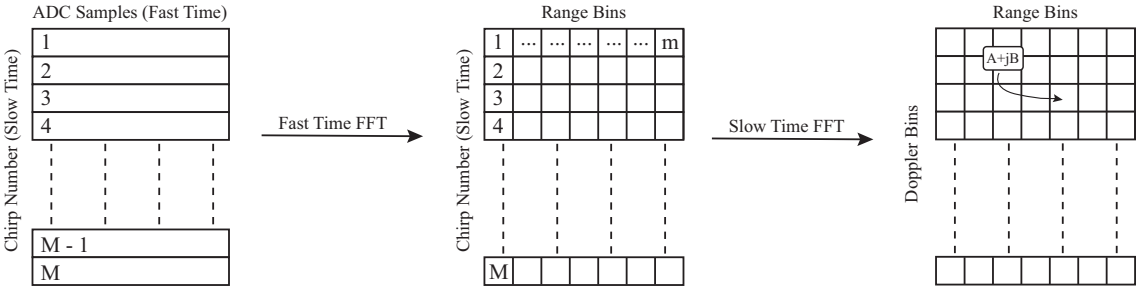

Figure 2.2: Calculation process of the range-Doppler map.

The mathematical model of this computation follows the equation:

$$R_D = \left| \sum_{m=0}^{M} \sum_{n=0}^{N} r[m,n] \cdot \exp\left(-j2\pi \left(\frac{mk}{M}\right)\left(\frac{nl}{N}\right)\right)\right|, \tag{2.1}$$

where $r[m,n]$ represents the elements of the data matrix, m and k are the indexes going from 0 to $M-1$, and n and l indexes from 0 to $N-1$, being M the number of fast time elements, while N is the number of slow time elements.
In the second map, the process is a little bit different, but the starting complex matrix is the same. To obtain the Doppler-time map, the fast-time axis must be along with the columns, and the slow-time along the rows, and the first step is performing a FFT along the fast-time. This process produces a range-time map and an example is depicted inside Fig. 2.3.
Starting from this map is possible to calculate a STFT which is the most common time-frequency representation [47], along the slow-time. The STFT can be obtained from the following equation:

$$STFT_x[k,n] = \sum_{r=-\infty}^{+\infty} x[r]w[n-r]e^{-j2\pi rk/N},\ k = 0, 1, \cdots, N-1, \tag{2.2}$$

where n represents a discrete index of time, k is a discrete index of frequency and $w[\cdot]$ is a window function. The STFT can in fact be considered as the Fourier transform of a signal multiplied by a window sliding over time. A trade-off between resolution in time and in frequency must be found, and overlapping the windows can help as this process try to stretch the time to improve the frequency resolution [48]. The process to obtain this second type of map is depicted in Fig. 2.4.

[1]We will use this name for the rest of the chapter to indicate the global range-Doppler map obtained from one acquisition.

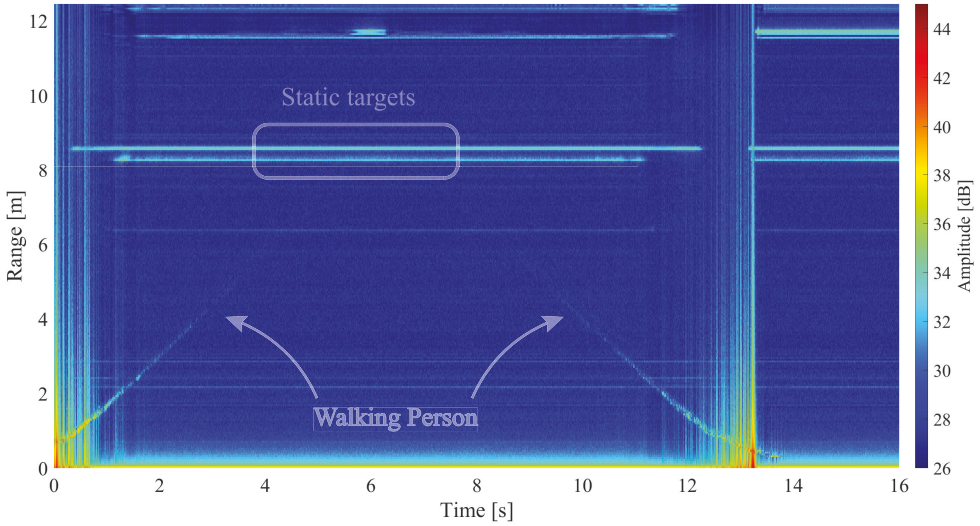

Figure 2.3: Example of range-time map for a walking person.

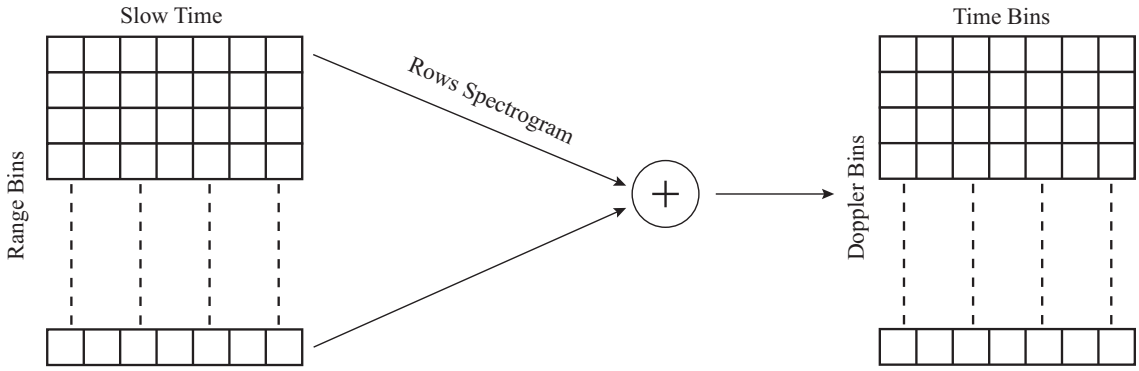

Figure 2.4: Calculation process of the Doppler-time map.

The STFT is performed in each row of the range-time map, this process produce a matrix which represent the collected mD at each distance. Summing together the obtained matrices we obtain the Doppler-time map of the global acquisition. The computation is performed for each range bin because we don't know exactly where the target is. As we want to create a more general algorithm that can be applied in each situation the best choice is to sum all the STFT obtained at each range bin, the result will be a sum of all the mD signals for each range value inside the setup.

Both range-Doppler and Doppler-time maps are composed by complex numbers and to obtain a "picture" where we can extract features, we must compute the module. Each classification operation will be performed in figures which contains only the module information. An example of these results, for a waking person, can be found in Fig. 2.5a and Fig. 2.5b.

From this starting point we can discuss how to classify mD signals.

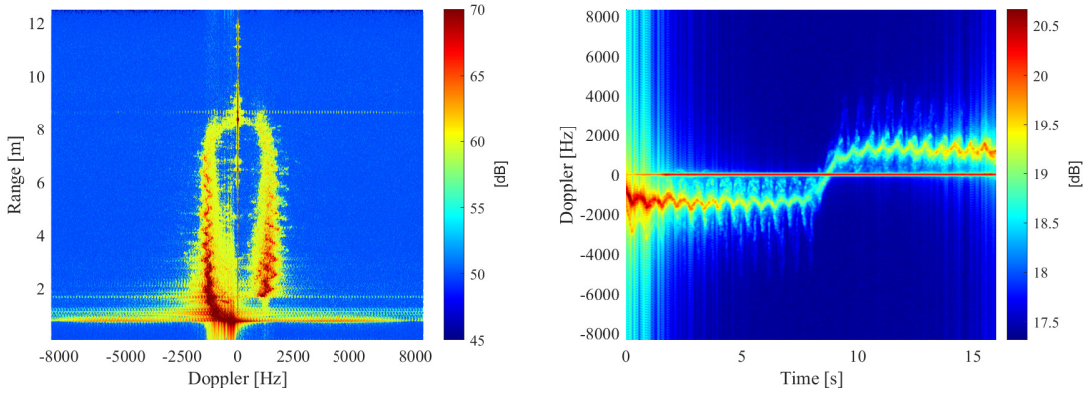

(a) (b)

Figure 2.5: Example of (**a**) range-Doppler map and (**b**) Doppler-time map for a walking person.

2.2 Classification Pipelines

In this section we describe the first developed pipeline, which is based on dimensionality reduction techniques and the classification algorithms used to discriminate different acquisitions under consideration. As regards features extraction, we resort to two different methods to reduce data dimensionality, the Principal Component Analysis (PCA) and the t-distributed Stochastic Neighbor Embedding (t-SNE).
Both maps obtained through the radar signal processing, will be considered as amplitude images. From the application of dimensionality reduction techniques to these images we obtain a vector, that is, the principal components extracted from PCA and the main dimensions given by the t-SNE, which will serve as features vectors. If for instance, we have a set of N images I_n of dimension $[l \times m]$, with $n = 1, \cdots, N$, images are initially vectorized row-wise and grouped in order to form a training set $\mathbf{X} = [x^{(1)}, \cdots, x^{(N)}]^T$, where T denotes the transpose operator; rows of $\mathbf{X}$ correspond to observations and columns correspond to variables. The j-th element of each row is then normalized according the following equation:

$$\bar{x}_j = x_j - \mu_j = x_j - \frac{1}{N}\sum_{n=1}^{N} x_j^{(n)}. \tag{2.3}$$

2.2.1 Principal Component Analysis (PCA)

Principal Component Analysis (PCA) [49, 50] is a non supervised transform also known as Karhunen-Loeve transform (KLT). It aims at finding suitable linear transformations y of the observed variables that are easily interpreted and capable of highlighting and summarizing the information inherent in the initial matrix I. PCA exploits a singular value decomposition (SVD) algorithm to extract the principal components of I. For further details please refer to [51]. This tool is especially useful when dealing with a considerable number of variables from which you want

to extract the greatest possible information while working with a smaller set of variables.
PCA can hence be described as a transformation of a given set of N vectors into inputs (variables) of the same length K placed in a vector N-dimensional $\mathbf{X}$, which allows to transform this vector into a second vector y, given by

$$y = \mathbf{A} \cdot (x_j - \mu_j), \tag{2.4}$$

which is the linear combination of the starting variable. μ_j represents the vector of the mean values, and it is defined as $\frac{1}{N}\sum_{n=1}^{N} x_j^{(n)}$. The multivariate vector $y = [y^{(1)}, \cdots, y^{(N)}]$ is built in such a way that the first element of y includes the greatest possible variability (and therefore more information) of the original variables, that the second represents the greater variability of the x_i after the first component, and so up to $y^{(N)}$ which takes into account the smallest fraction of the original variance. Therefore the main components are those linear combinations of the random variables $x^{(N)}$ according to the unit norm which make the variance maximum and which are uncorrelated.
The matrix $\mathbf{A}$ is instead determined by the covariance matrix $\mathbf{C}_x$, which represents the variation of each variable with respect to the others: the rows of $\mathbf{A}$ are represented by the eigenvectors of $\mathbf{C}_x$ ordered according to the decreasing order of the corresponding eigenvalues. The covariance matrix can be computed as

$$\mathbf{C}_x = \frac{1}{N}\sum_{i=1}^{N}(x^{(i)})(x^{(i)})^T \tag{2.5}$$

or exploiting a singular value decomposition (SVD) algorithm. $\mathbf{C}_x$ has dimension $[N \times N]$; elements on the diagonal represent the variances of $\mathbf{X}$, while the others determine the covariance between the input variables x_i and x_j. Rows of $\mathbf{A}$ are orthonormal, thus implying implying that the PCA algorithm is invertible, so original data can be easily recovered. The resulting vector y form the feature vector which can be used for classification.

2.2.2 t-distributed Stochastic Neighbor Embedding

t-SNE [52] is a non linear and non supervised transform, specifically designed to reduce dimensionality to 2 or 3 dimensions in order to display multidimensional data.
The t-SNE algorithm consists of two main steps: first, it computes a probability distribution over pairs of high-dimensional objects in such a way that similar objects have a high probability of being picked while dissimilar points have an extremely small probability of being picked. Given our set of N vectorized images $x^{(1)}, \cdots, x^{(N)}$ with length $l \cdot m$, t-SNE first computes the conditional probability $p_{j|i}$, which represents the similarity of datapoint x_j to datapoint x_i. In other words, it evaluates the probability that x_i would pick x_j as its neighbor if neighbors were picked in proportion to their probability density under a Gaussian centered at x_i. In formulas,

$$p_{j|i} = \frac{\exp\left(-\|x_i - x_j\|^2/2\sigma_i^2\right)}{\sum_{k\neq i}\exp\left(-\|x_i - x_j\|^2/2\sigma_i^2\right)}. \tag{2.6}$$

t-SNE then defines a similar probability distribution over the points in the low-dimensional map, and it minimizes the Kullback-Leibler (KL) divergence between the two distributions with respect to the locations of the points in the map. The output of this computation will be a vector of elements that can be used as features for the classification algorithm.

2.2.3 Classification algorithms

As regards the classification task, we consider the use of k-Nearest Neighbor (NN) and Support Vector Machines (SVMs), they are both supervised and non parametric algorithms.
k-NN [53, 54], is an instance-based algorithm, meaning that it does not explicitly learn a model. Instead, it chooses to memorize the training instances which are subsequently used as "knowledge" for the forecasting phase. In concrete terms, this means that only when a query is made in the database (i.e., when asked to provide a label with an input), the algorithm will use the training instances to send a response. As a drawback, this algorithm presents both a storage cost during the training phase, since it is necessary to store a potentially huge dataset, and a computational cost during the prediction phase as the classification of a given observation requires the vision and/or analysis of the entire dataset. In the context of classification, the k-NN algorithm essentially boils down to determine a majority vote among the k closest neighbors to a given unknown instance. The proximity is defined by a distance metric, usually the Euclidean distance, between two data points.
SVM [55], algorithm classifies data by creating a linear of non-linear decision boundary to separate different classes. It projects the data through a non-linear function to a space with a higher dimension, lifting them from their original space to a feature space, which can be of unlimited dimension. To perform this operation, SVM makes use of kernels, among which one of the most used is the Gaussian kernel, also used in this work. A graphical representation of these two classification can be found in Fig. 2.6a and 2.6b.

2.3 Experimental tests

The previously described methods can be combined in four classification pipelines, this methodology is summarized inside Fig. 2.7.
To validate their performances we need to build a dataset of mD signals and for these tests, we choose to classify different types of activities of walking people. The dataset can be found in [56] and consists of six different types of activities, performed by 29 subjects who repeat each activity several times. The subjects walk without any constraint or do not follow any pattern, at each subject was simply asked to walk for example in a "slow" or in a "fast" way, without specifying the number of steps or the time required to complete the activity, in order to generate data as realistic as possible. In addition acquisitions belonging to subjects of different height and weight were collected to provide a set comprehensive of a large variety of characteristics. The acquisitions are conducted inside an hallway of our department

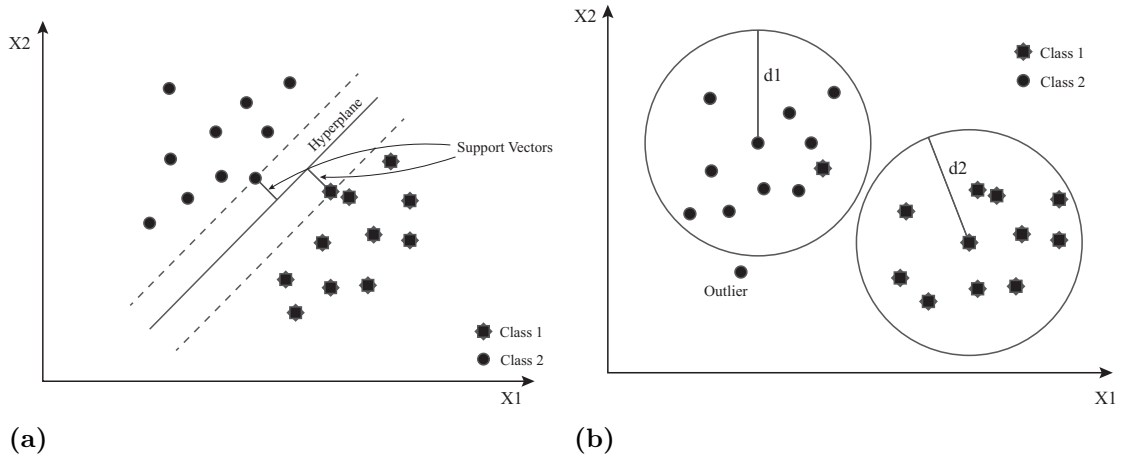

Figure 2.6: Two class classification example (a) SVM (b) kNN, in this case d_1 and d_2 are the distances metrics.

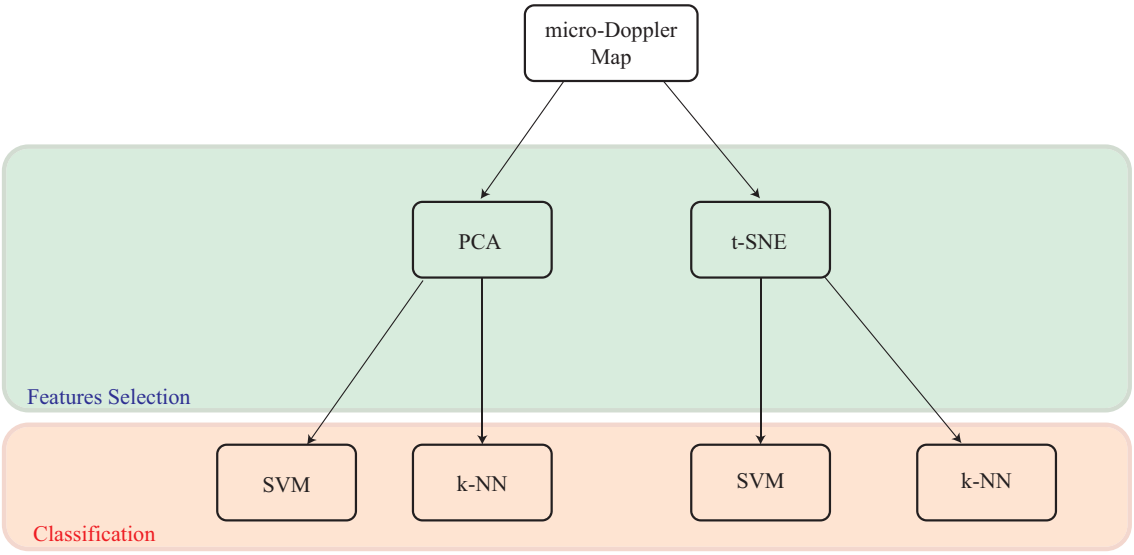

Figure 2.7: Pipelines used for the classification of the micro-Doppler maps.

and the subjects walks in front of the radar system who stands on a tripods. The test area is depicted in Fig. 2.8.
In each acquisition the subjects execute the activity going away from the radar and coming back, always in front of the radar system. The considered activity are:

- Walking slow;
- Walking slow with hands in pockets;
- Walking fast;
- Walking with hiding a metallic bottle;
- Limping;
- Walking slowly and swinging hands.

Figure 2.8: Hallway used for the acquisitions.

In the work described in [57], we choose to use only the first three activities: Walking Slow, Walking slow with hands in pockets and Walking fast. The reason is the mD generated by the activity inside the dataset. These three are more similar, so we expect a more difficult classification, so better performances can be obtained with the other cases.
This portion of the dataset is composed by nineteen subjects who repeated each activity for three times, for a total of 168 different acquisitions. Walking speed difference is subtle and depends on the person examined, who interpreted it subjectively. In general, the average speed measured for the fast walk is around 2 m/s, while for the slow walk, with both free hands or hands in pockets is about 1.2 m/s. The maps used for the classification process are calculated as previous described, for the Doppler-time map the STFT function uses windows of 512 samples, with an overlap of 98% where an Hann window is applied. The radar configuration used for these tests are reported inside Tab. 2.1.

Table 2.1: Radar parameters

Parameter	Value
f_{start}	77 GHz
Slope	60.012 MHz/ μs
t_{idle}	100 μs
ADC Valid Start Time	6 μs
f_s	10 Msps
t_{ramp}	60 μs
$n_{samples}$	512
n_{frame}	400
no. of chirps per frame	128
Periodicity	40 ms
Used Radar Bandwidth	3.6 GHz

A first analysis has been made on the background without any subject, which is depicted in Fig. 2.9a and 2.9b. Only one measurement has been performed, since the test area is the same for all the subjects. From this analysis is possible to see that the background does not affect the measurements, thus we can neglect its effect in the movements classification.

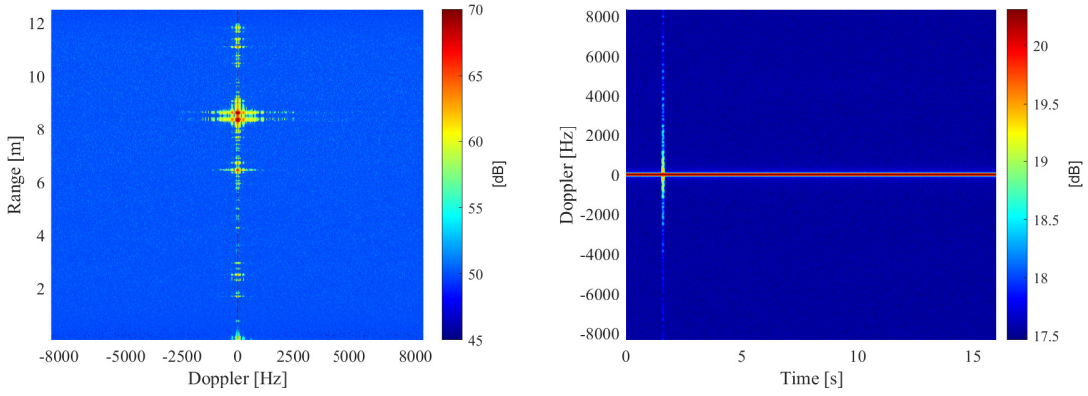

(a) **(b)**

Figure 2.9: Analysis on the background in absence of subjects using (a) Range-Doppler map and (b) Doppler-Time map.

In Fig. 2.10 we show an example of the same subject who walks in different ways, displaying both range-Doppler maps (on the left) and Doppler-time maps (on the right). It is possible to observe that slow and fast walk are easily recognizable in the maps. As expected, maps related to slow walk with hands in pockets present a slightly less evident Doppler with respect to free hands, but this effect is scarcely noticeable.
Data obtained after the processing of the radar signal are treated as images. Since their original size cannot be easily handled, all matrices have been reshaped to the

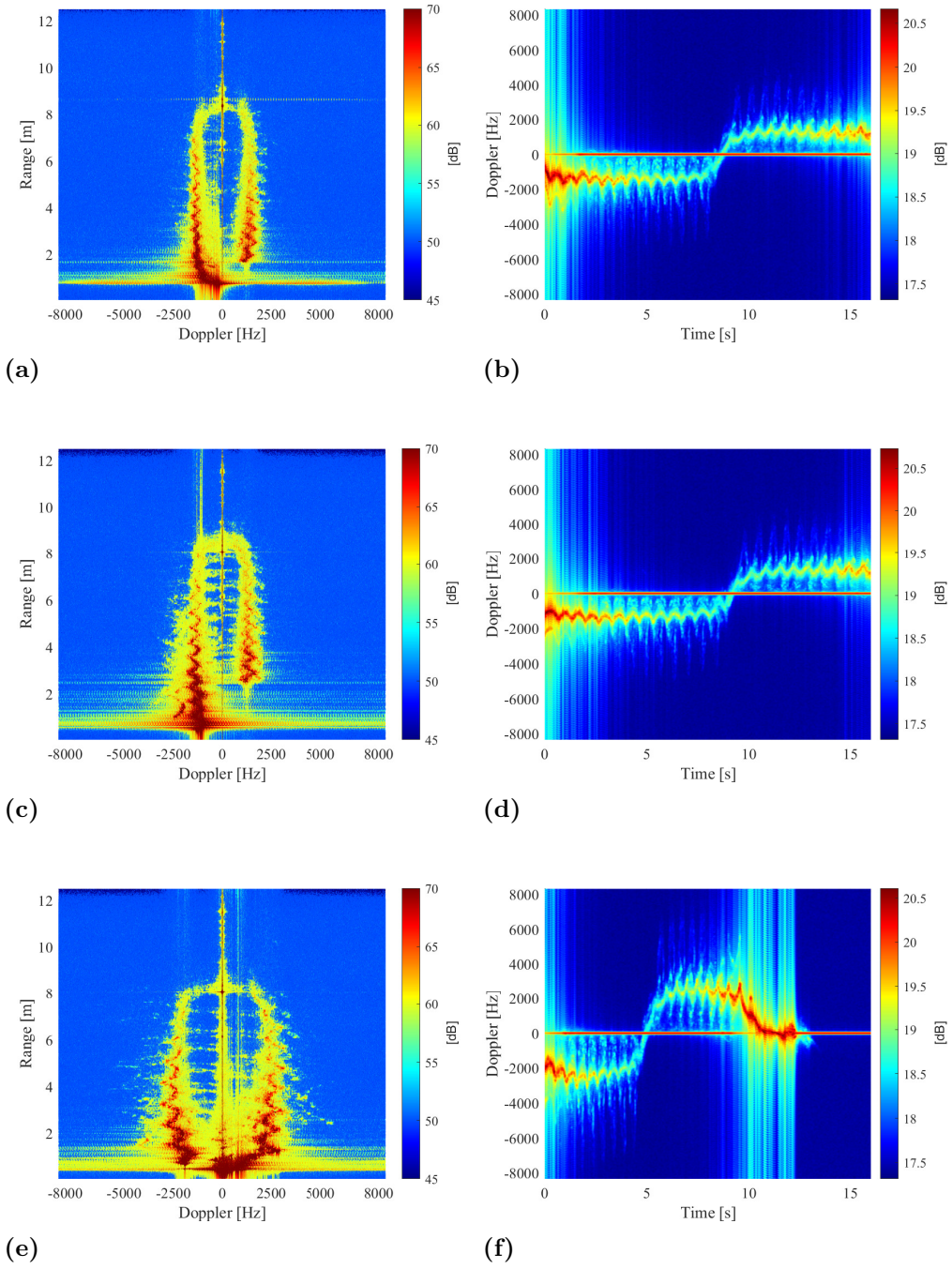

Figure 2.10: Example of a person walking slowly ((**a**) and (**b**)), slowly with hands in pockets ((**c**) and (**d**)) and fast ((**e**) and (**f**)).

same dimension [195 × 119], this result is obtained by applying a mean between near pixels of the image. In order to further reduce dimensionality and to extract features from images, PCA and t-SNE algorithm have been then applied separately to data. The matrices are vectorized so the new dataset is a matrix where each row is a range-Doppler map or a Doppler-time map. In Fig. 2.11a and 2.11b we show the classification accuracy resulting from exploiting a different number of principal

components, by using a NN classifier and a SVM algorithm. We choose to use a Gaussian kernel for the SVM. The figures' case is for the range-Doppler maps, the results with the Doppler-Time maps is very similar so we report only this one. The value of k for the k-NN and the kernel used for SVM have been chosen by using a leave-one-out cross-validation algorithm, which aims at minimizing the validation error. Each sample of the dataset is alternatively selected as a validation set, whilst the remaining part represents the training set. In this way all samples are used only one time both for training, both for validation. Results obtained by the algorithm for odd values of k between 1 and 49 are shown in Fig. 2.12, where k equal to 1 leads to an error of about 2.4%. The validation error obtained by different kernels in percentage is reported in Tab. 2.2, thus directing the choice to the use of linear kernel in our scenario.

Table 2.2: Results of the leave-one-out cross validation for support vector machine (SVM) with different kernels.

Kernel	Linear	Gaussian	Polynomial
Error validation (%)	4.46	17.26	33.33

We here define the metrics which will be used to evaluate the performance of the proposed methodologies. They are based on the so called *confusion matrix*, whose columns represent the predicted values for each class, while rows represent the actual values. The most common metric is the accuracy, which is defined as

$$Acc = \frac{TP + TN}{TP + TN + FP + FN}, \tag{2.7}$$

where TP and TN stand for true positives and true negatives, while FP and FN are the false positives and the false negatives. It represents the percentage of images assigned to the correct category.
Another useful metric is the precision (also called positive predictive value), which corresponds to the ratio of correctly predicted positive observations to the total predicted positive observations, or

$$P = TP/(TP + FP). \tag{2.8}$$

Recall (also known as sensitivity) is the ratio of correctly predicted positive observations to the all observations in actual class

$$R = TP/(TP + FN). \tag{2.9}$$

The F1 score is the harmonic mean of the precision and recall, where an F1 score reaches its best value at 1 (perfect precision and recall). Therefore, this score takes both false positives and false negatives into account as follows

$$F1 = 2RP/(R + P). \tag{2.10}$$

Sixty percent of the acquisitions are used for training, while the remainder is used for testing. Results have been averaged over 100 classification results obtained choosing

training and test sets at random. We consider here only two classes, corresponding to the slow and fast walk. Interestingly, it is possible to observe that the number of principal components (or number of dimension in case of t-SNE) that here corresponds to the number of features, has a small impact on the classification performance. The application of PCA or t-SNE algorithm to extract features from images leads to very similar results, although t-SNE was originally designed to reduce data to two or three dimensions, and becomes very slow for higher values. In addition, we obtain the same results using both range-Doppler and Doppler-time maps.

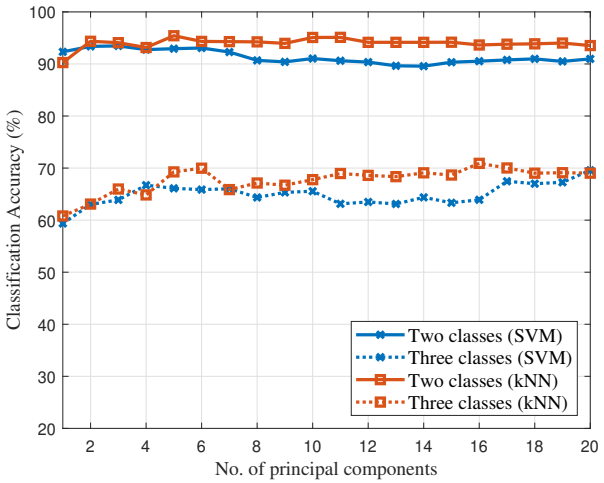

(a)

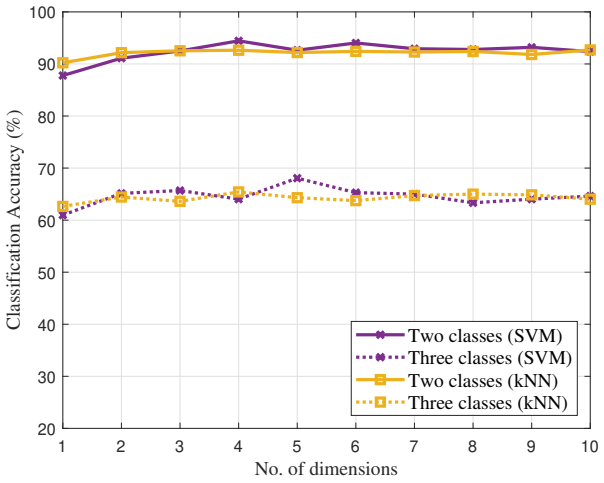

(b)

Figure 2.11: Comparison of classification accuracy achieved by SVM and kNN considering 2 and 3 classes, applying (**a**) Principal Component Analysis (PCA) and (**b**) t-distributed stochastic neighbor embedding (t-SNE). In the figures case, only range-Doppler map are considered.

In Tab. 2.3 and 2.4 we show the classification results, in terms of confusion matrices

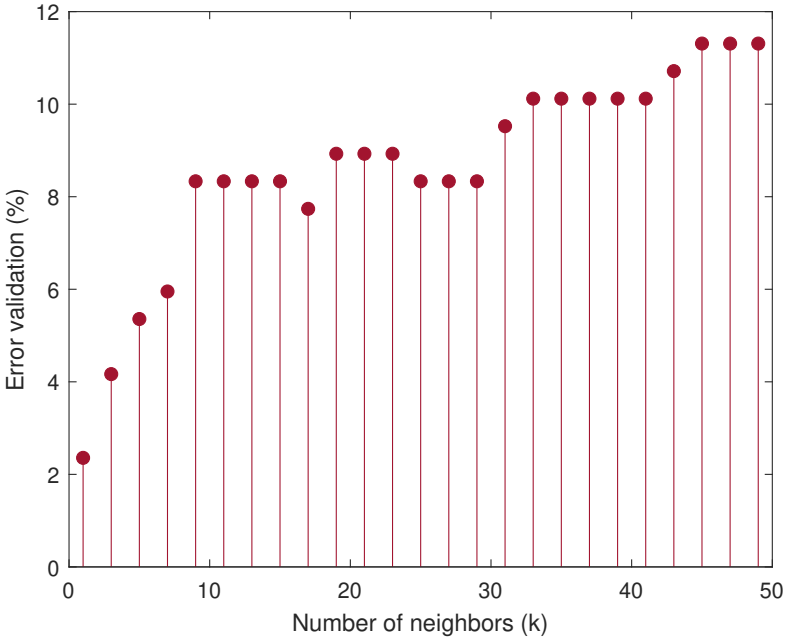

Figure 2.12: Results of the leave-one-out cross-validation for the k-Nearest Neighbor (kNN).

obtained by applying classification on two and three different classes. In the first table, measurements of slow walk and slow walk with hands in pockets have been incorporated into a single class, while in the second table they have been split into two separate classes. As predictable, distinguishing free hands from hands in pockets is a much more complicated task than identify different ways of walking. In the first case in fact the best accuracy obtained is about 72% and red boxes highlight the presence of a number of misclassified examples, although the fast walk is recognized from the other activities with a high precision (87.5%); SVM methods seem to achieve better performance than KNN algorithms. In the latter case we have instead an excellent accuracy of more than 93%. In both Tab. 2.3 and 2.4 we highlighted a high presence of correct detections in green, while a high number of misclassified samples is marked in red.

Table 2.3: Confusion matrix obtained applying SVM and kNN (into parentheses) on two classes, considering 5 principal components, $acc = 93.5\%$.

True / Predicted	S	F
Slow Walk (S)	110 (109)	2 (3)
Fast Walk (F)	9 (8)	47 (48)

In Tab. 2.5, we give an overview of the results obtained by other works focused on the classification of walking activities through radar measurements, showing the best accuracies achieved. [*] denotes the present work. In Reference [58] 7 types of activities are considered, that is, walking backwards, limping, depressed, elderly, excited, holding the arm and walking in a zigzag, and the radar used is an Ultra-

Table 2.4: Confusion matrix obtained applying SVM and kNN (into parentheses) on three different classes, considering 9 principal components, $acc_{\text{SVM}} = 72\%$, $acc_{\text{KNN}} = 66.7\%$.

True / Predicted	S	F	SH
Slow Walk (S)	33 (32)	2 (1)	21 (23)
Fast Walk (F)	4 (5)	49 (48)	3 (3)
Slow Walk with Hands in Pockets (SH)	16 (22)	1 (2)	39 (32)

Wide Band; Reference [59] considers a FMCW radar, and the examined activities are crawl, creep on hands and knees, walk, jog and run. Although the difference between walking slowly or quickly is less evident than the other activities, we prove that our system is able to achieve a better accuracy. Moreover, we consider a larger number of subjects that move differently from each other, thus confirming the validity of our method in a realistic context. The activity of holding the arm while walking [58], which is in some way comparable to our case of walking slowly with hands in pockets, could not be differentiated from the others at all, with a specific accuracy of 42.42%.

Table 2.5: Comparison of different radar based methods for human walking classification.

	Radar Type	No. of activities	Dataset dimension	Algorithm	Best accuracy
[*]	FMCW mmWave	2	19 subjects, 168 acquisitions	PCA/t-SNE + k-NN/SVM	93.5%
[*]	FMCW mmWave	3	19 subjects, 168 acquisitions	PCA/t-SNE + k-NN/SVM	72%
[58]	Ultra Wide Band	7	8 subjects, 280 acquisitions	PCA + SVM	89.1%
[59]	FMCW mmWave	5	3 subjects, 95 acquisitions	CV/TV + SVM	91%

The subjectivity and the personal speed interpretation of the conducted tests represents the major error source for our classification model. A standardized time or number of steps during the experiment should probably improve the system performance, but this would not represent a realistic scenario.

The same approach can be used on the other part of the dataset where the other activities are more different. This work can be found in [60] and inside the rest of this section will be reported and discussed. In this case only PCA and k-NN is considered as the others pipelines provides similar results. Four different activities, grouped in four classes, were examined:

- Slow walk with non-swinging hands [NS] (55 samples);
- Limping [L] (20 samples);
- Slow walk with swinging hands [S] (20 samples);
- Fast walk [F] (36 samples).

As regards the limping activity, subjects were to simulate a walk with a limp. This resulted in many different types of walking, since each subject has performed the request in its own way. No instructions were given about the other type of walk, in order to obtain data as realistic as possible.

In Fig. 2.13 Doppler-time maps for the four activities performed by the same subject are shown. From these maps it is possible to note the differences between the types of walk examined, which result very evident thanks to the high sensitivity of the used radar. The swinging hands (Fig.2.13b), for instance, results in a more evident effect on Doppler with respect to the non-swinging case (Fig. 2.13a), while limping (Fig. 2.13c) generates a very different map. In the following we consider the results obtained using the range-Doppler map.

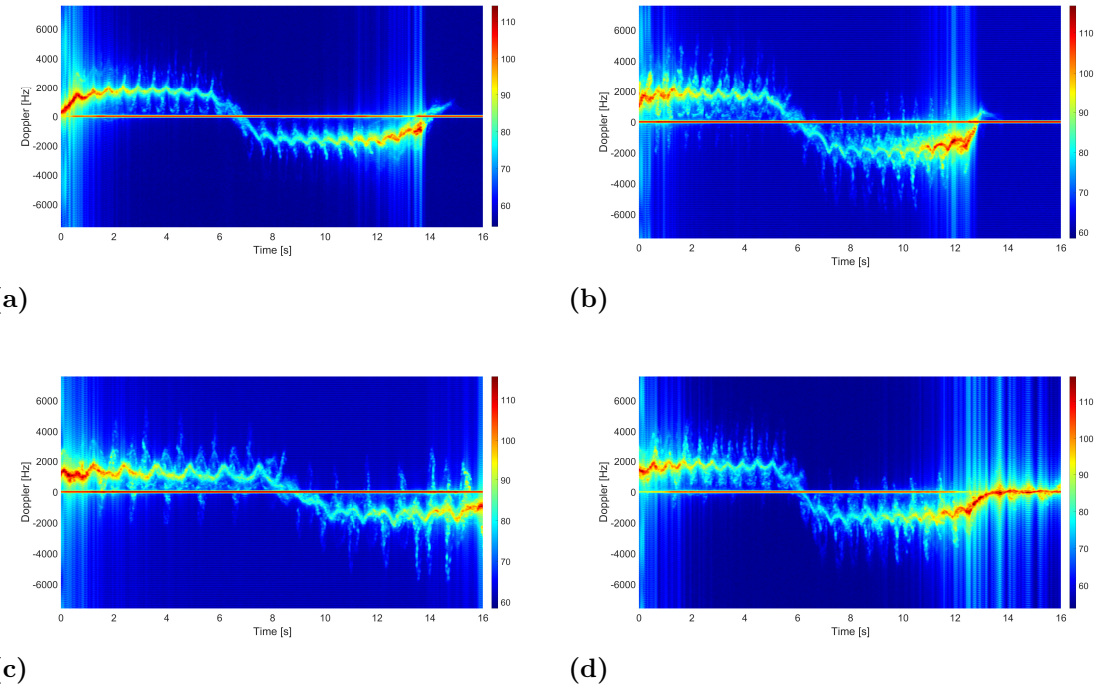

Figure 2.13: Doppler-time maps of a person walking slowly with non swinging hands (**a**), slowly with swinging hands (**b**), limping (**c**) and rapidly (**d**).

As we say for the previous test, data obtained from radar signal processing are treated as images and all matrices have been first reshaped to the same size [180×71], then their dimension has been further reduced by applying PCA. As we did before, the value of k has been chosen by using a leave-one-out cross-validation algorithm, by selecting alternatively a sample of the dataset as a validation set, while the remaining part is used as a training set. All samples are thus used only one time both for training, both for validation. Results obtained by the algorithm for odd values of k between 1 and 49 are shown in Fig. 2.14, where the value of k equal to 1 leads to the minimum error, corresponding to 1.33%.

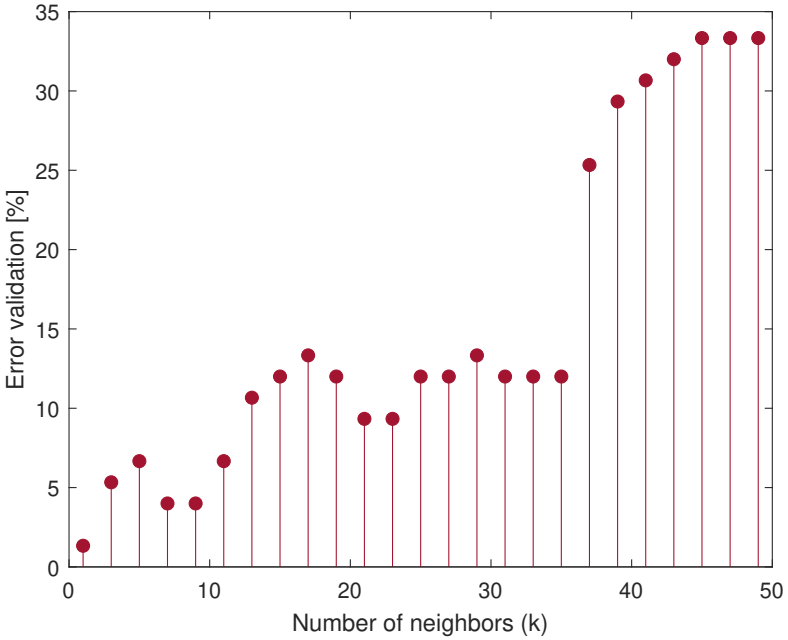

Figure 2.14: Results of the leave-one-out cross-validation for the k-NN for the second dataset.

In the classification process the 70% of the acquisitions are used for training, while the remainder is used for testing. In order to reduce the dependence of the results on the choice of the training set, results have been averaged over 50 classification results obtained choosing training and test sets at random.
In Tab. 2.6 we show the confusion matrix obtained by considering 9 principal components, which is the value that provides better performances and then applying k-NN. In this case, we choose to don't use the t-SNE feature extraction technique because provides similar performances compared to the PCA. We obtain an average accuracy of 96.1%, with excellent precision especially in detecting the slow walk with non-swinging hands and the fast walk.

Table 2.6: Confusion matrix obtained applying k-NN on four activities, considering 9 principal components. Accuracy 96.1%.

True / Predicted	NS	L	S	F
NS	98.91%	0	0	1.09%
L	3.67%	91.33%	0	5%
S	0	4.33%	95.67%	0
F	1.5%	0	0	98.5%

What we obtain with this second part of the dataset is similar to the first one. Is possible to distinguish two different activities of a person with good performances but these decrease when we try to distinguish similar activities such as walking slowly and slowly with hands in pockets.

The experimental evaluation confirms the power of the developed pipelines, but also the main drawback. Feature extraction technique must be applied to all the dataset to increase the data correlation with an overhead in the data processing.
For this reason, in the next section, we explore different ways to extract features on the maps, and this involves an ad-hoc construction of them and also a Deep Learning approach.

2.4 Comparison of different classification techniques

In this section we will discuss different ways to classify mD signals, this work is based on the previous described dataset and will use only three activities: fast walking, slow walking and slow walking with hands in pockets. The different pipelines are depicted inside Fig. 2.15.

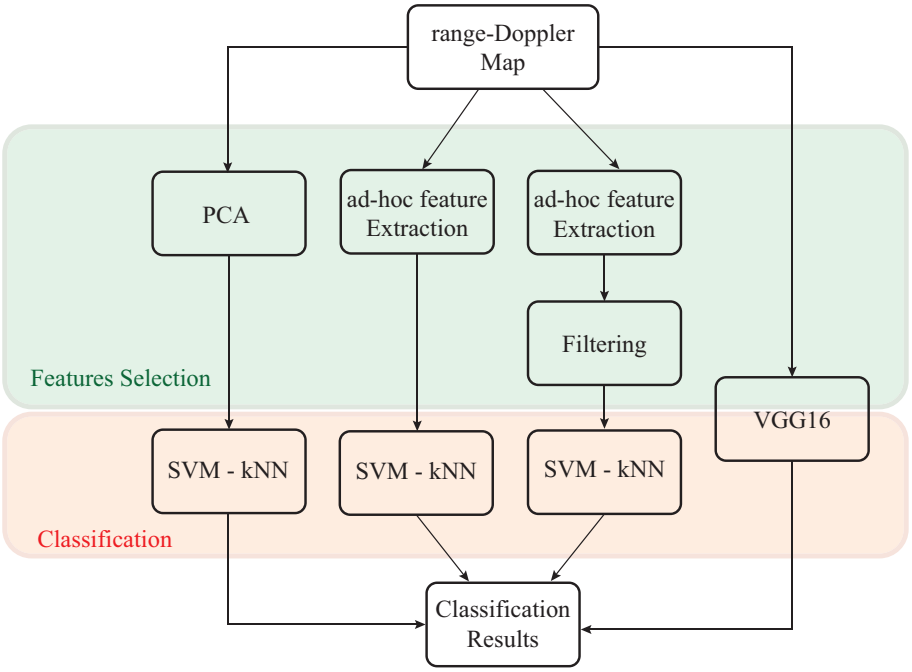

Figure 2.15: Flow chart of the different pipelines compared.

The purpose of this work is to understand if is possible to achieve similar classification performances with lower computation complexity techniques. For this reason, we compare three different types of approaches:

- PCA + k-NN or SVM;
- ad-hoc feature extraction + k-NN or SVM;
- Deep Learning (VGG16).

All the comparisons will be based on range-Doppler maps as we show how this and Doppler-time maps provide similar results. To increase the dimension of the dataset the range-Doppler map is divided into two halves, so from each acquisition, we obtain two maps of dimension $[256 \times 25600]$ (we call this matrix "map" for the rest of the chapter).

2.4.1 PCA complexity analysis

The output of PCA is a matrix Y of principal components. The first elements of each vector y in the resulting matrix Y, contain the greatest possible variability of the original variables, thus allowing to select a small set of variables which bring the largest possible information. Matrix Y can be then used as input for the classification algorithm. As regards the PCA computational cost, a dataset composed by L samples (or images in our case) is considered. Each image has dimension $[M \times N]$ and is vectorized before entering the PCA. The dataset dimension is therefore $[L \times MN]$. The main computational cost of PCA is given by the calculation of the covariance matrix, which requires a time in the order of $\mathcal{O}(L^2 \cdot MN)$. Eigenvalues and eigenvectors are then computed from this covariance matrix, requiring a complexity is in the order of $\mathcal{O}(L^3)$. Thus the total complexity of PCA is in the order of $\mathcal{O}(L^2MN + L^3)$.

2.4.2 Parameters extraction from range-Doppler maps

The application of PCA typically requires a high computational cost. Moreover, to obtain the best possible correlation between samples, it needs to be applied to the entire dataset and if a new sample is considered, the algorithm needs to be rerun. For this purpose, an alternative technique for feature extraction from range-Doppler maps can be proposed. We can calculate on each map different parameters that can be used as features. The parameters calculated on the range-Doppler maps are:

1. **Maximum Doppler value:** the parameter max_D is calculated by taking the maximum intensity value for each row of the Range-Doppler map as follows

$$max_D^{(i)} = max\Big(R_D(i)\Big), \tag{2.11}$$

   where i represents the row index and $R_{Doppler}(i)$ is the selected row. The rows in fact contain the information about the velocity of the target, and the maximum identifies the Doppler value for each considered distance.
   An example of the calculation process is reported in Fig. 2.16. All the $max_D^{(i)}$ elements at the end can be grouped inside a vector called $\overline{max}_D$.

2. **Mean Doppler value:** with a process similar to that used to compute the maximum, the mean values of the Doppler are evaluated for each row of the Range-Doppler matrix. These values compose a vector named $\overline{\mu}_D$ where each element is calculated as

$$\mu_D^{(i)} = \frac{\sum_{m=1}^{M} m \cdot R_D(i,m)}{\sum_{m=1}^{M} R_D(i,m)}, \tag{2.12}$$

   where i represents the row index considered for the computation, and m is the column index of the singe element. An example of $\overline{\mu_D}$ for different type of acquisition can be found in Fig. 2.17.

3. **Variance of the Doppler values:** the process used to evaluate this parameter slightly differs from the previous ones, because of the distribution of the Doppler values within the map. Fig. 2.18 depicts an example of the normalized

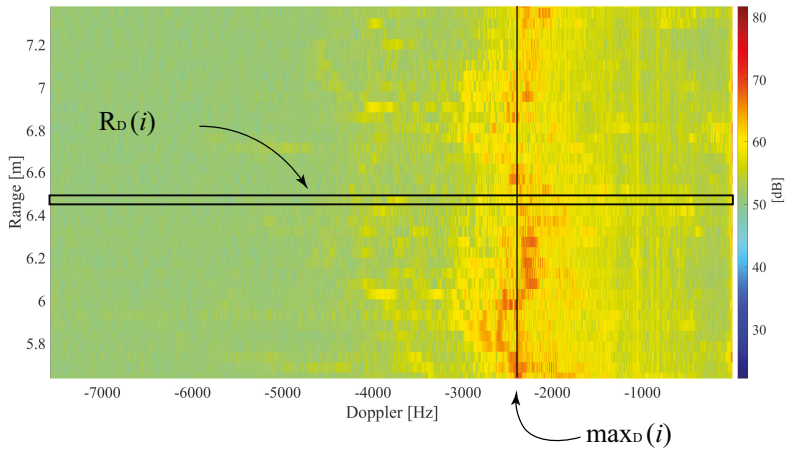

Figure 2.16: Extraction process of the Maximum Doppler value $max_D^{(i)}$.

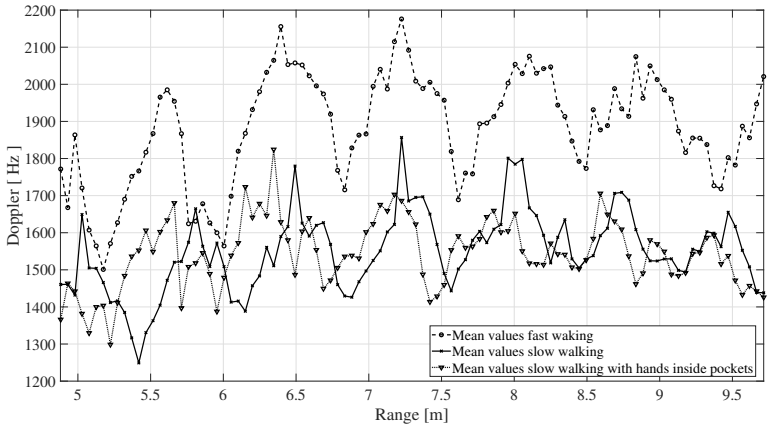

Figure 2.17: Comparison between the calculated values of $\overline{\mu_D}$ for different acquisitions.

distribution of the values at the same range distance. It is possible to see how the highest Doppler intensity values inside the map are concentrated around the zero-Doppler, both for the positive and the negative part. This effect is a result of the sensor parameters calibration, which allows to detect a more higher velocity than the target effective value.

This effect produces unbalanced results not centered on the mean values on the computation of the $\sigma_D^{2(i)}$, and for this reason, the following process is applied on the distribution of the values:

- the maximum amplitude value is extracted for each row of R_D, for the firsts 10000 Doppler bins in the case of the negative Doppler values, and the last 10000 for the positive;
- all the amplitude values under the calculated threshold are neglected by setting the values to zero.

The result of the previous described process is represented in Fig. 2.19. Only

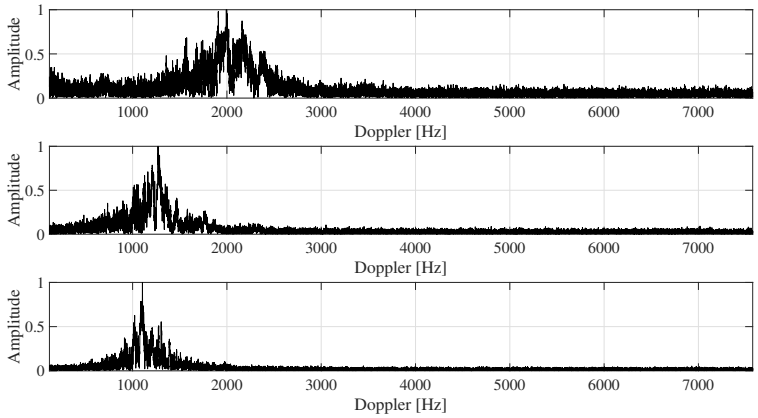

Figure 2.18: Doppler distribution for three different activities at the same distance. The values are re-scaled for a better comparison.

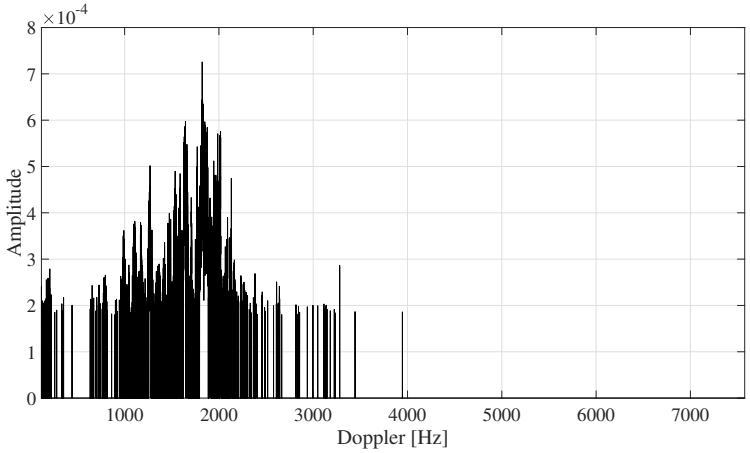

Figure 2.19: Effect of the applied threshold.

at this point we can compute the variance σ_D^2 as follows

$$\sigma_D^{2(i)} = \frac{\sum_{m=1}^{M} m^2 \cdot R_D(i,m)}{\sum_{m=1}^{M} R_D(i,m)} - (\mu_D^{(i)})^2. \tag{2.13}$$

The obtained vectors can be treated as signals and each sample is calculated on a slow-time row inside the Range-Doppler map. As a result the sampling frequency is related to the chirp time. A Butterworth filter is finally applied on these vectors in order to smooth the abrupt changes of the signal. An example is reported in Fig. 2.20 for the computation of the Maximum Doppler value before and after filtering, for the fast walk and slow walk activities contained in the dataset.
By looking at (2.11), (2.12) and (2.13), the cost for the extraction of each parameter can be easily computed respectively as:

1. Maximum Doppler value: $\mathcal{O}(L \cdot N)$;
2. Mean Doppler value: $\mathcal{O}(L \cdot N \cdot 2M)$;
3. Variance of Doppler values: $\mathcal{O}(L \cdot N \cdot 2M)$.

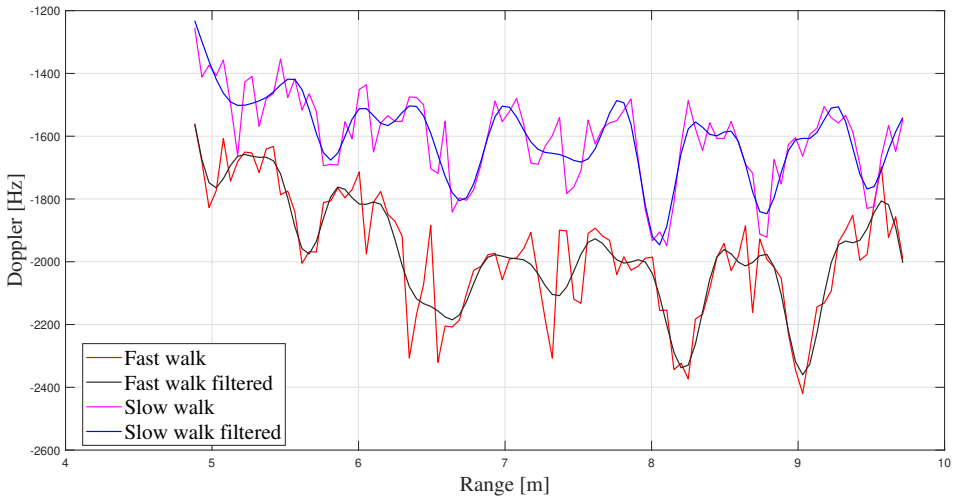

Figure 2.20: Effect of the Butterworth filter on the computation of the Maximum Doppler value for the fast walk and the slow walk activities.

By comparing the sum of these costs with the PCA complexity, it can be easily stated that this second methodology is computationally cheaper.

2.4.3 VGG16 neural network classification

In this case, we will consider the use of the VGG16 network [61, 62] to generate a model that classifies activities according to the classes contained in the dataset.
Working with a dataset with a small dimension it is possible to avoid the training of the model from scratch by using transfer learning [63]. Neural networks require a huge dataset to perform the training, is possible to use a smaller dataset by using transfer learning [63]. Transfer learning is particularly useful to avoid expensive training of new neural networks when working with a small amount of data and allows to extract the network weights from pre-trained models and to transfer them to other networks. Range-Doppler maps are taken as input for training and the model trained on the ImageNet Large Visual Recognition Challenge dataset [64] is then retrained using the selected dataset by following the procedure described in [63].
For a single image, the computational cost required by a convolutional network is $\mathcal{O}(F_I M N m n F_O)$, where each input feature map is of size $(M \cdot N)$, spatial two-dimensional kernels are of size $(m \cdot n)$ and F_I, F_O are the input and output channels within a layer, respectively [65].

2.4.4 Machine learning classification

After feature selection, the classification is performed using the k-NN and the SVM, which present different computational costs. As described before, parameters optimization for both algorithms has been carried out by using a leave-one-out cross-validation algorithm, whose goal is to minimizing the validation error. On the basis

of this evaluation, k is chosen equal to 1 and a linear SVM is selected. The complexity analysis follows:

k-NN complexity: Generally, a k-NN requires a computational cost in the order of $\mathcal{O}(Ly + kL)$, by assuming that k has been previously fixed. L represents the cardinality of the training set and y is the dimension of each sample. y may be the output of the PCA or the vector collecting the extracted parameters.

The total cost of NN algorithms can be easily derived considering the following steps:

- Distance computation: the distance of a new observation from each sample of the training set is computed. For each computation the cost requires is in the order of $\mathcal{O}(y)$.
- Label assignment: the k samples with the small distance value are selected by looping the entire training set. The label assigned to the new observation is that owned by the majority of the k selected samples. Each iteration of the second step requires a cost in the order of $\mathcal{O}(L)$ by looping through the training set observations, so the overall step cost will be in the order of $\mathcal{O}(kL)$.

SVM computational complexity: Linear SVM has a complexity equal to $O(L)$, being it is just a single inner product. Kernel SVMs usually require a higher cost, depending on the choice of the kernel and on the number of supporting vectors s_v. For most kernels, including polynomial and Gaussian, the cost is $O(s_v L)$. An approximation exists for SVMs with a Gaussian kernel that reduces the complexity to $\mathcal{O}(L^2)$.

Linear SVM therefore requires a lower cost then k-NN, while kernel SVM may need a higher complexity. The classification cost must then be added to that required by the feature selection method considered.

2.4.5 Deep learning results

The dataset is split into 80% for training, 10% for validation, and 10% for test purposes. Based on 100 training steps, or *epochs*, in Figures 2.21a and 2.21b we show the training and validation loss for the three separate classes and when a slow walk and slow walk with hands in pockets are merged, respectively. The training loss indicates how well the model is fitting the training data, while the validation loss indicates how well the model fits new data. They are evaluated using cross-validation. Values smaller than 0.75 are observed after 80 epochs in Fig. 2.21 and tests with more than 100 epochs tend to overfit. When only two activities are considered, the performance improves and the validation loss assumes on average values between 0.2 and 0.3 with a small number of epochs.

In Table 2.7 we show some other classification metrics for our model for each considered class, i.e., precision, recall, and F1-score. It is possible to note that both slow and fast walk classes achieve an excellent precision but a low recall, while the opposite behavior is observed for the slow pocket class.

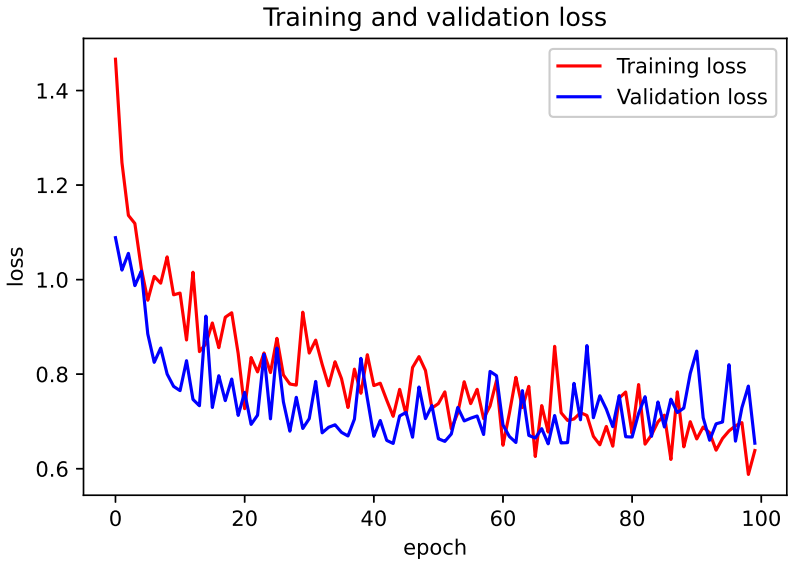

(a)

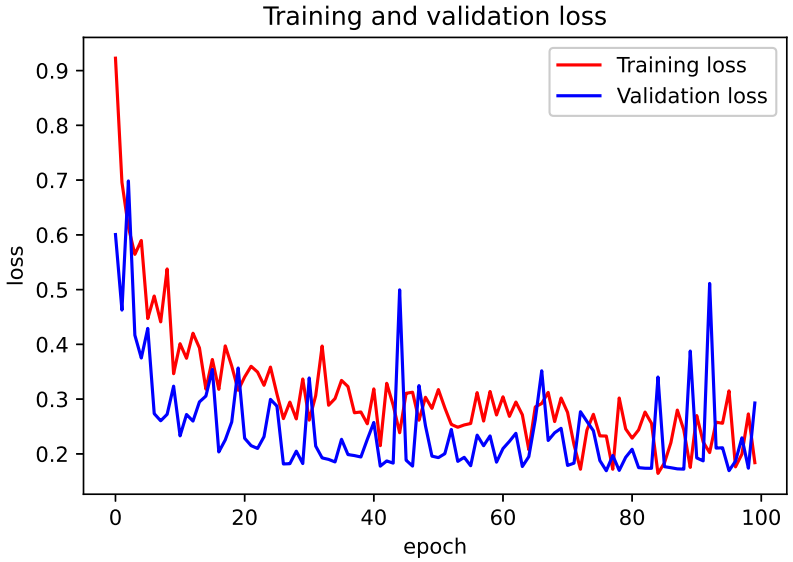

(b)

Figure 2.21: Training and validation loss of VGG16 neural network for a) three and b) two classes.

2.4.6 Comparison between different methodologies

As explained before, we extract from the range-Doppler maps three vectors of parameters, representing the maximum, the mean, and the variance of the Doppler values. After obtaining these vectors for all acquisitions in the dataset, they are averaged to obtain three features, or six if we consider both the positive and the negative parts of the range-Doppler maps. As the subjects do the same activity going away from the radar and coming back we can split the acquisition into two

Table 2.7: VGG16 results for the three activities.

	Precision	Recall	F1-score
Fast	1	0.57	0.73
Slow	1	0.43	0.60
SlowPocket	0.6	0.86	0.71

halves and increase the number of features. The resulting matrix has 171 rows and 3 (or 6) columns. This reduced matrix helps us to use fewer resources when doing the classification task. In the classification based on these features, 60% of the acquisitions are used for training, while the remainder is used for testing. Results have been averaged over 50 classification results obtained choosing training and test sets at random. Classification accuracy obtained by the different methodologies illustrated in the previous sections are reported in Tables 2.8 and 2.9, while a summary of the computational costs for each of the proposed techniques is reported in Table 2.10. It is important to note that the VGG16 cost refers to a single image, and not to the entire training set.

Table 2.8: Accuracy achieved by the proposed methods for two activities.

Method	Classification Algorithm	Accuracy
PCA	SVM	93.50%
PCA	kNN	93.50%
ad-hoc Features Extraction	SVM	84.20%
ad-hoc Features Extraction	kNN	86.18%
ad-hoc Features Extraction + filtering	SVM	94.20%
ad-hoc Features Extraction + filtering	kNN	94.20%
Deep Learning	VGG16	93.75%

Table 2.9: Accuracy achieved by the proposed methods for three activities.

Method	Classification Algorithm	Accuracy
PCA	SVM	72%
PCA	kNN	66.70%
ad-hoc Features Extraction	SVM	63.70%
ad-hoc Features Extraction	kNN	66.10%
ad-hoc Features Extraction + filtering	SVM	73.70%
ad-hoc Features Extraction + filtering	kNN	73.70%
Deep Learning	VGG16	66.67%

Table 2.10: Computational costs of the considered methodologies for feature selection. *Note that the cost for the VGG16 refers to a single image.

Method	Computational cost
PCA	$\mathcal{O}(L^2MN + L^3)$
ad-hoc Features Extraction	$\mathcal{O}(LN(1 + 4M))$
VGG16	$\mathcal{O}(F_I MNmnF_O)^*$

By looking at the table it is evident how the parameters extraction together with filtering leads to better results than other methodologies, and also requires the lowest computational cost. Interestingly, the application of the filtering has an important impact on the results, helping to enhance the performances. Deep learning improves the accuracy given by the PCA + classification method for both the cases of two or three activities, but it is outperformed by the parameter extraction with filtering. This is ascribable to the small dimension of the dataset under consideration, since the VGG16 network is more performing in presence of a large training set.

2.5 Ad-hoc features extraction: UAVs

What we discussed before, can be applied also in another application field: the Unmanned Aerial Vehicles (UAV) identification. UAV are nowadays becoming very common and are available for different applications and purposes [66]. For this reason, each country has adopted a regulation in terms of allowed flight zones and types of drones that can be sold [67]. In fact, these devices are not always used for fun or to support a professional activity, but sometimes they are employed to cause disorders or dangerous situations [68]. For this reason, it is important not only to detect the drone but also to predict any dangerous way of flying.
Different approaches for the detection of drones are proposed during time, one of them is to assign each authorized drone a unique code for its identification called Automatic Identification System (AIS), as used for air and sea traffic control. If the drone is not authorized by the local authority, it can be pulled down to avoid any danger. Another common technique is to use radars, through which the UAV can be detected but also some information on the type of drone detected can be obtained. Radar systems provide in fact not only drone's velocity or distance information, but also the dimension of the drone can be estimated by measuring its RCS. The mD can be also used in this application. The propellers and all the moving parts provide a mD signature that can be useful to classify different types of UAVs with ML approach. This technique requires firstly to define and compute the features to be used and identify its flight characteristics. These can be provided in near real-time in order to predict and anticipate dangerous situations. Conversely, if it takes a long time to classify the drone, the system can become ineffective.
A common technique is to analyze the STFT spectrograms, from which the mD signature of a drone becomes well evident. This approach is well-known for the case of different kinds of target movement recognition, and a lot of research on this topics has been carried out during the years [69, 70, 71]. However, a problem related to the analysis of spectrograms is the time needed for the computation. It is

not only the complexity of the algorithm which adds a delay on the detection, but also the time duration of the observation. The STFT needs usually several seconds to be calculated, the reason is the observation time of the target. For a propeller that rotates at 1000 rpm, a rotation can be captured with some milliseconds of acquisition, but to detect and interpret a movement, many seconds of acquisition are needed. Also, the STFT is a more complex elaboration than the FFT and this is an additive contribution to the delay who can affect the identification process. To simplify this process it is then possible to define many parameters of the computed spectrograms, through a less computationally expensive approach, in order to enable a faster identification.
Providing some information on how the drone is flying and the characteristics of its range-Doppler map can be useful to reduce the time needed to predict potentially dangerous situations. The extraction of features from the range-Doppler maps is faster and easier than an STFT computation, so the classification can be achieved more quickly. This work aims to provide a quick feature extraction procedure on the range-Doppler and can be found in [72]. To validate the method we conduct experimental tests on two different types of drones (both with four propellers): the smallest is a commercial one, and the other is assembled in our lab. Both models are depicted inside Fig. 2.22. The motivation for using two different UAVs is to analyze the mD features in real situations: the commercial drone is a commonly sold item, and this way, the developed technique is validated also with a commercially available UAV.

2.5.1 Features extraction

The extraction of the features is performed directly on the range-Doppler map where the position of the target depends on the distance and the relative speed to the radar system. Each element of the range-Doppler matrix gives information and the drone is not present in just one "pixel" element. The number of bins occupied along the axis and the related amplitude values provide the information that can be used for classification purposes.
In Fig. 2.23 an example of the range-Doppler map is provided, where the main target, that represents the drone, is also the only one that does not stand on the zero-Doppler line (Doppler bin no. 65). To improve the identification performances, an interpolation factor of 2 along the range is applied during the FFT computation. For each map it is possible to evaluate different parameters along with the Doppler and along with the range, and they are:

- the weighted mean values $\mu_{Doppler}$ and μ_{range};
- the standard deviation values $\sigma_{Doppler}$ and σ_{range}.

These parameters are simple to calculate, so if we use them as features for the classification the performances, in terms of latency, can be improved. To calculate the weighted means and the standard deviation of Doppler and range, the position of the drone inside the map must be located. In a real outdoor conditions this can be done with a classical approach based for example on CFAR thresholds. In this case, we choose a simpler approach as only one drone is present inside the measurement area

(a)

(b)

Figure 2.22: Drones used for the measurements a) Custom drone b) Potensic T25.

and this area is also small. The center position is calculated as the maximum value inside the zone of interest of the range-Doppler map. The coordinates of the point are then used to extract the corresponding Doppler and range vectors. The values used for the computation of the features are the magnitude of the elements inside the vectors, and, for each range-Doppler map, four parameters will be extracted. The procedure applied in the experiments is represented in Fig. 2.24.
The following notation will be used to describe the computation of the features:

- $\bar{R}(\bar{r}, d)$: vector of magnitudes along the range used to calculate μ_{range} and σ_{range};
- $\bar{D}(r, \bar{d})$: vector of magnitudes along the Doppler used to calculate $\mu_{Doppler}$ and $\sigma_{Doppler}$;
- $\bar{r}$: vector of indexes of the bins along the range axis;
- $\bar{d}$: vector of indexes of the bins along the Doppler axis;
- r,d : coordinates of the target (drone) position.

The values of r are limited to the number of bins and can go from 1 to r_{max}, where r_{max} depends on the numbers of samples used in each chirp; at the same time, d

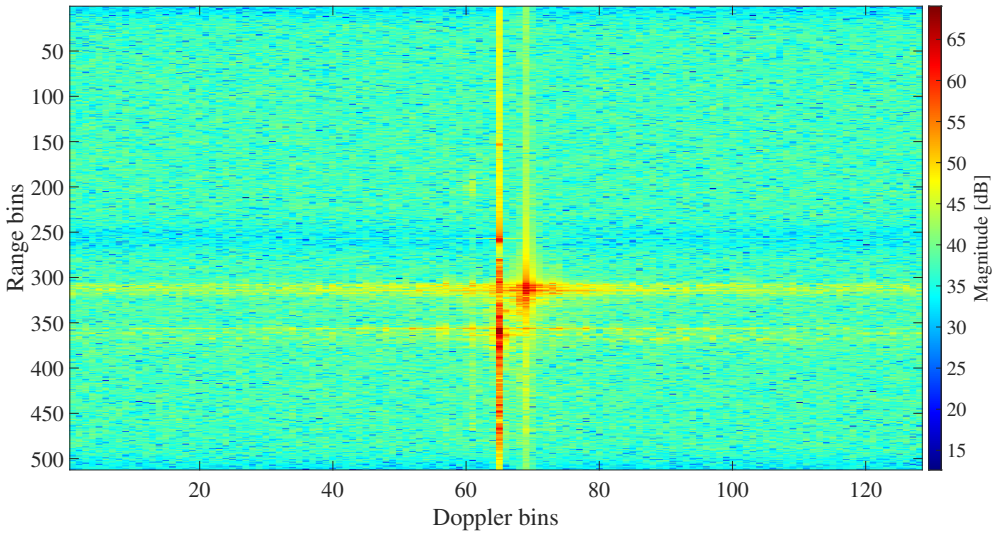

Figure 2.23: Example of a range-Doppler map of a drone flying in the front of the radar system.

goes from 1 to d_{max}, where d_{max} depends on the number of transmitted chirps inside a frame. The range-Doppler map evidences all the detected targets, for this reason only a portion of the total map is considered and the zero-Doppler line is neglected. To such an aim, the values outside the defined map area are imposed equal to zero. The dimension of the considered range bins must be chosen in accordance with the dimension of the UAV under analysis. In Fig. 2.25 the effective map used is shown. The following equations are used to calculate the features chosen as parameters:

$$\mu_{range,i} = \frac{\sum_{r=1}^{r_{max}} r \cdot \bar{R}(\bar{r}(r), d)}{\sum_{r=1}^{r_{max}} \bar{R}(\bar{r}(r), d)} \tag{2.14}$$

$$\mu_{doppler,i} = \frac{\sum_{d=1}^{d_{max}} d \cdot \bar{D}(r, \bar{d}(d))}{\sum_{d=1}^{d_{max}} \bar{D}(r, \bar{d}(d))} \tag{2.15}$$

$$\sigma_{range,i} = \sqrt{\frac{\sum_{r=1}^{r_{max}} r^2 \cdot \bar{R}(\bar{r}(r), d)}{\sum_{r=1}^{r_{max}} \bar{R}(\bar{r}(r), d)} - \mu_{range,i}^2} \tag{2.16}$$

$$\sigma_{Doppler,i} = \sqrt{\frac{\sum_{d=1}^{d_{max}} d^2 \cdot \bar{D}(r, \bar{d}(d))}{\sum_{d=1}^{d_{max}} \bar{D}(r, \bar{d}(d))} - \mu_{Doppler,i}^2} \tag{2.17}$$

where i is the index of each map inside the data cube.
The calculated parameters are used to trace, for each frame, a pseudo-ellipse in the (Doppler bins, Range bins) plane, obtained by using the mean values of Eq.s (2.14) and (2.15) as the center coordinates, and the standard deviations of Eq.s (2.16) and (2.17) as the axes amplitude. In Fig. 2.26 an example of this graph is represented. The parameters and the geometry of the pseudo-ellipse can be used to classify how the drone is moving. The dimension of the figure is dependent on how the drone

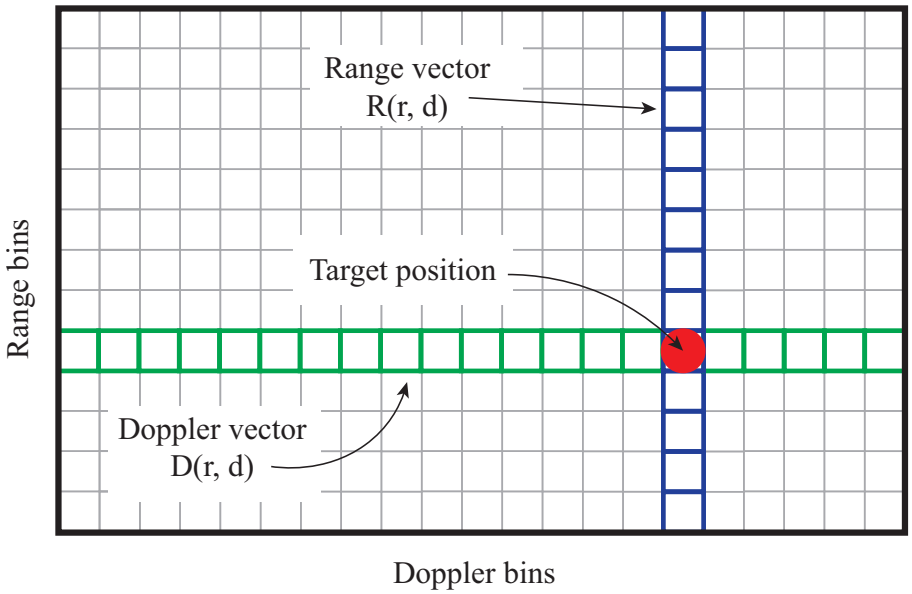

Figure 2.24: Range and Doppler vectors of magnitude extraction procedure.

is flying and on its physical characteristics. To calculate the shape of the pseudo-ellipse we divide the figure into four quadrants, from 0 to $\pi/2$, from $\frac{\pi}{2}$ to π, from π to $\frac{3\pi}{2}$ and from $\frac{3\pi}{2}$ to 2π. This process can be found inside Fig. 2.27.
For each quadrant, we calculate the position of the points $P(x, y)$ with the equations:

$$P_x = R_x \cdot cos(\theta) + c_x \tag{2.18}$$

$$P_y = R_y \cdot sin(\theta) + c_y \tag{2.19}$$

where R_x and R_y are the semiaxis in each quadrant, θ the angle and c_x and c_y the coordinates of the ellipse center. The values of R_x and R_y can be calculated as

$$R_x = \sigma_x - |c_x - \mu_x| \tag{2.20}$$

$$R_y = \sigma_y - |c_y - \mu_y| \tag{2.21}$$

where σ and μ are the standard deviation and the mean value along the relative axis.

2.5.2 Experimental Tests and results

To validate the proposed technique, two sets of measurements are conducted. In the former, the biggest drone is flying in the front of the radar; in the latter, the smallest drone is fixed to a table, so only the movement of the propellers and the tilted position can influence the value of the calculated parameters. The measurement setup is graphically represented in Fig. 2.28.
In the first case, the drone is free to fly in front of the radar at a variable distance. Since the space available is limited, also the movements of the drone are limited. In

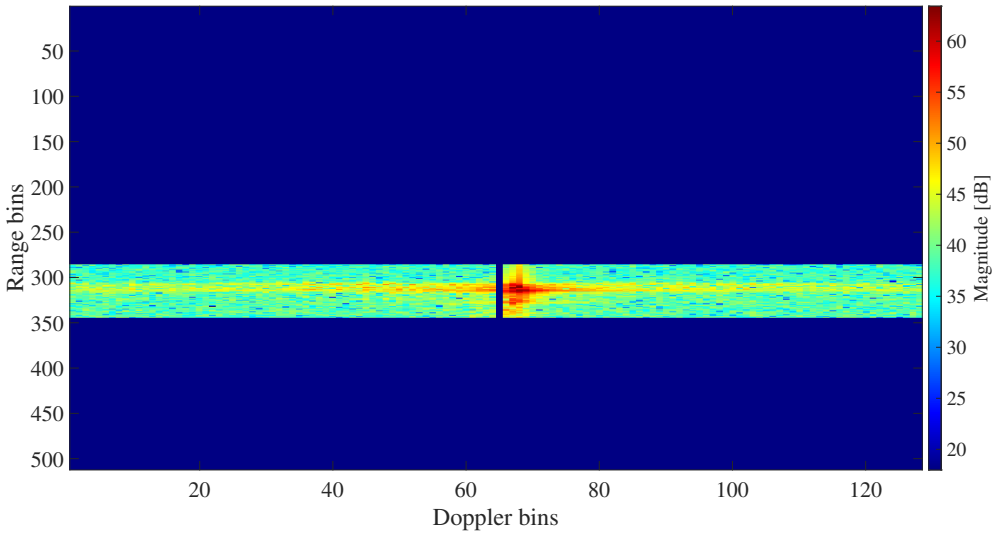

Figure 2.25: Effective range-Doppler map considered for the parameters computation.

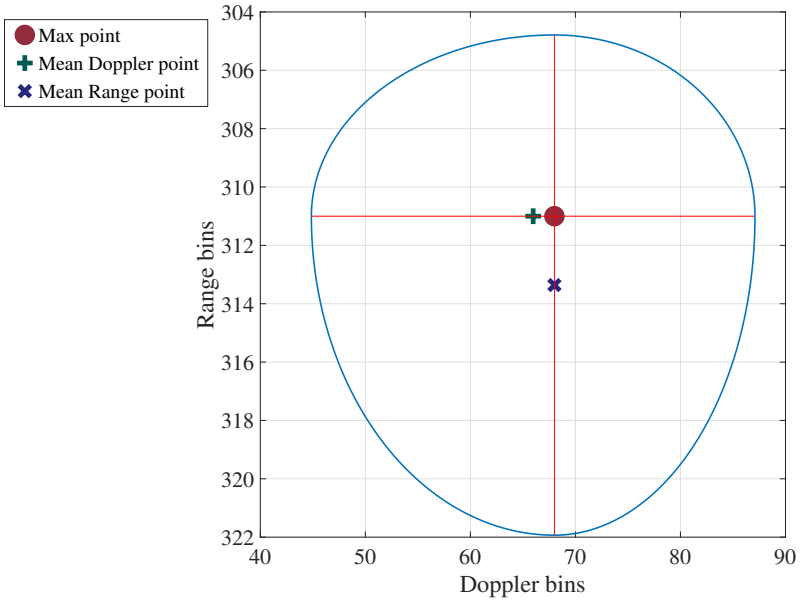

Figure 2.26: Example of pseudo-ellipse extracted.

this phase of the algorithm development, we are interested to study if the proposed method is true with an experimental evaluation. So, for this case, the drone flying without a particular motion style: sometimes is moving along the pitch axis or sometimes along the roll axis. Also, in some acquisition is hoovering. These activities for the moment are not useful to create a classification dataset but can be used to understand if the geometry of the pseudo-ellipse change. Small movements are difficult to detect and cannot be revealed with classical radar detection but maybe is possible by exploiting the mD effect.

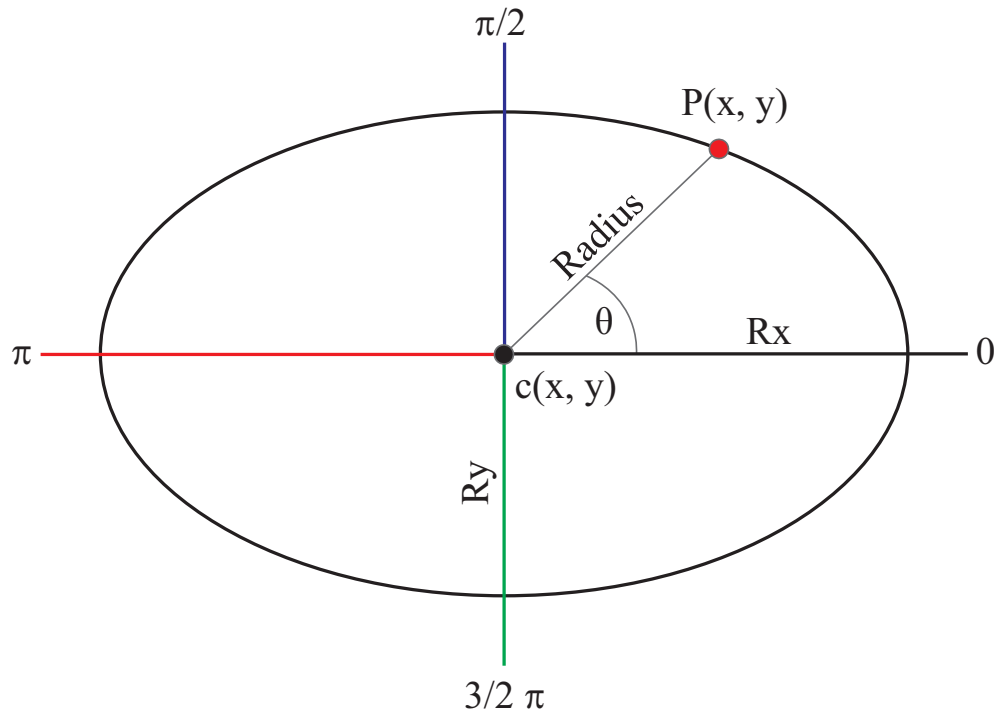

Figure 2.27: Pseudo ellipse construction schematization. Each semi-axis is identified with a different colour.

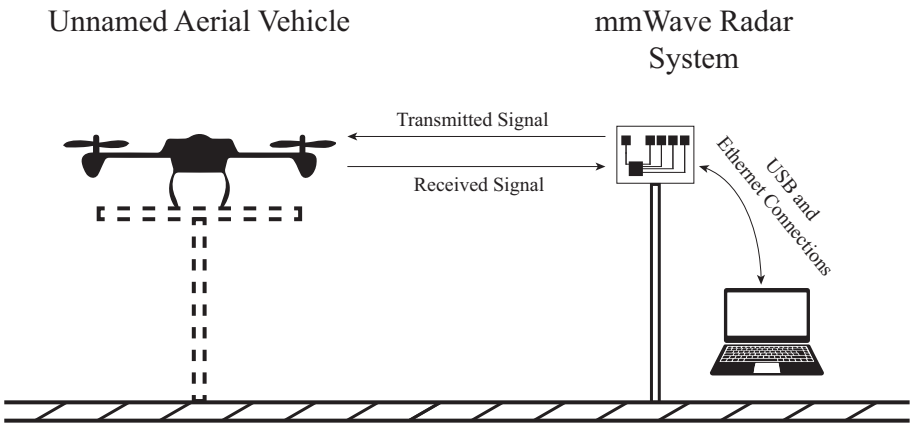

Figure 2.28: Representation of the measurement setup. In the former test, the drone is free to fly; in the latter, it is fixed to a table. In the figure, the table is represented with dotted line.

The second set of measurements is conducted with the purpose of removing the dependency from the drone movement. Only the variation of the micro-Doppler and the range profile must influence the calculated parameters values. For this reason, the drone is fixed to a table with a tape and is not able to fly. In this condition five acquisitions are made. In three of them, the drone changes the rotational speed of the propellers but stands on the horizontal plane. In the other two acquisitions, the drone is tilted along the pitch rotation axis, and along the roll rotation axis, respectively. The purpose of this test configuration is to force the drone to change

the rotational speed of the propellers in a tilted position. This way it is possible to understand how this flying modality influences the extracted features.
The radar configuration parameters used for all the measurements are kept the same and are reported in Table 2.11.

Table 2.11: Radar Parameters

Parameter	Value
Idle Time	100 μs
ADC Valid Start Time	6 μs
ADC Sampling Time	66 μs
Effective Radar Bandwidth	3.607 GHz
$f_{sampling}$	10 MHz
$t_{periodicity}$	40 ms
no. of Chirp in a Frame	128
no. of ADC Samples	512
Total chirps transmitted	400

With the chosen parameters, each acquisition has a duration of sixteen seconds. At the end a total of five acquisitions for the first set is carried on, and four acquisitions for the second one. As the second set of measurements is conducted to collect only the micro-Doppler effect of the propellers the number of acquisitions is different between the two sets.

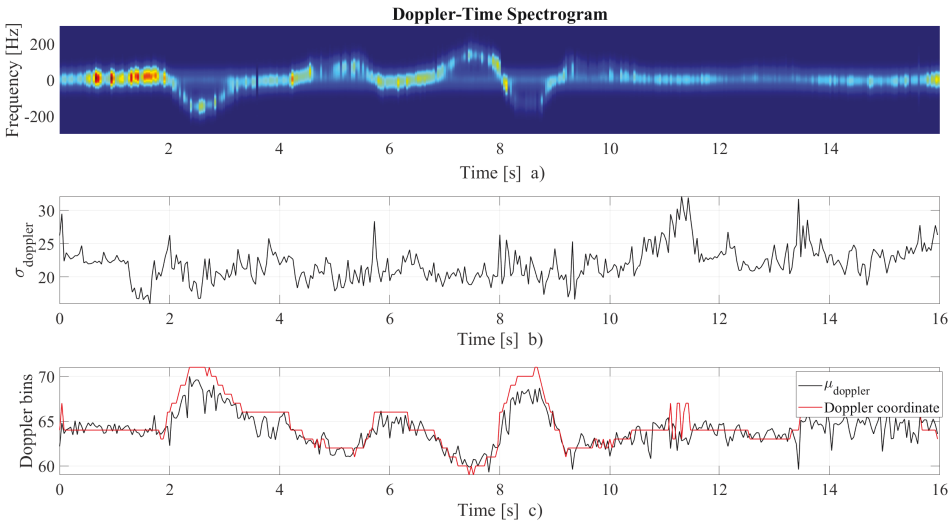

Figure 2.29: Comparison between the Doppler parameters and the Doppler-Time spectrogram: a) calculated Doppler-time spectrogram, b) $\sigma_{Doppler}$ and c) $\mu_{Doppler}$.

In each flying condition, which can be a hoovering or a rotation along an axis, the rotational speed of the propeller is always symmetrical. This condition derives from the conservation of the angular momentum [73]. The same happens for the micro-Doppler, for which the effect, for example in a hoovering condition, is equally

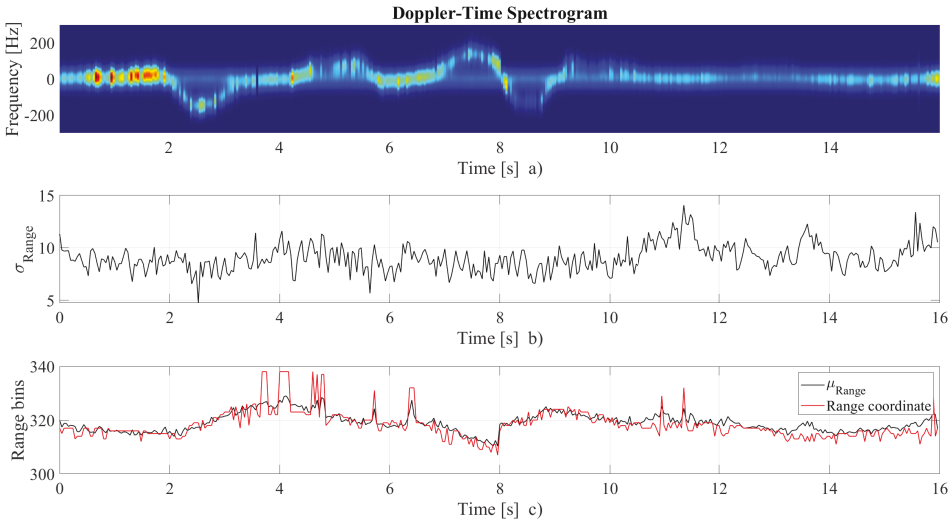

Figure 2.30: Comparison between the range parameters and the Doppler-Time spectrogram: a) calculated Doppler-time spectrogram, b) σ_{range} and c) μ_{range}.

distributed around the maximum detected point. For the range, the values of the parameters are mainly dependent on the range profile of the drone.
In Fig. 2.29 and Fig. 2.30 the results of a single acquisition of the first set are depicted. The value of $\mu_{Doppler}$ along with the Doppler changes in accordance to the position of the center are shown. It is interesting to notice that the values change, going under or upper the mean value, as a results of the tilted orientation assumed by the drone during its movement. In a condition where the drone hoovers up and down in front of the radar system, only $\sigma_{Doppler}$ changes. A different situation holds for the range parameters, which mainly depend on the range profile of the drone.

By combining the extracted information, it is possible to understand how the drone is moving or flying, even if stands at a fixed distance and the relative velocity to the radar systems is zero.

In Fig. 2.31, an example for the second sets of measurements is depicted. In the specific case, the drone is not tilted and the dependence from this condition is removed. Only the distribution of the micro-Doppler values influences the parameters, and the weighted mean value and standard deviation are more stable than in the first case. This means that the geometry of the pseudo-ellipse changes according to the movement, the tilted position, the speed of the propellers, and what are the propellers that cause the speed increase. An example of the evolution of the pseudo-ellipse geometry, for different time values, is depicted in Fig. 2.32, where the (Doppler bins, Range bins) planes captured at different moments are vertically stacked. Fig. 2.32 (a) shows the case of the drone free to fly, Fig.s 2.32 (b) and (c) show two cases when the drone is fixed to the table.

During the test referred to Fig. 2.32 (b), the drone stands along the horizontal plane and is controlled to move, so the propellers change their speed in accordance with the moving direction. As the drone is not able to move, only the micro-Doppler effect of the propellers is collected and the shape of the pseudo-ellipse changes along the

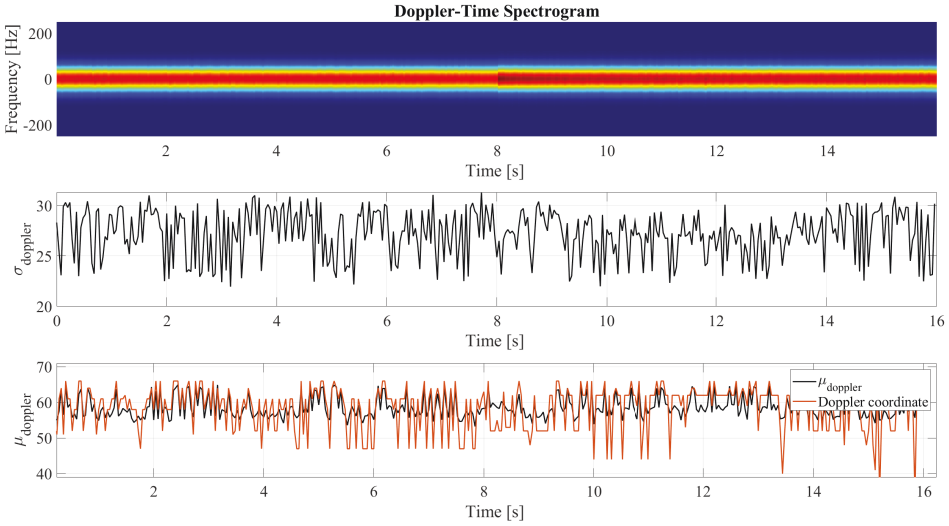

Figure 2.31: Comparison between the Doppler parameters and the Doppler-Time spectrogram for the second sets of acquisitions: a) calculated Doppler-time spectrogram, b) $\sigma_{Doppler}$ and c) $\mu_{Doppler}$.

Doppler axis, because the $\sigma_{Doppler,i}$ change their amplitudes. In the case of Fig. 2.32 (c), the drone is tilted along the roll axis but the propellers rotate with a constant speed, and the result is a pseudo-ellipse with a more constant shape during the whole acquisition. These characteristics of the extracted features are well evident in Fig. 2.32 (a), where the drone is free to fly and both the effects due to the propellers and the drone inclination are combined.

All the above introduced features and their evolution over time can be used to classify the behaviour of the drone: for example, for a hoovering condition these parameters are constant and the pseudo-ellipse does not change its shape. These values and the geometry of the pseudo-ellipse can be used to create a labeled dataset of different flying conditions and can be useful to recognize if the drone has hostile intentions.

This preliminary work was conducted inside our department, so to fully validate the technique we need more acquisition and also outdoor tests with different types of drones. Also, the automotive radar cannot reach long-distance suitable for a real defense system but their characteristics can be very powerful on this topic. A real commercial device based on this technique must be designed to reach an effective long-distance to prevent dangerous situations and classify non only in time but also in range the ways of flyng of the UAVs. The purpose of this work is to provide a proof of concept on how a radar system suited with some characteristics of an automotive radar, such as wavelength, bandwidth and CRT, can be used to solve the drone problem.

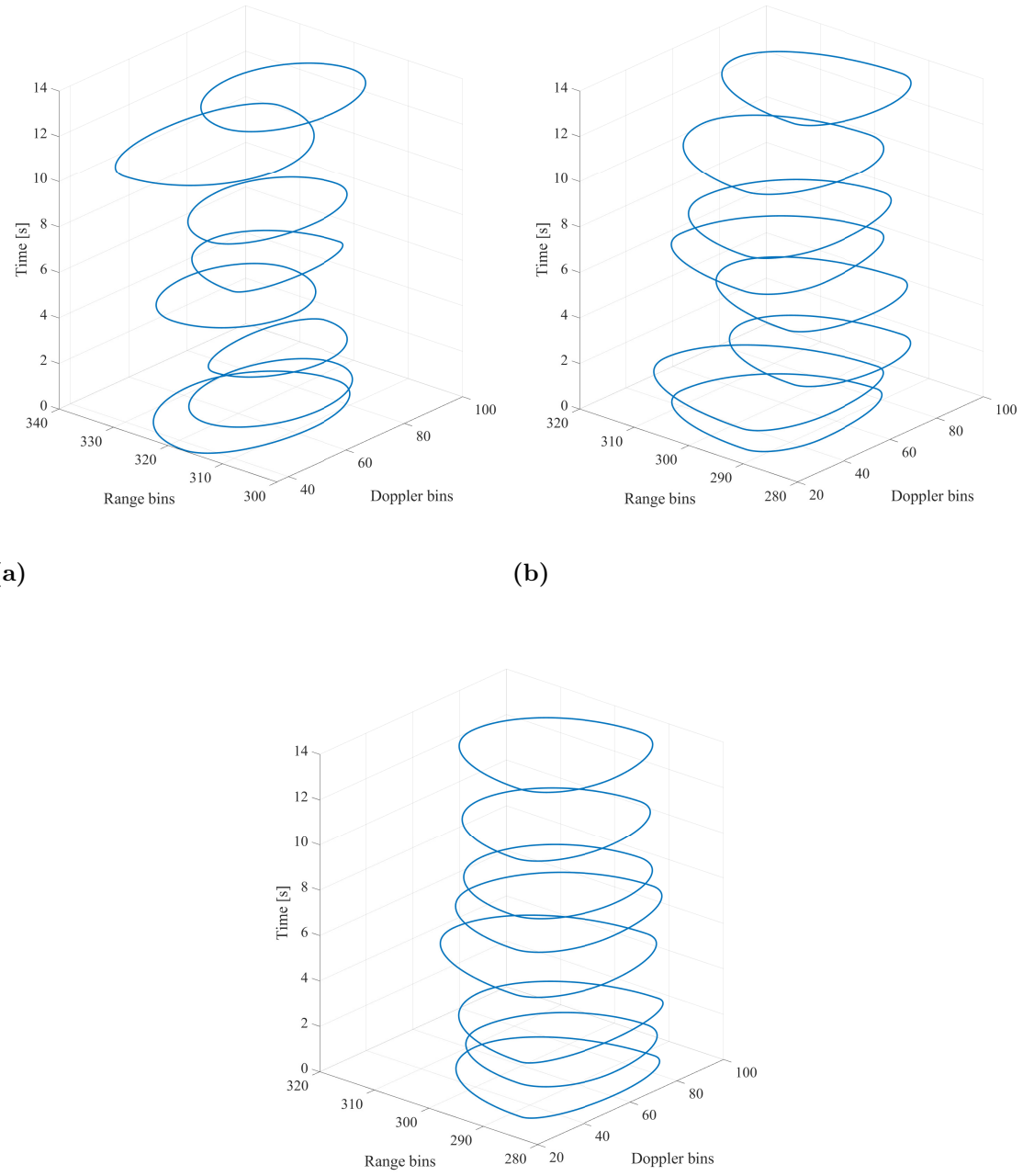

(a) **(b)**

(c)

Figure 2.32: Pseudo-ellipse evolution during the acquisition: (a) drone free to fly (b) drone fixed to the table in the horizontal position (c) drone fixed to the table in the tilted position.

2.6 Chapter conclusions

In this chapter, we show how an automotive radar can be used to classify targets by exploiting their mD features. These devices coupled with suitable signal pro-

cessing and a classification pipeline can provide good results. We show also how different features extraction techniques can be used and we compare the results and the computational costs. We apply also a neural network, which is more complex, to improve the comparison. From the results, we demonstrate how an ad-hoc feature extraction technique provides the same classification results but with a lower computational cost. Of course, this approach can be used only in a particular case (i.e., classify different walking styles), while the other methods are more general. In the last section, we explore the radar capability to detect different drones' ways of flying. We propose a method to extract information, based on features that can be calculated directly on the range-Doppler map to reduce latency calculation. This proposed method is different from applying directly a Machine Learning or Deep Learning technique that extracts features without considering what information is provided with the data. Ad-hoc features are more specific and must be defined in each situation, but these can be simpler to calculate, and the classification latency can be reduced. The future development of this approach is to provide an automatic way of finding the center of the pseudo-ellipse and apply a neural network or a Machine Learning classifier to provide a performance validation of the proposed method.

3

Vibrations measurements with Automotive Radars

Measure and detecting vibration is an important task in different applications, for example in predictive maintenance or the monitoring of the displacement of bridges and buildings. Common sensors used for these purposes are accelerometers [74], inertial platforms [75] and sometimes also video-cameras [76]. Such approaches can be expensive and sometimes difficult to be applied, for example, the cameras are sensitive to dust and dirt and accelerometers need an electronic data-logger to collect information so the system becomes more complex to install. In this field also Radar systems can be applied, for example, Synthetic Aperture Radar (SAR) and Inverse Synthetic Aperture Radar (InSAR) can be used to detect vibrations; both techniques use Radar interferometry and when the system stands on the ground is called Ground Based Synthetic Aperture Radar (GB-SAR) [77, 78]. The GB-SAR are commonly applied to detect vibrations of buildings [79] and are also used to monitor the condition of glaciers and detect landslides [80, 81]. The detection is possible not only with a terrestrial Radar system but also with aerospace-born Radar and in [82, 83] different techniques are illustrated.
In addition to the previous systems, also Automotive Radars can be applied in this field since the small wavelength and the fast CRT can provide high performances in detecting vibrations, also the small form factor of the devices is a plus where is not possible to install big systems. For example, as the respiration and the heartbeat of a person can be treated as small chest vibrations, is possible to detect them with a radar system. If we want to reveal driver drowsiness during the drive time, we can use this approach but inside a car is difficult to install big radar systems. For this reason, automotive radars offer a big opportunity to realize this application in a small environment.
Different radar technologies can be used to detect vibrations, as described in chapter 1, the mD effect is the same in all Radar systems, but the signal processing techniques can be different. In an FMCW Radar, the transmitted signal is a chirp, so the value of f_0 changes along the time. In this modulation scheme, the mD effect is extracted from the phase of the beat signal, and in [1, 84] different approaches are proposed. In this work, the focus is on FMCW Radars, so the discussion will be limited to this type of sensors. Exploiting the information about the vibration-related mD in a Radar system can extend the range of its possible applications, it is possible, for example, to detect the vital parameters of several patients inside a clinical setting [85]. The human heartbeat can be detected because the heart can be seen as a vibrating object that produces a mD signature in the Radar echo. Res-

piration as well, even if with a simpler detection methodology, produces the same effect and can be detected through mD [86, 87, 88]. The use of a Radar for such purposes allows implementing a contactless measurement technique, which can be very powerful when the patients' conditions are not compatible with contact sensors. The same principle can be also applied to monitor the structural health of buildings or bridges [89, 90, 91]. Other industrial applications include the detection of water levels inside a tank [92], or the estimation of tire wear [93].
The transmitted signal wavelength plays a key role in the Radar sensor's ability to detect small vibrations and determines its vibrational resolution [94]. Radars operating at frequencies up to 60 GHz and beyond can detect vibration in the range of hundreds of microns, which is a great result, considering the relatively low cost of the device. Moreover, this technique allows for a high sampling rate, that makes it possible to analyze a wide spectrum of vibrational frequencies, thus making Radar devices even more versatile. Comparing, for example, the results of [95] with [96], it is possible to assert that using a higher frequency makes it possible to detect smaller vibrations. FMCW modulation is also an advantage against the CW technique: if many targets are present in the measurement area, the CW technique does not make it possible to discriminate them along with the range, and the detected vibrational signal will be not accurate. CW Radars are not able to detect multiple target vibrations and they need a more cleared measurement area. For this reason, CW Radars are well suited for the detection of vital signs if only one person is present and there is no clutter situation [97, 98]. For a more general-purpose applications, FMCW Radars provides better performances.

In this chapter, a signal processing technique used to detect vibrations will be presented, and also their performances in applied context will be discussed.

3.1 Proposed Signal Processing Approach

In chapter 1 we describe how a vibrating object produce a mD effect, and in an FMCW Radar, the vibration can be extracted from the phase of the Beat signal [28]. Typically, an FMCW transmitted signal, is composed of up-chirps and down-chirps but, as described in Chapter 1, the tested system can transmit only up-chirps, so the signal model used in this section refers only to this configuration. The transmitted signal for a single chirp can be modeled as:

$$s_T(t) = exp\Big[j\Big(2\pi f_0 t + \pi\frac{B}{T}t^2 + \phi_0\Big)\Big] \tag{3.1}$$

where f_0 is the starting ramp frequency, t is the so-called fast-time, ϕ_0 is the initial phase, B the bandwidth, and T the chirp time (fast-time). Under the model described above, it is possible to write the reflected signal as:

$$s_R(t) = \rho \cdot exp\Big[j(2\pi f_0(t-\tau) + \pi\frac{B}{T}(t-\tau)^2 + \phi_0)\Big] \tag{3.2}$$

where ρ a generic amplitude coefficient and τ the delay of the received signal, which

is related to the distance by the relation:

$$\tau = \frac{2}{c} \cdot R(t) = \frac{2}{c} \cdot [R_0 + x(t)] \tag{3.3}$$

where $R_0 + x(t)$ is the distance of the vibrating target, R_0 is a fixed distance and $x(t)$ is the vibration displacement. As known, in an FMCW Radar the transmitted signal is multiplied by the received signal and from equations (3.1) and (3.2), after a low-pass filtering, the Beat signal can be obtained:

$$s_b(t) \approx \rho \cdot exp\Big[j\Big(2\pi\frac{B}{T}\tau t + 2\pi f_0 \tau\Big)\Big] \tag{3.4}$$

In equation (3.4), τ^2 is neglected because smaller than τt, and also $x(t)$ can be assumed constant inside a chirp, so the variation can be seen only along with different chirps (slow-time dimension). As also described in [99], it is possible to write the Beat signal in terms of the slow-time and the fast-time:

$$\begin{aligned} s_b(iT + t) &\approx \rho \cdot exp\Big[j\Big(\frac{4\pi\frac{B}{T}R_0}{c}t + \frac{4\pi f_0 R_0}{c} + \Big(\frac{4\pi\frac{B}{T}t}{c} + \frac{4\pi f_0}{c}\Big) \cdot x(iT)\Big)\Big] \\ &\approx \rho \cdot exp\Big[j(2\pi f_B t + \Psi_i)\Big] \end{aligned} \tag{3.5}$$

In the previous equation, f_B is the Beat frequency related to the main distance of the target R_0, and Ψ_i depends on the vibration signal.

Starting from a static target that only vibrates, its vibrations produce the effect of phase modulating the Radar signal, and for this reason, the Radar's ability to detect a remote static object's vibration relies on the possibility to analyze the received signal's phase variations in time. We can express the relationship between target motion and phase signal as follows:

$$\Psi_i = \frac{4\pi R_0}{\lambda_0} + \frac{4\pi}{\lambda_c} \cdot x(iT) \tag{3.6}$$

where:

- R_0 is target distance from the Radar in meters;
- $x(iT)$ is the target displacement in time;
- λ_0 is the initial chirp wavelength;
- λ_c is the central chirp wavelength.

The minimum value of $x(t)$ able to produce a $\Psi_i(t)$ phase variation is:

$$\Delta_\Psi = \frac{\lambda_c}{4\pi}\Delta_x \tag{3.7}$$

where:

- Δ_Ψ is the minimum detectable phase;
- Δ_x is the minimum target displacement able to generate a phase variation.

From equation (3.7) we can assert that the detection resolution is strictly bounded to the transmitted signal characteristics and is possible to detect sub-millimeters vibrations even by using signals having a wavelength in the millimeter range.
In a real application scenario, the Beat signal is made up of many terms originating from the target (signal of interest), and from all the other objects that are in the Radar's range of sight. The Beat signal can be seen as a summation of terms representing the vibrational state of all the objects detected in the scene. It is subsequently mandatory to isolate the relevant target's contribution. Having a MIMO capable Radar, we can use both distance and azimuth information to locate the target, this approach improves the capability of the Radar to discriminate different objects.
The Beat signal can be modeled as a sum along the range-azimuth plane, by indicating with $s_{b_{r\theta}}$ the single Beat signal coming from an element of the Range-angular direction map. It is possible to write the following relation:

$$s_b(R, \Theta) = \sum_{r=1}^{Rm} \sum_{\theta=1}^{\theta_n} s_{b_{r\theta}} \tag{3.8}$$

where R_m is the number of range bins in the range direction and θ_n is the number of angular bins, which depends on the angular resolution and the MIMO configuration. At this point, the importance of being able to separate targets is simple to understand, the improvement in range and angular resolution can separate different Beat signals coming from different targets. If the algorithm can separate much more targets, it is possible to extract with more accuracy the vibration signal; otherwise, the sensor detects the vibrations of all the targets summed together. The practical implementation of the algorithm starts from the raw samples coming from the ADCs (one for each receiver). These samples have the form of complex numbers, a vector of them represents the Beat signal evolution over time. Data can be rearranged in an $n \times 4$ matrix, where n is the number of samples collected during the acquisition and 4 is the number of receivers used in this setup. For the moment we do not use the full MIMO capability of the sensor. We may think of this data as being cube-shaped along three main axes:

- the Fast-Time axis: samples of a single chirp;
- the Spatial Sampling axis: samples collected from different ADCs;
- the Slow-Time axis: samples from different chirps.

The target position is determined by executing an FFT analysis in the fast-time and Spatial Sampling axes. If the target is not moving, we can extract a data vector from slow-time which corresponds to the detected position. Having determined the position of the target, we can calculate the phase information as stated in equation (3.6). After unwrapping the phase signal, we extract the vibrational information by inverting the formula in the equation (3.6) and removing the average value. The processing steps used can be graphically summarized by the flowchart shown in Fig. 3.1.
To detect the position of the target a range-azimuth map is calculated. Since the target is not moving, its position can be identified by the same bin for all the measurements. This map is calculated only once, for identifying the position used during

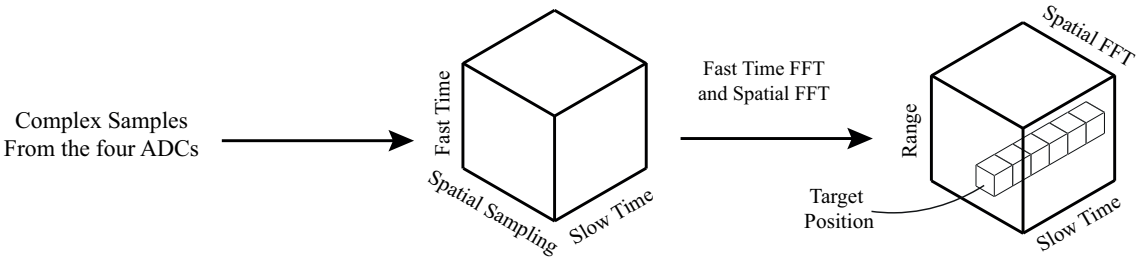

Figure 3.1: Radar signal processing flowchart.

the processing. Fig. 3.2 shows an example of this map. The sense of performing an FFT, or a bidimensional-FFT in the MIMO case, is to select a specific $s_{b_{r\theta}}$ component whose phase is our vibrational signal. This maximum-likelihood method can separate the echo of the desired target from the others.

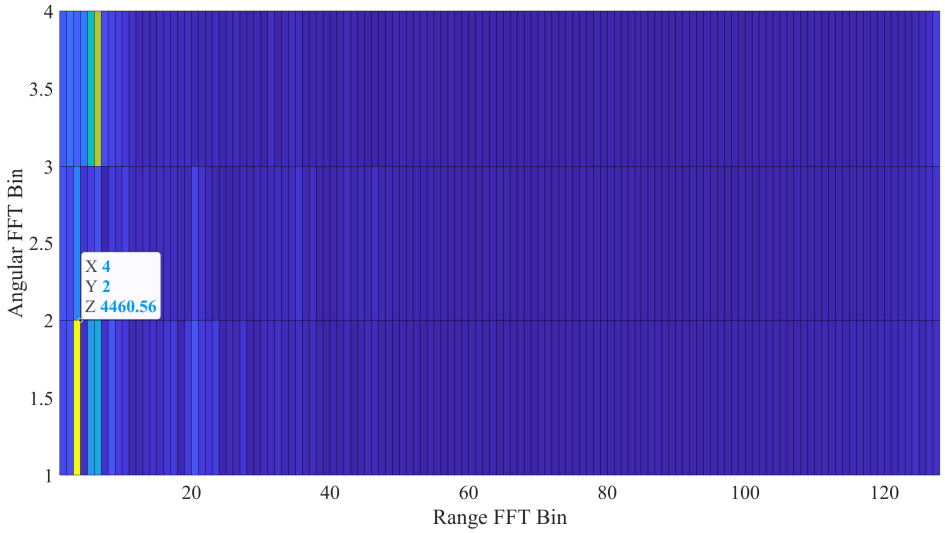

Figure 3.2: Range-angular direction map.

From the figure, it is also possible to understand how the environment affects the algorithm capability. If only one target is present, it is simple to detect it and extract its vibration signal. If more objects are present, or we are analyzing a complex target such as a bridge we need to accurately choose which bins correspond to our target so the identification can be more complex.

3.2 Preliminary Tests

To validate the proposed method, at the beginning we consider the simplest version of the algorithm. For the preliminary tests, the MIMO is not used and the beat signals coming from the four receivers lines are summed together to improve the signal-to-noise ratio. Referring to Fig. 3.3, the sampled values of the beat signals are stored in a matrix, where along the fast-time are stored the samples related to a chirp, while along the slow-time are stored data related to the different chirps.

To evaluate the phase variation of the beat signal in time, a row of the matrix is selected, this is related to the distance of the target. The phase variation among the different samples on this row represents the phase change of the beat signal due to the target vibration.

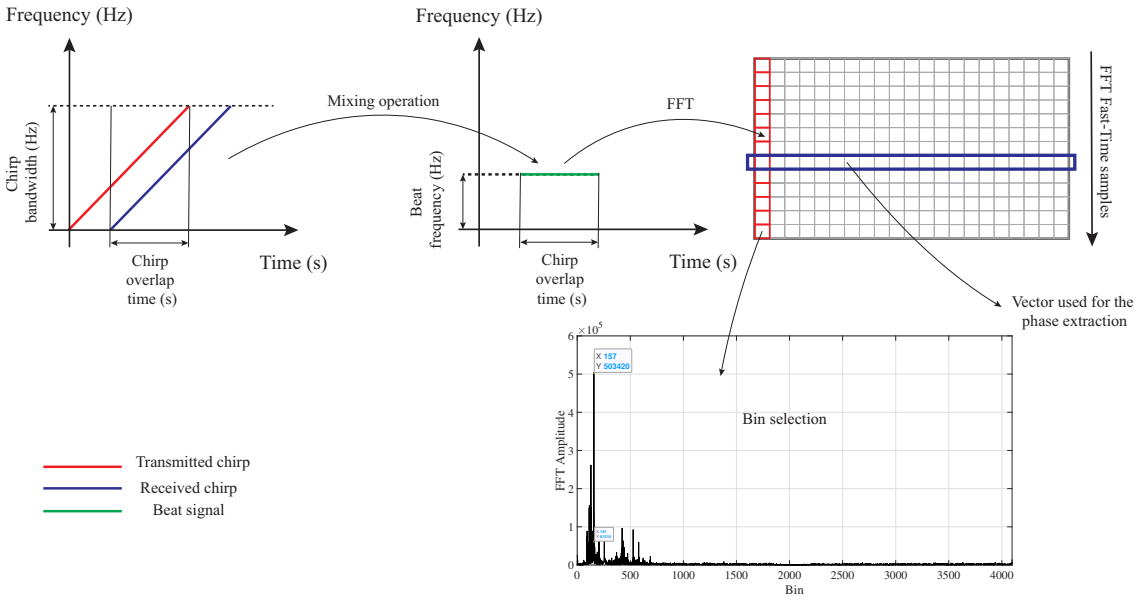

Figure 3.3: Target position detection without the MIMO usage.

The proposed method is based on a fundamental consideration, the target must not move during the measurements. This is because if the target moves, a signal saturation may occur in a sensitive receiver for heartbeat detection because of its limited dynamic range, making it impossible to detect any signals [100, 101]. This case is common when we try to measure vital parameters as the human body always moving. In the case of mechanical systems, this movement can be controlled so the effect can be neglected. The steps for extracting the phase information are:

- Calculate the FFT along the fast-time and identify the target position;
- Extract the complex samples of the FFT for the selected range bin;
- representation in time and frequency of the phase signal.

The configuration of the radar system is based on two main parameters, the observation distance, and the best resolution. To reach a good target identification the range resolution value must be smaller as possible, but the configuration of the system is a compromise between all the parameters. The maximum distance R_{max} is related to the beat frequency f_{beat} through the equation:

$$R_{max} = \frac{f_{beat} \cdot c}{2 \cdot Slope} \tag{3.9}$$

where c is the speed of light and $Slope$ is the slope of the FMCW signal ramp. In this case, given that the maximum value of f_{beat} is equal to the maximum sampling frequency, only the $Slope$ parameter may be chosen for calibration. The phase signal, used in the analysis, is a signal composed of a value for each chirp and therefore its sampling time coincides with T_{chirp}:

$$f_{SamplingFFT} = \frac{1}{T_{chirp}} \tag{3.10}$$

This also determines the maximum frequency of observed vibration, the adopted configuration tries to reduce T_{chirp} to the minimum value and to maximize spatial resolution and definition. Based on these constraints, the configuration parameters reported in Tab. 3.1 were chosen.

Table 3.1: Radar Parameters

Parameter	Value
Start Frequency	77 GHz
Idle Time	100 μs
Slope	11.587 MHz / μs
Radar Bandwidth	3998,9 MHz
$f_{sampling}$	12 MHz
$t_{periodicity}$	60 ms
n° ADC Samples	4096
T_{Chirp}	345.12 μs

From this calibration the maximum range distance is around 80 meters and is possible to measure vibrations with a maximum frequency of 2.246 KHz.

3.2.1 Numerical Simulations

The experimental performance evaluation starts from a numerical simulation and to represent a realistic trend, the data of a real earthquake, which occurred in Perugia on 30 October 2016, acquired through seismic accelerometers, was taken into consideration [102]. Based on the acceleration data, the displacement signal, which is the entity of the vibration, was obtained through a double integration. In the simulation, the displacement signal was attributed a maximum amplitude of the order of hundreds of microns, and it was assumed that the analyzed target was at a distance of three meters. The displacement signal $R(t)$ depicted inside Fig. 3.4 and his sampling frequency is equal to T_{chirp}. The beat frequency will be given by:

$$f_{beat}(t) = 2 \cdot \frac{R(t) \cdot Slope}{c} \tag{3.11}$$

The value of $f_{beat}(t)$ obtained for each $R(t)$ is used to build a sinusoidal signal $sb(t)$ that simulates the target:

$$s_b(t) = exp(-j2\pi f_{beat}(t)t) \tag{3.12}$$

The reference displacement is depicted inside Fig. 3.4, this signal represents the oscillation obtained from the accelerometers. In Fig. 3.5, we can find the result of the proposed technique and the signals show how the trend is reconstructed with very good performances. From this simulated result, we can move to a real implementation.

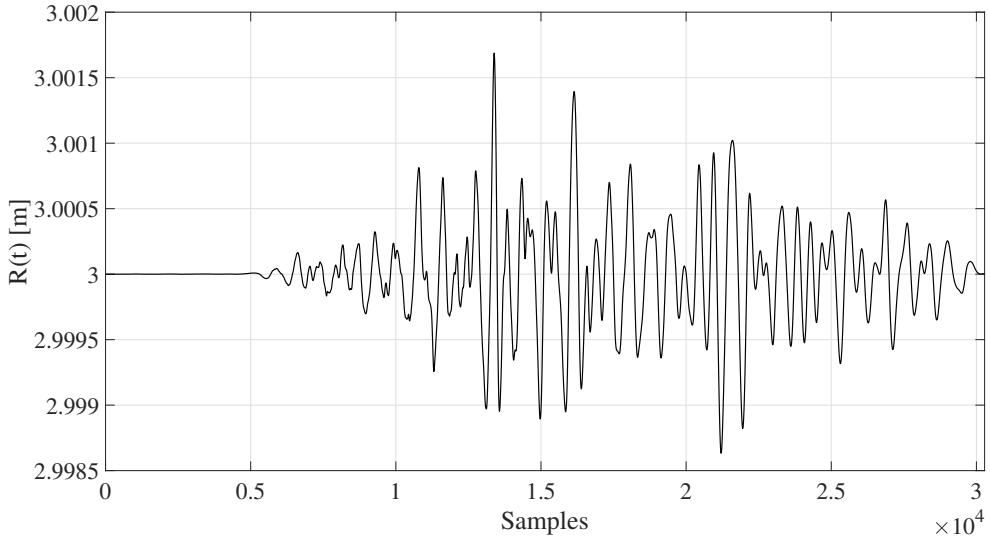

Figure 3.4: Simulated displacement signal obtained from the accelerometer information.

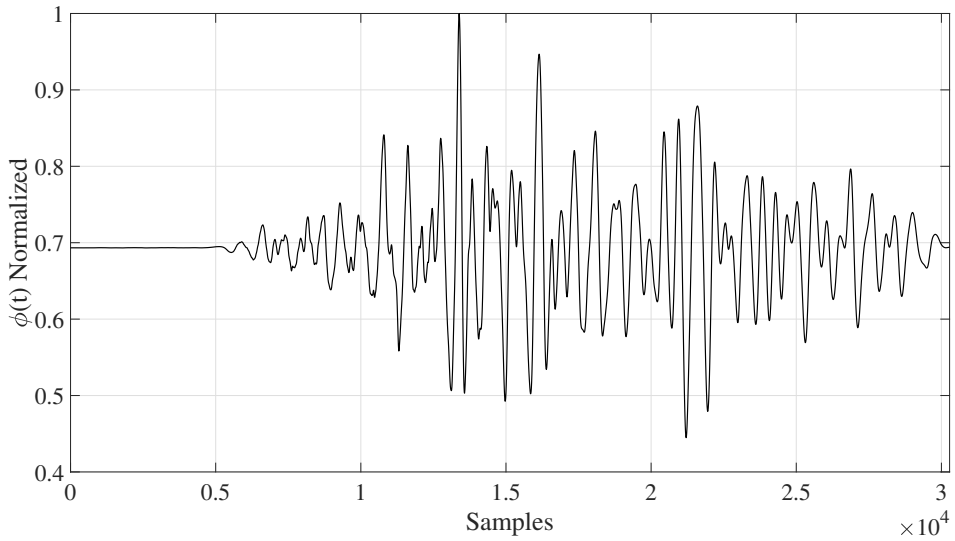

Figure 3.5: Phase signal provided by the vibrational algorithm. The phase value was normalized by dividing by the maximum value.

3.2.2 Laboratory and Outdoor tests

After the simulation, we move to a practical laboratory setup implementation, the target used is a metallic board where an electro-acoustic transducer is fixed to them. The transducer is connected to a signal generator that provides a train of rectangular pulses with a 50 Hz frequency and a 50 % duty cycle. In the measurement setup, the board was placed at a known distance of about 2.59 m from the radar system so it is easy to locate its position inside the FFT range. The setup is depicted inside Fig. 3.6.
The obtained results are shown in Fig. 3.7 where in the first graph is possible to find

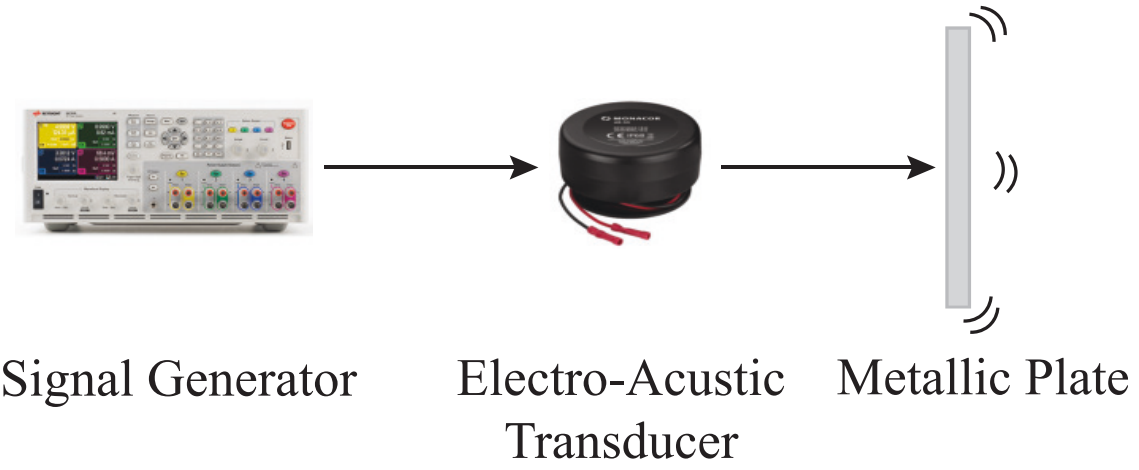

Figure 3.6: Schematic representation of the setup used during the laboratory preliminary tests.

the trend of the phase along time, being the acquisition time of about six seconds. In the second it is shown shown the conversion of the phase into displacement, for a reduced time interval. Finally, in the third, the FFT of the displacement signal was obtained to highlight the harmonic vibration components, to verify the frequencies triggered by the transducer. The most interesting frequency components are at 53.1 Hz and its multiples. The trend of the phase signal over time makes it possible to identify a periodicity of about 0.02 s. This is consistent with the type of pulse supplied to the transducer.
The last part of the work is aimed at an application in a real context, carrying out measurements on a continuously stressed structure as a motorway bridge. The sensor configuration is the same used in the laboratory environment and two different tests were performed: in the first one the vibration of the main metal beam of the bridge was measured, while in the second one the vibration of a shelf to support the beam was considered. As introduced before, the position of the beam and the shelf were firstly identified in the FFT Range to extract from the data matrices the displacement bins. To validate the obtained results, two videos were recorded showing the passage of the various vehicles on the bridge. There is no perfect synchronization between video and radar acquisitions, but the video is still important for data validation. Fig. 3.8 refers to the radar pointing at the center of the metal beam that supports the bridge. The graph shows two important oscillations spaced about 4 seconds apart. The analysis of the video shows two vehicles that pass on the bridge with a temporal distance of 4 seconds, causing bridge oscillation. The detected displacement is in the order of tens of microns.

3.3 Performances validation

The produced results make it interesting to study which performances can be reached by the sensor, in terms of accuracy, in measuring vibration displacements and frequency. Also, the sensor used is equipped with MIMO, so this technology can be

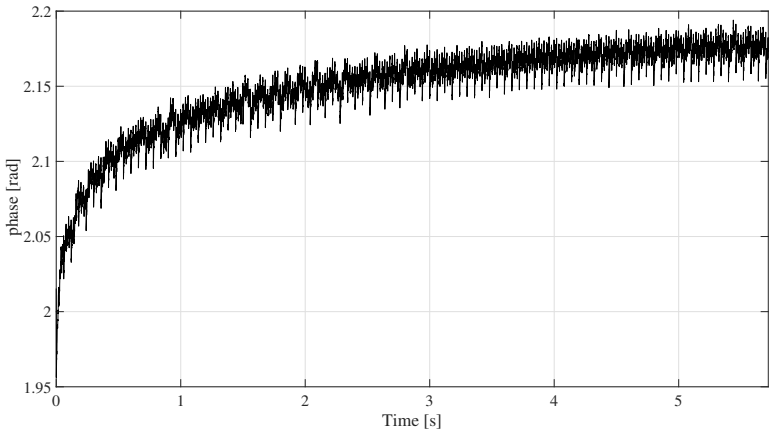

(a)

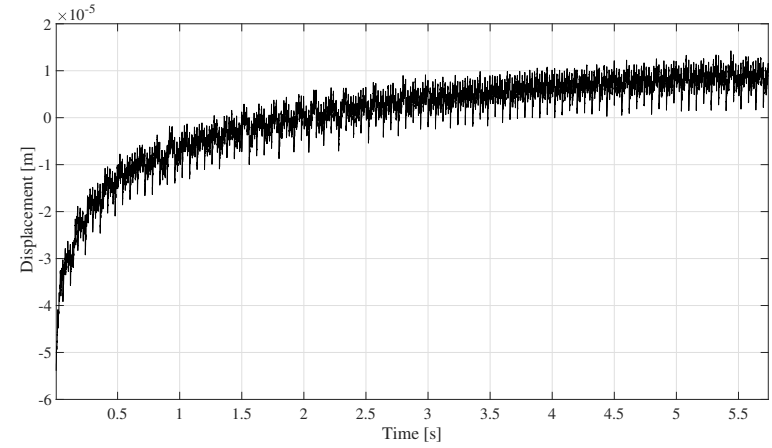

(b)

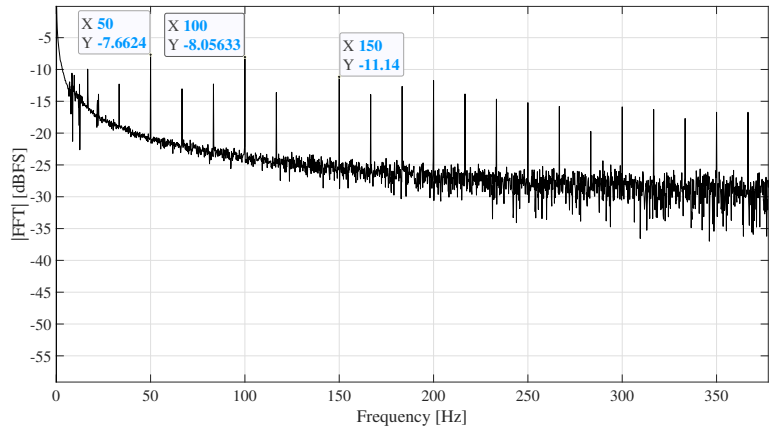

(c)

Figure 3.7: Results obtained during preliminary tests: a) signal phase, b) calculated Displacement, c) Displacement FFT.

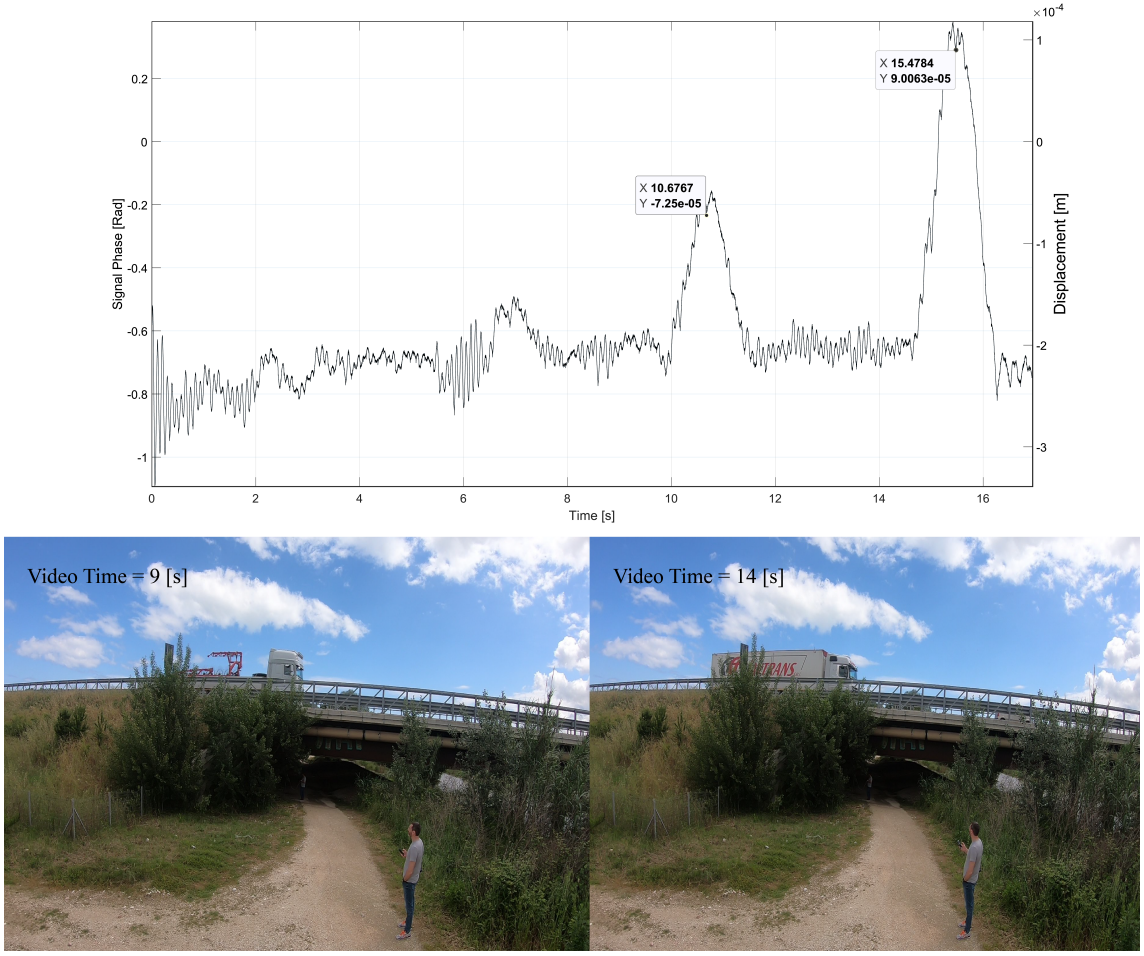

Figure 3.8: Vibrational test on the main metal beam of the bridge.

applied as in the previous work this is not done. This performance analysis can be conducted with a setup built for this purpose and the area chosen for the measurements is a mechanical measurement laboratory. Inside this area, not only the measurement setup is present, but also other instruments and objects, this means that the area is not clean but suitable to reproduce a generic environment where many objects can be present and not only the chosen target.
The measurement setup includes a signal generator, a mechanical shaker, an oscillating panel (the target), and a laser vibrometer. The dimension of the panel is 46 $\times$ 34.5 cm and is made with a sandwich in fiberglass and the core is in polyurethane foam. The facing surface in the direction of radar and laser vibrometer is coated with aluminum tape thick of 0.5 mm. The generator is used to generate a sinusoidal signal with a given stable amplitude and frequency where the signal's parameters are varied throughout the tests. The generator is connected both to an ADC (part of the laser vibrometer system) and to a mechanical shaker. The latter is bound to the aluminum-coated panel which is the oscillating target in our setup, which is shown in Fig. 3.9.

The position of the target is chosen in a map similar to the one in Fig. 3.10 which shows the angular-range information in terms of FFT bins, not the converted Range-

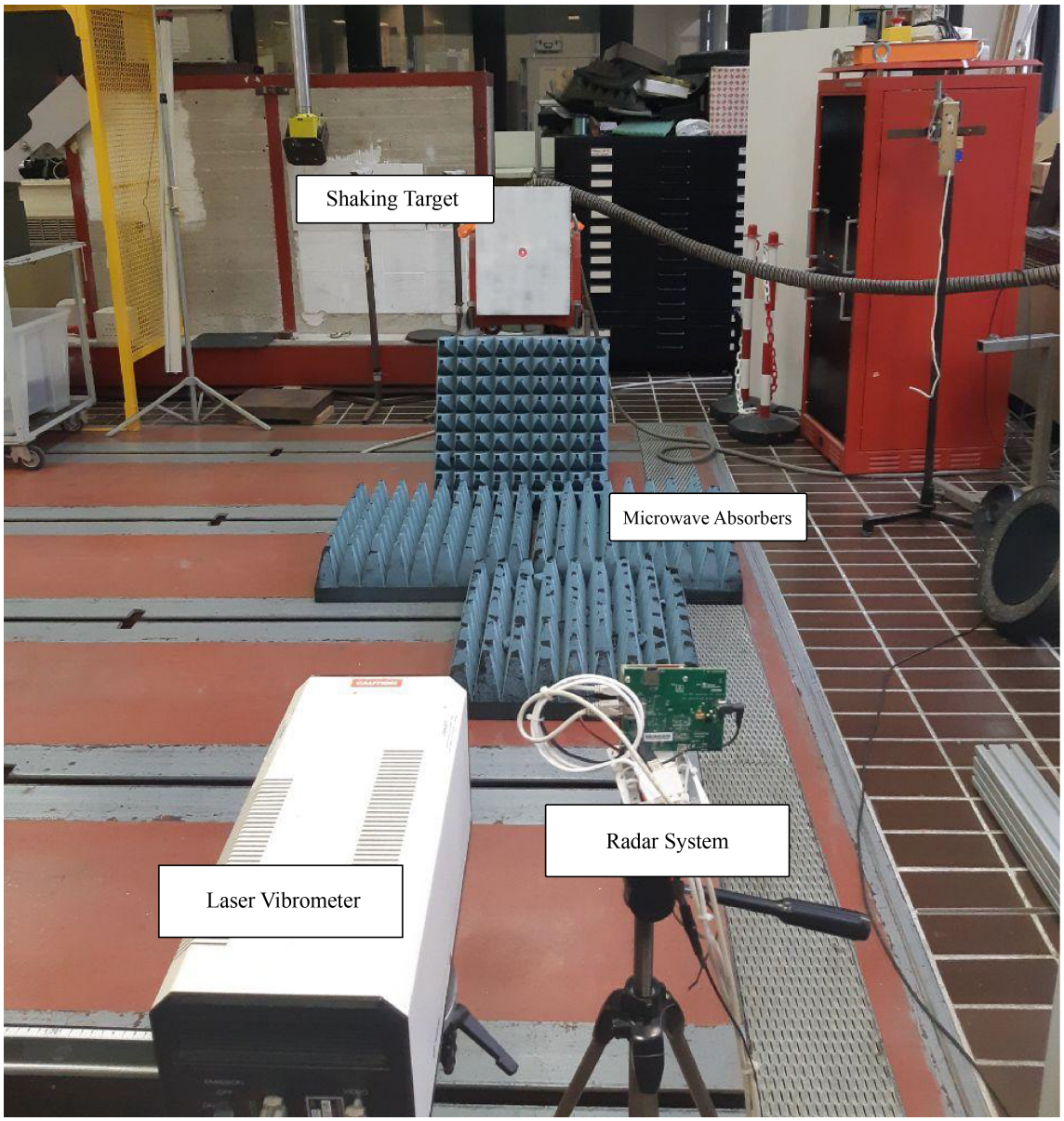

Figure 3.9: Measurement setup with the radar and the laser vibrometer.

Angle axis. The target used stands along with the angular bin no. 1 and the range bin no. 46. As it is also evident, the target structure stands extends over three range bins (46, 47, 48), but the correct one is only the first, which gives the position of the vibrating panel.

To avoid the Radar receiving spurious reflections from the shaker support and the floor, a set of microwave absorbers have been placed on the measurement field. As mentioned above, each element that stands inside a "pixel" contributes to the beat signal, so even to the extracted vibration. For example, if we do not exclude the support of the panel, the algorithm will also detect its vibration. Tab. 3.2 shows the Radar parameters configuration, which is selected to easily identify the specific object chosen in our experiments to be the Radar target, i.e., a wooden aluminum-coated panel, among other objects located nearby in the lab. For this purpose a

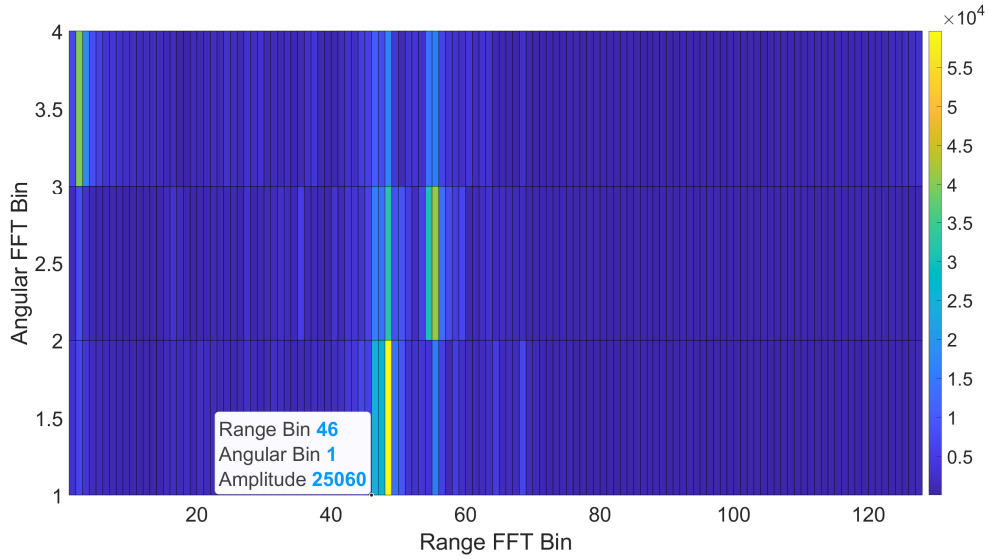

Figure 3.10: Range-angular direction map.

resolution of 0.067 m is used, a value that is comparable to the panel thickness.

Table 3.2: Radar Parameters

Parameter	Value
Idle Time	100 μs
ADC Valid Start Time	6 μs
ADC Sampling Time	63 μs
Used Radar Bandwidth	3.99 GHz
$t_{periodicity}$	976 μs

Radar and laser Vibrometer are 3.013 m far from the target and are operated simultaneously. The distance value is the range measurement of the Radar, such a distance value is taken from the Radar detection so the error is the resolution range. Both measurement systems are aiming at the shaking panel. The laser vibrometer sight of the target is greatly improved by using the laser spot as a reference. On the other hand, the Radar aiming is obtained by orientating the Printed Circuit Board (PCB) so that the transmitter's antenna boresight axis is lined-up with the center of the shaking panel. Two measurement campaigns have been carried out. In the former, a setup is used like the one shown in Fig. 3.9. In the latter, the microwave absorbers are removed and the position of some objects in the Radar field of view is changed, to verify the repeatability of the measurement results and their reliability. During each measurement campaign, the signal generator's frequency and amplitude are chosen within a set of possible values, thus changing the target's shaking frequency and displacement accordingly. In Tab. 3.3 all these values are reported: they are chosen to produce vibration with unknown amplitude and even non-integer values of their frequency.
Following the system setup, measurements with both instruments used at the same time are performed, in order to determine the target vibration frequency and dis-

Table 3.3: Generator's signal amplitude (voltage) and frequency settings.

Voltage [V]	Frequency [Hz]
1.5, 1, 0.5, 0.25, 0.125	21.5
1.5, 1, 0.5, 0.25, 0.125	13
1.5, 1, 0.5, 0.25, 0.125	4.7

placement. Each measurement lasts for 50 seconds. The Radar sensor's signals are collected and saved on a storage memory, to be processed off-line where a Matlab processing will extract frequency and displacement magnitude versus time. A sample result is given in Fig. 3.11. The number of samples collected by the Radar system is different from the laser vibrometer. For the former device, the number of samples depends on the number of transmitted measurement chirps (in this case, 51200); for the latter, the number of samples depends on the configuration (4096). The result is evident in the harmonic analysis, where a different frequency resolution is obtained. The sampling frequency of the vibration for the Radar system is 1024 Hz, and it is 1280 Hz for the laser vibrometer. So, the frequency resolution is 0.02 Hz and 0.3125 Hz, respectively. This must be taken into account during the analysis of the results.

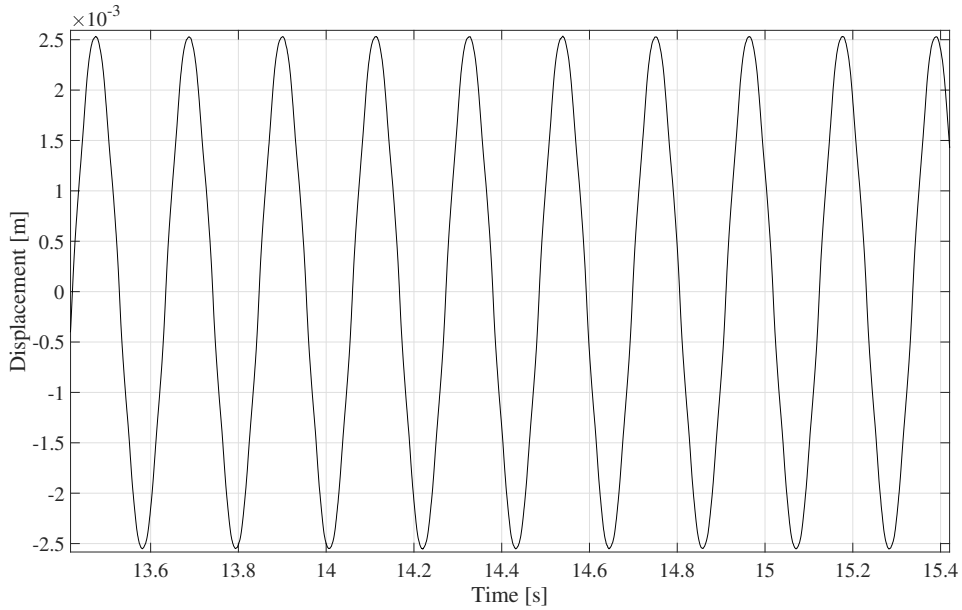

Figure 3.11: Target displacement in time, measured by the Radar.

To evaluate the Radar sensor performances in measuring the target displacement, the reference laser vibrometer is used, which can determine the target shaking displacement in real-time. The target shaking frequency as measured by the Radar equipment is directly compared with the signal generator displayed value. In Fig. 3.12 we can find an example of the vibrometer console output used for the laser measurements. The values used in the experimental evaluation are taken from such a console. In the first shell is depicted the magnitude of the FFT calculated on the measurement of the vibrometer, in the second the reference signal expressed in Volts

provided by the signal generator, and in the third, the measurement vibration result expressed in speed.

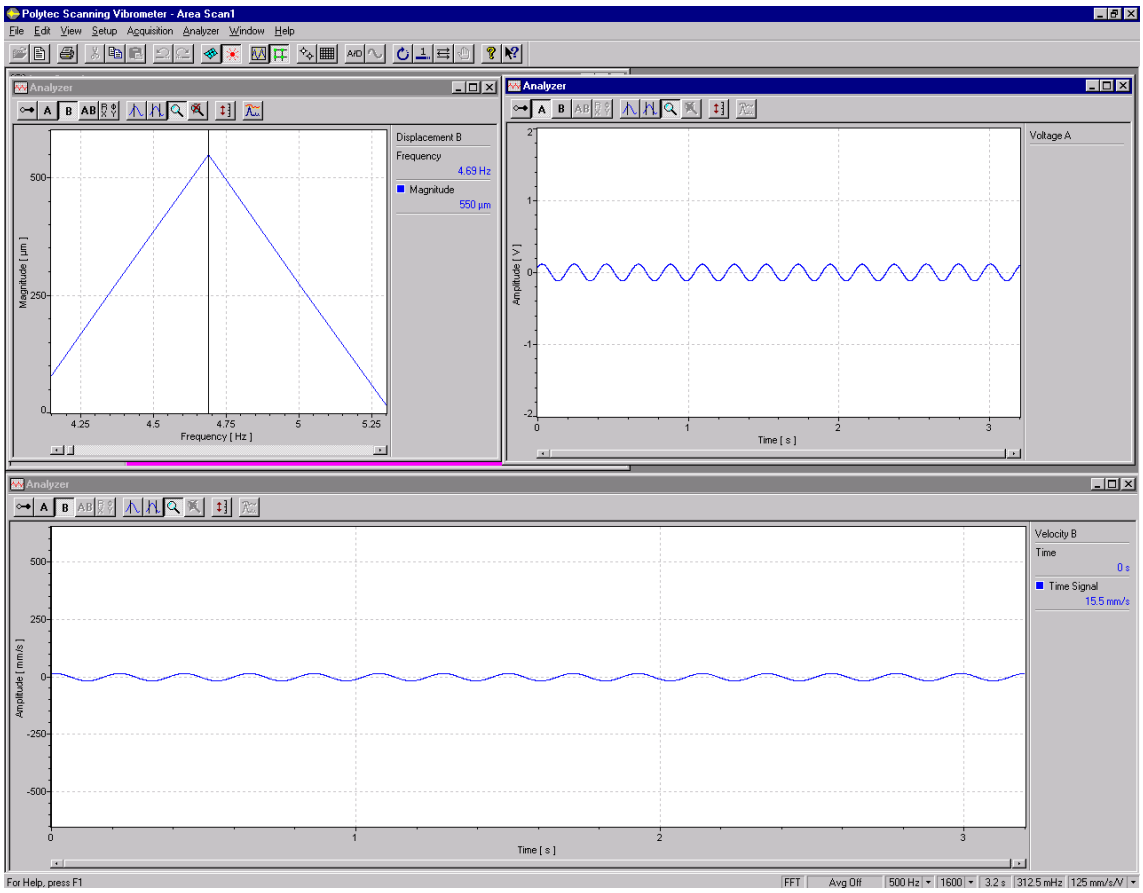

Figure 3.12: Vibrometer software display used to read the measured values. In the first shell is depicted the Magnitude of the detected displacement, in the second the reference voltage signal coming from the signal generator and in the third the amplitude of the detected displacement.

For each couple of frequency and voltage settings, ten measurements are repeated in the first setup, and two in the second one. For each signal, the value of the positive relative maxima was calculated; from the average of these values, it is possible to obtain the average measure of the target displacement. This is possible because the signal generator does not change the generated signal along the time, so it is possible to assert that the movement of the target remains the same during all the fifty seconds of the measurement.
In Tab. 3.4 and 3.5 the average values and standard deviations of the measurement data obtained from the vibrometer ($\overline{x}_v$) and from the Radar sensor ($\overline{x}_r$ and σ_r, as a result of signal processing) are reported.
Starting from the frequency results, these are the same at all voltage values, and for this reason Tab. 3.4 reports one value for each frequency. The laser vibrometer and the Radar system have different resolutions in frequency, but anyway it is possible to state that the Radar system produces very similar results to the vibrometer.
The results obtained from the second setup are the same as the first one. So, the

Table 3.4: Measurement results of the target frequency obtained in the first setup.

Signal Gen.	**Vibrometer**	**Radar**
Frequency [Hz]	$\overline{x}_v$ [Hz]	$\overline{x}_r$ [Hz]
21.5	21.56	21.49
13	13	13.13
4.7	4.7	4.69

effect of other objects located inside the scene and of the ground do not degrade too much the attained measurements.
Tab. 3.5 reports the result for the detected displacement: even in this case, for the first and second setup, similar results are obtained so in the table only the former are presented.

Table 3.5: Measurement results of the average target displacement obtained in the first setup. The last column reports the difference between the Radar and the vibrometer measurement values

Signal Gen.	**Vibrometer**	**Radar**		Δ_d
Frequency [Hz], Voltage [V]	$\overline{x}_v$ [mm]	$\overline{x}_r$ [mm]	σ_r [mm]	[mm]
21.5, 1.5	1.69	1.83	0.015	0.14
21.5, 1	1.08	1.15	0.004	0.07
21.5, 0.5	0.57	0.61	0.003	0.04
21.5, 0.25	0.28	0.32	0	0.04
21.5, 0.12	0.14	0.16	0	0.02
13, 1.5	2.50	2.88	0.005	0.38
13, 1	1.66	1.95	0.016	0.29
13, 0.5	0.83	0.92	0.001	0.09
13, 0.25	0.41	0.49	0.004	0.08
13, 0.125	0.20	0.25	0	0.05
4.7, 1.5	6.83	7.20	0	0.37
4.7, 1	4.62	4.96	0.012	0.34
4.7, 0.5	2.28	2.53	0.008	0.25
4.7, 0.25	1.12	1.16	0	0.04
4.7, 0.125	0.55	0.64	0.001	0.09

In the second measurement setup, we obtain similar results, either for displacement and frequency. By the analysis of the data, it is possible to assess that the Radar system gives stable measurement results, with a resolution of 100 μm.
The Radar used is a MIMO device, so it is possible to identify the position of the target not only in range but also in angle. This is helpful to resolve near targets and reduce the interference, especially in a radar-noisy environment. With respect to [103], the signal processing is similar but in this case the Radar is not able to discriminate targets at the same distance. This means having a degradation of the measurements. For analyzing this degradation we compare the laser vibrometer measurement with the Radar, using the MIMO identification or not. With the setup

used, the position of the target is "46" along the range FFT axis and "1" along the angular FFT axis. All the results presented are obtained from these values. In the case without MIMO, only the range is present, so the identification of the position is the range bin (46). Fig. 3.13 depicts the result of applying MIMO identification or not.
Observing Fig. 3.13, it is possible to see how the exploitation of the MIMO capability improves significantly the quality of the measurements. The signal generated by the generator is sinusoidal, and the most similar signal is obtained when applying MIMO. Without using MIMO, the signal is still periodic but with noticeably high amplitude and phase distortion. In a measurement area where multiple objects are present and not only the designated target, it is very difficult to obtain a clean measurement of displacement and vibration frequency. In some cases, the measured displacement is completely wrong and, following the model given in Equation (3.8), this is the result of summing together all the contributions coming from many targets at the same distance.

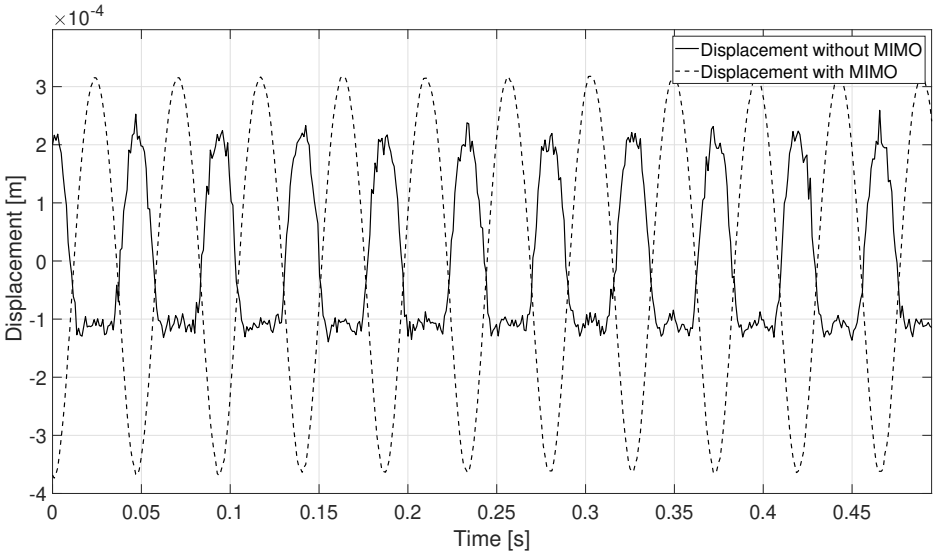

Figure 3.13: Measurement results for the test 21.5 Hz - 0.25 V, when using the angular identification (enabled by MIMO) or not.

Inside equation (3.8), the beat signal is the sum of multiple terms. With the application of the MIMO transmission it is possible to discriminate each component not only in range but also in angle. If the angular discrimination is not considered, the equation becomes:

$$s_b(R, \Theta) = \sum_{r=1}^{Rm} s_{b_{r\theta}} \tag{3.13}$$

Equation (3.13) considers all the angular components of the signal; conversely, inside equation (3.8) the angular terms are not summed together so this improves the performances of the detection. The result is a beamforming of the receiver antenna diagram, which allows separating the elements along the angle.
Another type of analysis can be focused on the harmonics of the detected vibrations. The signals' spectra are reported in Fig. 3.14.

Comparing the results in terms of the detected vibration frequency, the laser vibrometer and the Radar system with MIMO technique achieve similar results. The scale of the spectral amplitudes shown in Fig. 3.14 is in dB full scale [dBFS] for a better comparison. Both the systems can detect the main frequency of vibration and the other multiple harmonics with a decreasing trend. In the case without MIMO, the detected maximum value is not always correct: in the example shown, the main frequency is around 32 Hz when the vibration is set to 4.7 Hz. The application of the algorithm with the range detection only can reach good performance when the measurement area is clear from other objects, and there is only the desired target inside the chosen range bin.

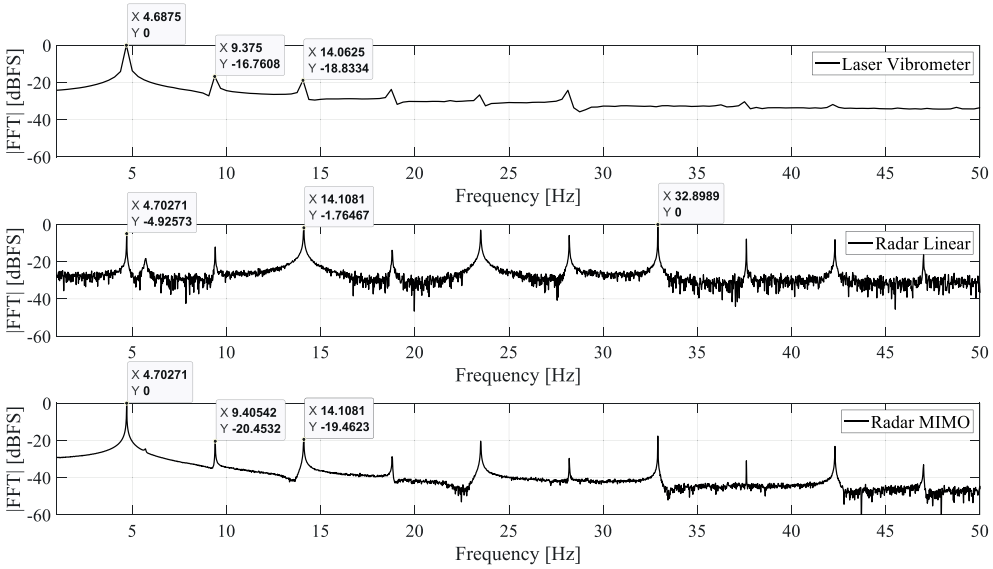

Figure 3.14: Harmonics comparison between the three measurement techniques used. The depicted spectrum is limited to 50 Hz. The vibrational frequency detected is very similar in all the cases.

From the results, it is possible to see how the Radar can detect with good performance the vibration frequency and the displacement of the target, the latter one with a resolution of hundreds of microns. Moreover, when the microwave absorbers are removed from the measurement scenario, thus increasing Radar noise and clutter, the performances remain the same. Comparing all the measurements with those provided by the vibrometer, a mean arithmetic value of Δ_d is calculated and results of 0.15 mm. This is bigger than the error stated in [99], but the setup used in this work is more realistic and the target is located at a greater distance from the sensor. The comparison between the two Radar techniques shows how the correct detection of the position of the target is important to improve the performance of the Radar-based system. The angular detection can somehow filter out the undesired targets, and this allows to obtain a better quality Radar measurement.

3.4 Application on measuring and detect Vital Parameters

With the same signal processing technique is possible to monitoring of the vital parameters of a person in non-contact mode. Measuring HR and Respiration Rate (RR) with a non-contact technique is very important in applications like drowsiness detection inside a vehicle [104, 105], or in a hospital where contact sensors cannot be applied. From the results described in section 3.3 we demonstrate how the radar system can detect very small vibrations even at a distance of meters so is interesting to see which performances can reach the automotive radar in vital parameters detection. To demonstrate the capability of the sensor and the signal processing technique we conduct many tests with different setups. The beginning work is described in [106], in this case, we need a reference method so also a video system and a pulse-oximeter are used for the validation. High precision in the definition of the target position is needed for the subject's HR detection, since, as described in the previous section, the heart activity is studied through the analysis of the FFT phase. Accuracy can be improved by exploiting MIMO, and, as discussed in [107], MIMO turns out to be extremely effective for the simultaneous monitoring of the HR of two subjects thanks to the possibility of identifying the angular position of the subject.
Each transmitted chirp, is designed to be able to precisely identify where the subject is located. It is possible to use only one chirp for each frame, thus not creating a data overhead during the processing phase and also more chirps inside a frame lead to a non-linear sampling of the phase signal. It is important to carefully set the duration of each chirp and the number of them contained in a frame since these values directly impact the sample rate of the HR. The sampling frequency along the slow-time can be written as:

$$f_{sampling[HR]} = \frac{k}{t_{periodicity}}, \tag{3.14}$$

where k is the number of chirps inside one frame and $t_{periodicity}$ represents the frame duration. This equation is similar to equation 3.10 but in this second case the variable k is added. We conduct Experimental tests at the ICT Laboratory of the Polytechnic University of Marche on a set of 15 Caucasian and Asian people of different ages and weights. Radar and GoPro Hero 6 were placed on two tripods, radar at a distance of about 20 cm from the subject's chest and GoPro at about 50 cm from the subject's face. The subjects under test were in a standing position with the back leaning against a wall. The instrumentation used in the measurement setup is depicted in Fig. 3.15. During the video acquisition, the subjects were asked to minimize their movements to avoid noisy signals or face tracking errors. Videos are captured in indoor conditions, hence we used a standard lamp (see Fig. 3.15) in addition to the ceiling light to better illuminate the subjects' faces.
Radar configuration parameters are reported in Tab. 3.6; it is possible to note that the heartbeat of the subject is sampled with a frequency of 20 Hz, which is a much larger value than Nyquist's limit. The obtained Ψ_i is filtered to separate the components related to the HR and to the RR so, after having obtained the phase signal

Figure 3.15: Measurement instrumentation used.

we can filter it in the range of the heartbeat and the respiration, i.e. between 60 beats/min and 150 beats/min. The respiration rate is obtained by filtering Ψ_i with a low pass Finite Impulse Response (FIR) equiripple filter. The values of the filter used for the HR are reported in Tab. 3.7. An example of the obtained signals after the filtering process are depicted inside Fig. 3.16.

Table 3.6: Radar parameters

Parameter	Value
t_{chirp}	15.7 ms
Bandwidth	3.99 GHz
$t_{periodicity}$	50 ms
n° chirps in frame	1
n° samples in chirp	128
$f_{sampling}$	4 MSps
R_{max}	4.2184 m
$f_{samplingHR}$	20 Hz
n° of transmitted chirps	1000
Used TX and RX	TX1/RX1-RX4

In Tab. 3.8 we report the characteristics of the subjects participating to the tests

Table 3.7: Filters parameters for the HR.

Parameter	Value
Filter Type	FIR Equiripple
f_{stop1}	0.8 Hz
f_{pass1}	1.1 Hz
f_{stop2}	2.5 Hz
f_{pass2}	2.8 Hz

and in Tab. 3.9 the results of the corresponding average heartbeat obtained with both the considered methods, radar (indicated as R) and video (V) processing, with respect to values given by Pulse Oximeter (POx).

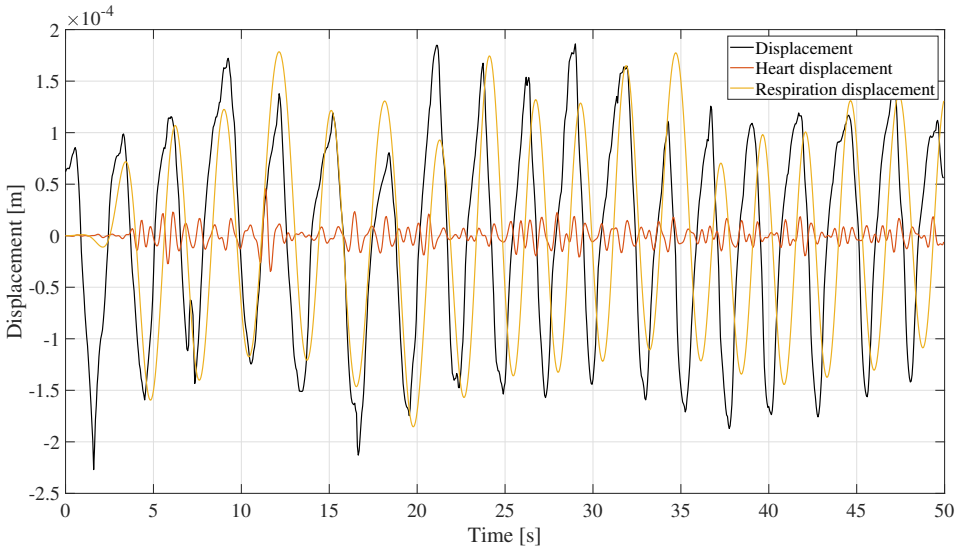

Figure 3.16: Extracted displacements before and after the filtering process.

One of the video techniques used for the comparison is the Eulerian Video Magnification (EVM) who amplifies the skin color, for this reason the subjects' characteristics and ethnicity are described to highlight any possible influence on the HR estimation. In the case of videoplethysmography (VPG) processing, people with beard or make-up may generate a greater error.
The relative percent errors $Er\%$ between different methods shown in Tab. 3.9 are calculated as follows

$$Er\% = \frac{|Ref - A|}{Ref} \cdot 100, \tag{3.15}$$

where Ref is the reference value and A is the value estimated using the contactless approach. The MREs, computed by averaging the relative percentage errors $Er\%$, between Radar and Pulse Oximeter and videoplethysmography (VPG) and Pulse Oximeter, are reported in Tab. 3.10, showing that errors obtained are very similar. The small errors measured also prove that both contactless methods can be used as a valid alternative to the Pulse Oximeter and the results obtained with the automotive radar are in line with the other non-contact technique.

Table 3.8: Characteristics of the subjects under test.

S	Age	Weight	Characteristics
1	22	66	Caucasian
2	22	85	Caucasian, Beard
3	37	75	Caucasian, Make-up
4	28	58	Caucasian, Beard
5	27	54	Caucasian, Make-up
6	26	54	Caucasian
7	37	75	Caucasian, Tanned skin
8	25	74	Caucasian, Beard
9	24	75	Asian
10	25	64	Caucasian
11	45	70	Caucasian
12	31	70	Caucasian, Beard
13	29	63	Caucasian
14	29	63	Caucasian
15	36	58	Caucasian, Make-up
16	29	50	Caucasian

Table 3.9: Tests Results: S is the subject number, V the video result, POx the measured value by the pulse-oximeter, R the value extracted from the radar and $Er_[P-R]\%$ and $Er_[P-V]\%$ the percentage errors.

S	V	POx	R	$\mathbf{Er_{\lvert P-R \rvert}\%}$	$\mathbf{Er_{\lvert P-V \rvert}\%}$
1	77	76	77	1.05	1.32
2	99	102	98.4	3.53	2.94
3	96	93	91	1.94	3.23
4	65	67	70	3.88	2.99
5	61	64	64	0.62	4.69
6	72	73	73	0.27	1.37
7	90	93	92.4	0.65	3.23
8	77	72	71	1.67	6.94
9	74	73	72	1.37	1.37
10	79	81	83	2.22	2.47
11	79	78	79	1.54	1.28
12	103	103	104	0.97	0.00
13	72	72	67	6.67	0.00
14	92	93	82	12.26	1.08
15	81	83	80	3.13	2.41
16	70	71	72	1.41	1.41

The evaluation HR with an FFT is simple and immediate, the highest peak of the spectrum is the result of the measurement. Also, the acquired signal is related to more or less 50 seconds so the obtained value is a mean of the HR during this

Table 3.10: MREs comparison between radar and video processing.

MRE POx-R	MRE POx-V
2.76%	2.35%

time. The main drawback is due to the presence of other multiple FFT peaks ,these can affect the correct evaluation of the HR, for this reason, we choose to use another type of algorithm to calculate the spectrum, this is the MUltiple SIgnal Classification (MUSIC) algorithm and his output is a pseudo spectrum who can be used for the HR calculation. The MUSIC algorithm is commonly used in MIMO radars to improve the angular resolution but this technique can be used also to estimate the main harmonic contributions in a signal [108, 109]. This algorithm is an eigen-based subspace decomposition method and can estimate the frequencies of complex sinusoids observed in additive white noise. We can consider a noisy signal vector y composed of P real sinusoids, we can model the signal as:

$$y = Sa + n \tag{3.16}$$

where:

- $a = [X_1, X_2, \ .... \ , X_P]^T$
- $S = [s_1, s_2, \ .... \ , s_P]$
- $s_k = \left[1, e^{j2\pi f_k}, \ .... \ , e^{j2\pi(N-1)f_k}\right]$

N is the number of samples, f_k is the frequency of the k-th complex sinusoid, X_k is the complex amplitude of k-th sinusoid and n is a zero mean Gaussian white noise vector with variance σ_n^2. To calculate the pseudo-spectrum we need the autocorrelation matrix which is:

$$R_{yy} = E\left[yy^H\right] = R_{xx} + R_{nn} = SAS^H + \sigma_n^2 I \tag{3.17}$$

where E denotes the expected value, H denotes the Hermitian. R_{yy} is a diagonal matrix and, in addition, Rxx and Rnn are the autocorrelation matrices of the signal and noise processes who can be written as:

$$R_{xx} = \sum_{k=1}^{N} \lambda_k v_k v_k^H \tag{3.18}$$

$$R_{nn} = \sigma_n^2 \sum_{k=1}^{N} v_k v_k^H \tag{3.19}$$

where λ_k and v_k are the eigenvalues and eigenvectors of the matrix R_{xx} respectively. The autocorrelation matrix of the noisy signal may be expressed as:

$$R_{yy} = \sum_{k=1}^{N} \lambda_k v_k v_k^H + \sigma_n^2 \sum_{k=1}^{N} v_k v_k^H = \sum_{k=1}^{N} \mu_k v_k v_k^H \tag{3.20}$$

where $\mu_k = \lambda_k + \sigma_n^2$ are the eigenvalues of the matrix R_{yy}. All the eigenvalues are the real numbers and satisfy:

$$\mu_1 \geq \mu_2 \geq, \ \ldots . , \geq \mu_p \geq \mu_{P+1} = \mu_N = \sigma_n^2 \tag{3.21}$$

At the end we can define the pseudo-spectrum $P_{XX}^{MUSIC}(f)$ as:

$$P_{XX}^{MUSIC}(f) = \frac{1}{\sum_{k=P+1}^{N} |s^H(f) v_k|^2} = \frac{1}{S^H(f) V V^H s(f)} \tag{3.22}$$

where $s(f) = [1 e^{j2\pi f}, \ \ldots . , e^{j2\pi(N-1)f}]^T$ is the complex sinuosidal vector and $V = [v_{P+1}, \ \ldots . , v_n]$ is the matrix of the noise subspace. So considering y the phase signal Ψ_i extracted as described in Section 3.1 is possible to calculate a new spectrum and use it for the HR evaluation.
For our specific application, the value of P who provides the better performances is 50 and, in Fig. 3.17 a comparison between the two radar techniques discussed before is depicted. We observe that the two detection algorithms lead to different results. In the case of the FFT, the highest peak corresponds to 64.8 bpm, while in the case of the MUSIC to 74.4 bpm, which represents the correct value. We note that within the FFT spectrum there is a value around 74 bpm. However, this is not the highest peak, and this affects the detection of the correct HR value.

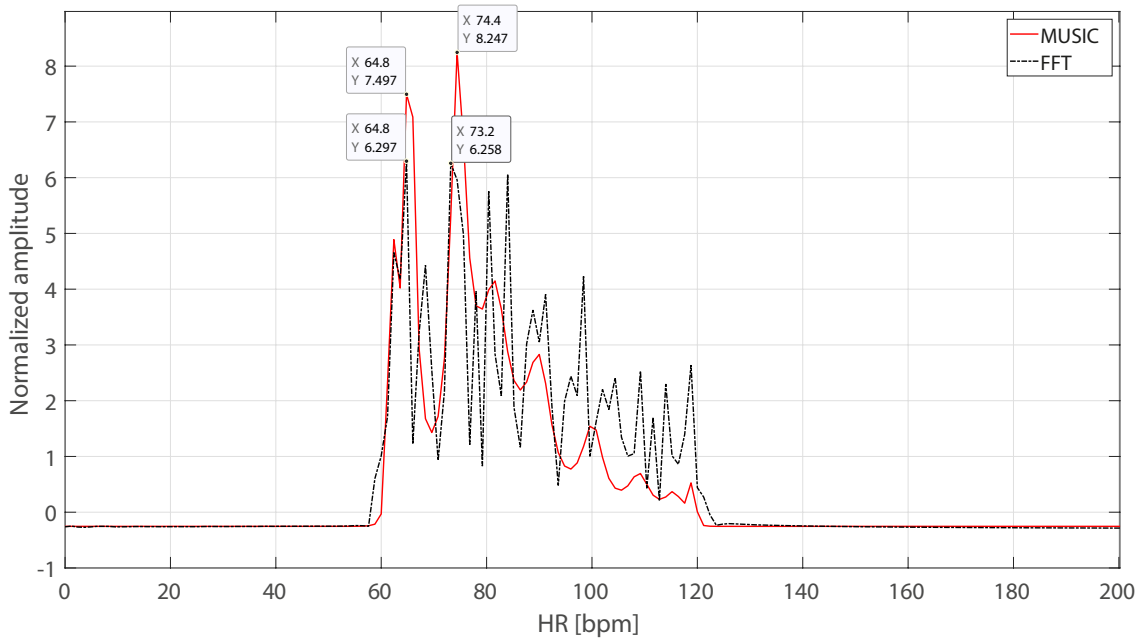

Figure 3.17: Extraction comparison between MUSIC and FFT. The amplitudes are obtained by dividing each value by the maximum of both the methodologies.

To improve the comparison of the performances, in Tab. 3.11 we report the results achieved by different video and radar methodologies, an overview of these video techniques can be found in [110, 111, 112, 113, 114]. Table 3.11 also shows the number of the subjects (indicated by S) who participated in the tests and the results of the average heartbeat (in bpm) obtained with the considered radar and video

methods, with respect to values given by Pulse Oximeter (POx). Regarding the radar techniques, in our comparison we do not consider subjects 13 and 14, since the error is too large. This is probably due to the incorrect position of the radar in front of the subject, which makes it difficult to detect the correct target position inside the Angle - Range map. For the cases of subjects 5, 8, and 15 the value of HR is extracted from the second peak. This problem is also present in the FFT based technique and is a consequence of the filtering process that generates big peaks near the cut frequencies. The application of the MUSIC reduces this effect, so this algorithm improves the performance of the system also from this point of view. It is possible to evaluate the difference Δ between the two techniques considered and the value measured by the pulse oximeter, averaged over the 16 subjects, using the following equation:

$$\Delta_{mean} = \frac{\sum_{n=1}^{N}(POx_n - V_n)}{N}, \tag{3.23}$$

where N is the number of the subjects, POx represents the value detected by the pulse oximeter and V is the value detected by the applied radar technique. The MUSIC algorithm results in a Δ_{MUSIC} of -0.227 [bpm], while the FFT in a Δ_{FFT} of 0.157 [bpm]. The two techniques give similar results, but the MUSIC algorithm allows a easier detection of the peak.

Table 3.11: Tests results on subjects with different physical characteristics. All results are measured in bpm.

S	POx	EVM	ICA(G)	ICA(G)+PCA	ICA+PCA+SD	FFT	MUSIC
1	76	77	72	70	70	77	75.6
2	102	98	98	81	85	98.4	100.8
3	93	98	85	90	91	93.6	91
4	67	64	54	70	57	70	72
5	64	62	70	70	67	64	64.8
6	73	72	72	67	72	73	72
7	93	90	88	76	83	92.4	91.2
8	72	77	67	70	70	71	72
9	73	75	75	90	67	72	70.8
10	81	69	75	90	72	83	81.6
11	78	77	78	79	75	79	80.4
12	103	111	83	104	91	104	103.2
13	72	72	72	70	80	67	/
14	93	95	85	93	93	82	/
15	83	80	80	96	85	80	81.6
16	71	69	70	93	67	73.2	72

In Tab. 3.12 we evaluate the mean relative error (MRE) between different methods, taking as a reference value the one measured by the pulse oximeter. As regards the methods based on video processing, we observe that the EVM method is the most accurate but computationally heavy, as the others video processing techniques. The

radar approach is less accurate but the processing is more simple and the system is not affected by the characteristics of the subjects such as make-up or beard.

Table 3.12: Comparison and percentage error between different methods.

Methods	MRE [%]
POx-EVM	0.55
POx-ICA	6.92
POx-(ICA+PCA)	10.06
POx-(ICA+PCA+SD)	7.71
POx-FFT	2.82
POx-MUSIC	1.86

3.5 Vital parameters estimation with 300 GHz radar sensor: qualitative analysis

As we wrote in section 3.1, the capability of the radar system to detect small vibrations is strictly related to the wavelength and the bandwidth of their transmitted signal. FMCW Radars with more high operating frequency and bandwidth can be found on the market and such sensors work at 300 GHz with around 40 GHz of bandwidth. A device equipped with these features is the Silicon Radar TRA_300_030 who is depicted inside Fig. 3.18.
With this sensor is theoretically possible to detect smaller vibrations with also more resolution in range detection.

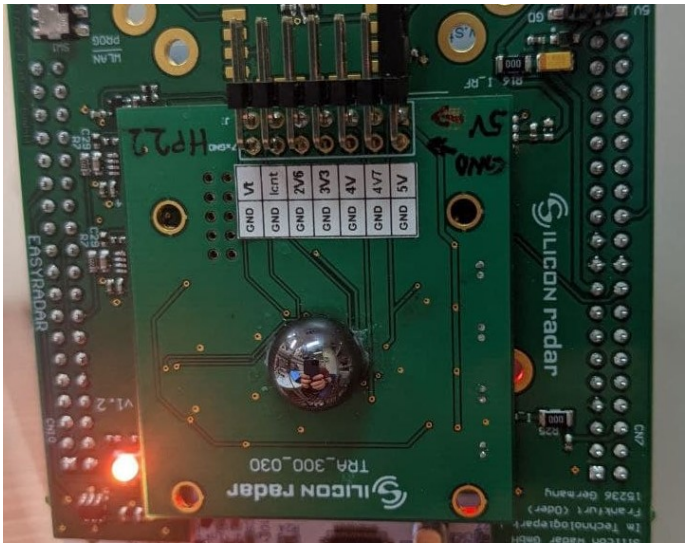

Figure 3.18: 300 GHz radar system.

The raw samples coming from the ADC are transferred by a USB cable and over the same connection, we can send the configuration parameters. The device is also designed to provide some elaborated data, such as the range FFT and the CFAR calculation. These computations result in a non-constant update time of the data: the sensor provides the samples of each chirp sampled according to a nominal frequency, but the time between two chirps changes from one to another. This means that the HR and the RR can be analyzed only along the time.
To validate the capabilities of this device with the proposed signal processing algorithm, we conduct some qualitative experiments, and we test the system in an HR and RR setup. This work can be found in [105] where we compare the results with the AWR1642. The used setup is simple, the subject sitting in front of the radar with the sensor oriented in the direction of the subject's chest. The measurement is performed separately with the two compared sensors. Performing a simultaneous measurement with the two devices is difficult so we decide to perform the measurements separately. The sensors are placed at more or less twenty centimetres from the subject and the configurations are derived also taking into account this distance. The configuration parameters are reported in Tab. 3.13 and Tab. 3.14. The technique used for extracting the vitals parameters are the same described before but, as the 300 GHz sensor is not suited with MIMO, the comparison with the 77 GHz Radar is performed without this technology.

Table 3.13: 77 GHz radar parameters

Parameter	Value
t_{chirp}	15.7 μs
Bandwidth	3.99 GHz
CRT	50 ms
No. chirps in frame	1
No. samples in chirp	128
$f_{sampling}$	4 MSps
R_{max}	4.2184 m
$f_{samplingHR}$	20 Hz

Table 3.14: 300 GHz radar parameters

Parameter	Value
t_{chirp}	503 μs
Bandwidth	4.99 GHz
No. samples in chirp	1024
R_{max}	15.998 m
Distance accuracy	312 mm

As we did before, the phase signal must be filtered to obtain the HR and the RR. In this case, we try to use a different type of filter: we choose an elliptic as this provides less delay. The parameters, both for HR and RR, can be found in Tab. 3.15.

Table 3.15: Used filter parameters

Parameter	RR	HR
Filter Type	Elliptic Bandpass	Elliptic Bandpass
f_{stop1} [Hz]	0.1	0.8
f_{pass1} [Hz]	0.2	1
f_{pass2} [Hz]	0.4	2
f_{stop2} [Hz]	0.8	2.2
Att_{stop1} [dB]	60	60
Att_{pass} [Hz]	1	1
Att_{stop2} [Hz]	80	80

The 300 GHz radar is equipped with a very directive antenna so the capability of the sensor to detect the HR is limited. The chest of the subject must be perpendicular to the sensor orientation and for this reason, we can measure only the respiration. An example of the vital parameters extracted by the two systems can be found in Fig. 3.19a and Fig. 3.19.
From the performed test, the performances of the 300 GHz radar seem to be poor respect the 77 GHz. The main reason in our opinion is the design of the antenna, their extremely directive radiation diagram makes this sensor not suited for this application. The wavelength of the transmitted signal is very interesting as in theory can provide very good performances in terms of vibration detection. So, in the case of vital parameters, where the detection of the heartbeat is very difficult, this device will be able to provide better performances than the 77 GHz. To reach them the sensor needs an accurate design for this particular application and the actual version cannot be used.

3.6 Chapter conclusions

The proposed signal processing technique, coupled with an automotive radar (the AWR1642), can detect very small vibrations who are in the order of 100 microns. This technique works well in applied fields such as building monitoring and person's vital parameters extraction. The comparison with another type of radar that works at a higher frequency and is equipped with more bandwidth can theoretically provide better performances but, from experimental results, we can see how this is not completely true. The 300 GHz sensor shows how the antenna design is fundamental in this application and to obtain good results we need a wider aperture antenna. Speaking about the signal processing technique, this has the main drawback in the detection of the target, this must not move during the measurement. The target must always stand in the same range-angular bin (or range-bin if we do not apply MIMO), otherwise, the technique provides poor results.

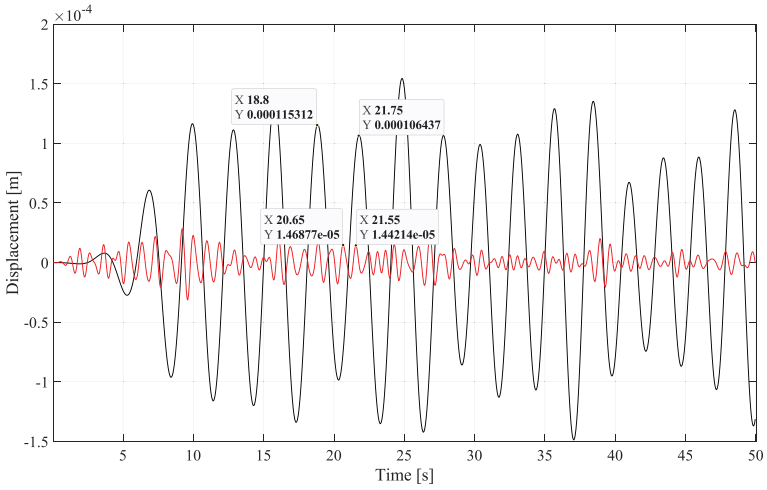

(a)

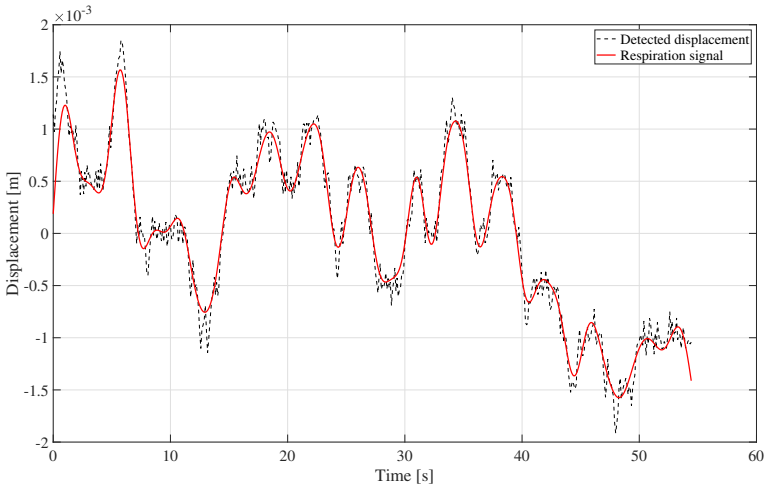

(b)

Figure 3.19: Signals extracted from the phase Ψ_i a) with the 77 GHz radar b) with the 300 GHz radar.

4

Conclusion

The work presented in this thesis shows how modern automotive radars can provide excellent performance not only in the vehicular field. Even if they are designed for a specific use, they can be used to extract micro-Doppler signals with good resolution. Moreover, modern Machine Learning techniques make possible classification operations of such signals with very high performance. In the first part of the thesis, we focused on classifying signals in different contexts. For each of them, a special pipeline has been developed, which is based on appropriate pre-processing. Different classification strategies have been studied and their performance has been validated. The work done shows that with these devices is not always necessary to apply more complex techniques to obtain better performance. It is also shown that the definition of features on radar maps makes it possible to simplify the algorithms, with the advantage of reducing latencies, and not having a loss of performance. This study has been verified in several areas one of which is the identification of drones. In this application, the detection time is critical to take countermeasures.

Instead, the second part of the thesis described the work done in measuring vibration. From the literature, it is known how radar systems can measure the vibrations of objects always exploring the micro-Doppler effect. The capacity of the system is related to the wavelength of the device, so we have validated the performance of the systems at 77 GHz. It has been passed for a part of the job in simulation and validation in the laboratory and subsequently, they have been made some outdoor measures on structures like bridges and viaducts. We then carried out a work of comparison between the capabilities of the radar and a laser vibrometer in order to obtain a numerical error value of the device. This parameter was fundamental in the study of a second application, that of vital signs detection. In this case, the displacement of the chest of the subjects analyzed contains the information of respiration and heartbeat. Therefore, a good detection capability is fundamental to have a good performance. In this case, we chose to compare the measures obtained with the radar with those obtained with video processing and we calculated the error. The performances of the two systems are comparable but the radar can preserve the patient's privacy which is more difficult with the video. In the end, a comparison was made with a 300 GHz radar, but the performances obtained are not satisfactory. The reason seems to be the extreme directivity of the antenna of the 300 GHz radar which does not allow to measure well the displacement of objects that are not perpendicular to it. The micro-movements of the subject, therefore, disturb the measurement and for this reason, better performances are obtained with the 77 GHz radar which has a wider radiation pattern.

In conclusion, the results obtained are in line with what is found in the literature demonstrating the quality of the work done. The algorithms developed are based on a device already available on the market which could be applied to the applications treated.

5

List of Publications

1. Ciattaglia, G., Spinsante, S., Gambi, E. Slow-time mmwave radar vibrometry for drowsiness detection. (2021) 2021 IEEE International Workshop on Metrology for Automotive, MetroAutomotive 2021 - Proceedings, pp. 141-146.

2. Ciattaglia, G., Temperini, G., Spinsante, S., Gambi, E. MmWave radar features extraction of drones for machine learning classification. (2021) 2021 IEEE International Workshop on Metrology for AeroSpace, MetroAeroSpace 2021 - Proceedings, art. no. 9511703, pp. 259-264.

3. Senigagliesi, L., Ricciuti, M., Ciattaglia, G., De Santis, A., Gambi, E. Comparison of Video and Radar Contactless Heart Rate Measurements. (2021) Communications in Computer and Information Science, 1387, pp. 96-113.

4. Ciattaglia, G., De Santis, A., Disha, D., Spinsante, S., Castellini, P., Gambi, E. Performance evaluation of vibrational measurements through mmwave automotive radars† (2021) Remote Sensing, 13 (1), art. no. 98, pp. 1-20.

5. Gambi, E., Ciattaglia, G., De Santis, A., Senigagliesi, L. Millimeter wave radar data of people walking (2020) Data in Brief, 31, art. no. 105996, .

6. Senigagliesi, L., Ciattaglia, G., Gambi, E. Contactless Walking Recognition based on mmWave RADAR Proceedings - IEEE Symposium on Computers and Communications, 2020-July, art. no. 9219565, .

7. Ciattaglia, G., Santis, A.D., Disha, D., Spinsante, S., Castellini, P., Gambi, E. Performance evaluation of vibrational measurements through mmWave radars 2020 IEEE International Workshop on Metrology for AeroSpace, MetroAeroSpace 2020 - Proceedings, art. no. 9160237, pp. 160-165.

8. Senigagliesi, L., Ciattaglia, G., De Santis, A., Gambi, E. People walking classification using automotive radar (2020) Electronics (Switzerland), 9 (4), art. no. 588, .

9. Ricciuti, M., Ciattaglia, G., de Santis, A., Gambi, E., Senigagliesi, L. Contactless heart rate measurements using RGB-camera and radar (2020) ICT4AWE 2020 - Proceedings of the 6th International Conference on Information and Communication Technologies for Ageing Well and e-Health, pp. 115-123.

10. Ciattaglia, G., Senigagliesi, L., De Santis, A., Ricciuti, M. Contactless measurement of physiological parameters (2019) IEEE International Conference on Consumer Electronics - Berlin, ICCE-Berlin, 2019-September, art. no. 8966140, pp. 22-26.

11. Gambi, E., Ciattaglia, G., De Santis, A. People Movement Analysis with Automotive Radar (2019) 2019 IEEE 23rd International Symposium on Consumer Technologies, ISCT 2019, art. no. 8900975, pp. 233-237.

12. Gambi, E., Ciattaglia, G., DE SANTIS, A. Automotive radar application for structural health monitoring (2019) WIT Transactions on the Built Environment, 189, pp. 79-89.

Bibliography

[1] V. Chen, D. Tahmoush, and W. Miceli, "Micro-doppler signatures-review challenges and perspectives," *Radar-Micro Doppler Signatures: Processing and Applications*, pp. 1–25, 2014.

[2] S. Rahman and D. A. Robertson, "Radar micro-doppler signatures of drones and birds at k-band and w-band," *Scientific reports*, vol. 8, no. 1, pp. 1–11, 2018.

[3] S. Yang, S. Yeh, S. Bor, S. Huang, and C. Hwang, "Electromagnetic backscattering from aircraft propeller blades," *IEEE Transactions on Magnetics*, vol. 33, no. 2, pp. 1432–1435, 1997.

[4] J. Martin and B. Mulgrew, "Analysis of the theoretical radar return signal form aircraft propeller blades," in *IEEE International Conference on Radar*. IEEE, 1990, pp. 569–572.

[5] D. P. Fairchild and R. M. Narayanan, "Classification of human motions using empirical mode decomposition of human micro-doppler signatures," *IET Radar, Sonar & Navigation*, vol. 8, no. 5, pp. 425–434, 2014.

[6] F. Fioranelli, M. Ritchie, and H. Griffiths, "Multistatic human micro-doppler classification of armed/unarmed personnel," *IET Radar, Sonar & Navigation*, vol. 9, no. 7, pp. 857–865, 2015.

[7] E. Gambi, G. Ciattaglia, and A. De Santis, "People movement analysis with automotive radar," in *2019 IEEE 23rd International Symposium on Consumer Technologies (ISCT)*. IEEE, 2019, pp. 233–237.

[8] L. Piotrowsky and N. Pohl, "Spatially resolved fast-time vibrometry using ultrawideband fmcw radar systems," *IEEE Transactions on Microwave Theory and Techniques*, vol. 69, no. 1, pp. 1082–1095, 2020.

[9] S. S. Ram, C. Christianson, Y. Kim, and H. Ling, "Simulation and analysis of human micro-dopplers in through-wall environments," *IEEE Transactions on Geoscience and remote sensing*, vol. 48, no. 4, pp. 2015–2023, 2010.

[10] J. L. Geisheimer, E. F. Greneker III, and W. S. Marshall, "High-resolution doppler model of the human gait," in *Radar Sensor Technology and Data Visualization*, vol. 4744. International Society for Optics and Photonics, 2002, pp. 8–18.

[11] F. Fioranelli, O. Krasnov, Y. Cai, A. Yarovoy, J. Yun, and D. Anderson, "Improving the simulations of radar signatures of small drone," 2021.

[12] "Sae levels of driving automation™ refined for clarity and international audience." [Online]. Available: https://www.sae.org/blog/sae-j3016-update

[13] S. S. Shadrin and A. A. Ivanova, "Analytical review of standard sae j3016 «taxonomy and definitions for terms related to driving automation systems

for on-road motor vehicles» with latest updates," *Avtomobil'. Doroga. Infrastruktura.*, no. 3 (21), p. 10, 2019.

[14] A. Herrmann, W. Brenner, and R. Stadler, *Autonomous driving: how the driverless revolution will change the world*. Emerald Group Publishing, 2018.

[15] "Etsi en 302 264-1." [Online]. Available: https://www.etsi.org/deliver/etsi_en/302200_302299/30226401/01.01.01_60/en_30226401v010101p.pdf

[16] J. Gamba, *Radar signal processing for autonomous driving*. Springer, 2020.

[17] M. I. Skolnik, "Introduction to radar," *Radar handbook*, vol. 2, p. 21, 1962.

[18] J. Hasch, E. Topak, R. Schnabel, T. Zwick, R. Weigel, and C. Waldschmidt, "Millimeter-wave technology for automotive radar sensors in the 77 ghz frequency band," *IEEE Transactions on Microwave Theory and Techniques*, vol. 60, no. 3, pp. 845–860, 2012.

[19] S. M. Patole, M. Torlak, D. Wang, and M. Ali, "Automotive radars: A review of signal processing techniques," *IEEE Signal Processing Magazine*, vol. 34, no. 2, pp. 22–35, 2017.

[20] H. Rohling, F. Fölster, M.-M. Meinecke, and R. Mende, "A new generation of automotive radar waveform design techniques," in *2004 International Waveform Diversity & Design Conference*. IEEE, 2004, pp. 1–5.

[21] W. Wang, J. Du, and J. Gao, "Multi-target detection method based on variable carrier frequency chirp sequence," *Sensors*, vol. 18, no. 10, p. 3386, 2018.

[22] L. Ghattas, S. Méric, and C. Brousseau, "Performance assessment of fmcw radar processing for transponder identification," in *2016 European Radar Conference (EuRAD)*. IEEE, 2016, pp. 258–261.

[23] Q. Guoqing, "High accuracy range estimation of fmcw level radar based on the phase of the zero-padded fft," in *Proceedings 7th International Conference on Signal Processing, 2004. Proceedings. ICSP'04. 2004.*, vol. 3. IEEE, 2004, pp. 2078–2081.

[24] J. Svensson, "High resolution frequency estimation in an fmcw radar application," 2018.

[25] A. Wojtkiewicz, J. Misiurewicz, M. Nalecz, K. Jedrzejewski, and K. Kulpa, "Two-dimensional signal processing in fmcw radars," *Proc. XX KKTOiUE*, pp. 475–480, 1997.

[26] M. Song, J. Lim, and D.-J. Shin, "The velocity and range detection using the 2d-fft scheme for automotive radars," in *2014 4th IEEE International Conference on Network Infrastructure and Digital Content*. IEEE, 2014, pp. 507–510.

[27] D. K. Barton, *Radar system analysis and modeling*. Artech House, 2004.

[28] G. Ciattaglia, A. De Santis, D. Disha, S. Spinsante, P. Castellini, and E. Gambi, "Performance evaluation of vibrational measurements through mmwave automotive radars," *Remote Sensing*, vol. 13, no. 1, p. 98, 2021.

[29] S. Sun, A. P. Petropulu, and H. V. Poor, "Mimo radar for advanced driver-assistance systems and autonomous driving: Advantages and challenges," *IEEE Signal Processing Magazine*, vol. 37, no. 4, pp. 98–117, 2020.

[30] "Mimo radar." [Online]. Available: https://www.ti.com/lit/an/swra554a/swra554a.pdf?ts=1637679579950&ref_url=https%253A%252F%252Ft.co%252F

[31] F. Belfiori, W. van Rossum, and P. Hoogeboom, "2d-music technique applied to a coherent fmcw mimo radar," in *IET International Conference on Radar Systems (Radar 2012)*. IET, 2012, pp. 1–6.

[32] V. Krishnaveni, T. Kesavamurthy, and B. Aparna, "Beamforming for direction-of-arrival (doa) estimation-a survey," *International Journal of Computer Applications*, vol. 61, no. 11, 2013.

[33] S. Kim, D. Oh, and J. Lee, "Joint dft-esprit estimation for toa and doa in vehicle fmcw radars," *IEEE Antennas and Wireless Propagation Letters*, vol. 14, pp. 1710–1713, 2015.

[34] M. A. Richards, *Fundamentals of radar signal processing*. McGraw-Hill Education, 2014.

[35] X. Gao, G. Xing, S. Roy, and H. Liu, "Experiments with mmwave automotive radar test-bed," in *2019 53rd Asilomar Conference on Signals, Systems, and Computers*. IEEE, 2019, pp. 1–6.

[36] S. Li, X. Bi, L. Huang, and B. Tan, "2-d cfar procedure of multiple target detection for automotive radar," *SAE International Journal of Passenger Cars-Electronic and Electrical Systems*, vol. 11, no. 1, pp. 65–74, 2018.

[37] J. Wang, "Cfar-based interference mitigation for fmcw automotive radar systems," *arXiv preprint arXiv:2101.01257*, 2021.

[38] G. T. Capraro, A. Farina, H. Griffiths, and M. C. Wicks, "Knowledge-based radar signal and data processing: a tutorial review," *IEEE Signal Processing Magazine*, vol. 23, no. 1, pp. 18–29, 2006.

[39] "Awr1642, single-chip 76-ghz to 81-ghz automotive radar sensor integrating dsp and mcu." [Online]. Available: https://www.ti.com/product/AWR1642

[40] "Dca1000evm data capture card." [Online]. Available: https://www.ti.com/lit/ug/spruij4a/spruij4a.pdf?ts=1637756157640&ref_url=https%253A%252F%252Fwww.ti.com%252Ftool%252FDCA1000EVM

[41] "Mmwave-studio." [Online]. Available: https://www.ti.com/tool/MMWAVE-STUDIO

[42] C. Aydogdu, N. Garcia, L. Hammarstrand, and H. Wymeersch, "Radar communications for combating mutual interference of fmcw radars," in *2019 IEEE Radar Conference (RadarConf)*, 2019, pp. 1–6.

[43] Y. Wang, Q. Liu, and A. E. Fathy, "Cw and pulse–doppler radar processing based on fpga for human sensing applications," *IEEE Transactions on Geoscience and Remote Sensing*, vol. 51, no. 5, pp. 3097–3107, 2012.

[44] Y. S. Koo, L. Ren, Y. Wang, and A. E. Fathy, "Uwb microdoppler radar for human gait analysis, tracking more than one person, and vital sign detection of moving persons," in *2013 IEEE MTT-S International Microwave Symposium Digest (MTT)*. IEEE, 2013, pp. 1–4.

[45] R. Trommel, R. Harmanny, L. Cifola, and J. Driessen, "Multi-target human gait classification using deep convolutional neural networks on micro-doppler spectrograms," in *2016 European Radar Conference (EuRAD)*. IEEE, 2016, pp. 81–84.

[46] H. G. Doherty, R. A. Burgueño, R. P. Trommel, V. Papanastasiou, and R. I. Harmanny, "Attention-based deep learning networks for identification of hu-

man gait using radar micro-doppler spectrograms," *International Journal of Microwave and Wireless Technologies*, vol. 13, no. 7, pp. 734–739, 2021.

[47] S. K. Mitra and Y. Kuo, *Digital signal processing: a computer-based approach*. McGraw-Hill New York, 2006, vol. 2.

[48] L. Cohen, *Time-frequency analysis*. Prentice hall, 1995, vol. 778.

[49] I. T. Jolliffe and J. Cadima, "Principal component analysis: a review and recent developments," *Philosophical Transactions of the Royal Society A: Mathematical, Physical and Engineering Sciences*, vol. 374, no. 2065, p. 20150202, 2016.

[50] R. Bro and A. K. Smilde, "Principal component analysis," *Analytical methods*, vol. 6, no. 9, pp. 2812–2831, 2014.

[51] S. Wold, K. Esbensen, and P. Geladi, "Principal component analysis," *Chemometrics and intelligent laboratory systems*, vol. 2, no. 1-3, pp. 37–52, 1987.

[52] L. Van der Maaten and G. Hinton, "Visualizing data using t-sne." *Journal of machine learning research*, vol. 9, no. 11, 2008.

[53] X. Wu, V. Kumar, J. R. Quinlan, J. Ghosh, Q. Yang, H. Motoda, G. J. McLachlan, A. Ng, B. Liu, S. Y. Philip *et al.*, "Top 10 algorithms in data mining," *Knowledge and information systems*, vol. 14, no. 1, pp. 1–37, 2008.

[54] J. C. Bezdek, S. K. Chuah, and D. Leep, "Generalized k-nearest neighbor rules," *Fuzzy Sets and Systems*, vol. 18, no. 3, pp. 237–256, 1986.

[55] K.-R. Muller, S. Mika, G. Ratsch, K. Tsuda, and B. Scholkopf, "An introduction to kernel-based learning algorithms," *IEEE transactions on neural networks*, vol. 12, no. 2, pp. 181–201, 2001.

[56] E. Gambi, G. Ciattaglia, A. De Santis, and L. Senigagliesi, "Millimeter wave radar data of people walking," *Data in brief*, vol. 31, p. 105996, 2020.

[57] L. Senigagliesi, G. Ciattaglia, A. De Santis, and E. Gambi, "People walking classification using automotive radar," *Electronics*, vol. 9, no. 4, p. 588, 2020.

[58] J. Bryan, J. Kwon, N. Lee, and Y. Kim, "Application of ultra-wide band radar for classification of human activities," *IET Radar, Sonar & Navigation*, vol. 6, no. 3, pp. 172–179, 2012.

[59] S. Björklund, H. Petersson, and G. Hendeby, "Features for micro-doppler based activity classification," *IET radar, sonar & navigation*, vol. 9, no. 9, pp. 1181–1187, 2015.

[60] L. Senigagliesi, G. Ciattaglia, and E. Gambi, "Contactless walking recognition based on mmwave radar," in *2020 IEEE Symposium on Computers and Communications (ISCC)*. IEEE, 2020, pp. 1–4.

[61] K. Simonyan and A. Zisserman, "Very deep convolutional networks for large-scale image recognition," *arXiv preprint arXiv:1409.1556*, 2014.

[62] M. Mahdianpari, B. Salehi, M. Rezaee, F. Mohammadimanesh, and Y. Zhang, "Very deep convolutional neural networks for complex land cover mapping using multispectral remote sensing imagery," *Remote Sensing*, vol. 10, no. 7, p. 1119, 2018.

[63] S. L. Rabano, M. K. Cabatuan, E. Sybingco, E. P. Dadios, and E. J. Calilung, "Common garbage classification using mobilenet," in *2018 IEEE 10th International Conference on Humanoid, Nanotechnology, Information Technol-*

ogy, Communication and Control, Environment and Management (HNICEM). IEEE, 2018, pp. 1–4.

[64] http://https://www.image-net.org/.

[65] P. Maji and R. Mullins, "On the reduction of computational complexity of deep convolutional neural networks," *Entropy*, vol. 20, no. 4, p. 305, 2018.

[66] H. González-Jorge, J. Martínez-Sánchez, M. Bueno, Arias, and Pedor, "Unmanned aerial systems for civil applications: A review," *Drones*, vol. 1, no. 1, 2017. [Online]. Available: https://www.mdpi.com/2504-446X/1/1/2

[67] "Master list of drone laws (organized by state & country)." [Online]. Available: https://uavcoach.com/drone-laws/

[68] J.-P. Yaacoub, H. Noura, O. Salman, and A. Chehab, "Security analysis of drones systems: Attacks, limitations, and recommendations," *Internet of Things*, vol. 11, p. 100218, 2020. [Online]. Available: https://www.sciencedirect.com/science/article/pii/S2542660519302112

[69] P. Zhang, L. Yang, G. Chen, and G. Li, "Classification of drones based on micro-doppler signatures with dual-band radar sensors," in *2017 Progress in Electromagnetics Research Symposium-Fall (PIERS-FALL)*. IEEE, 2017, pp. 638–643.

[70] F. Fioranelli, M. Ritchie, H. Griffiths, and H. Borrion, "Classification of loaded/unloaded micro-drones using multistatic radar," *Electronics Letters*, vol. 51, no. 22, pp. 1813–1815, 2015.

[71] A. Coluccia, G. Parisi, and A. Fascista, "Detection and classification of multirotor drones in radar sensor networks: A review," *Sensors*, vol. 20, no. 15, p. 4172, 2020.

[72] G. Ciattaglia, G. Temperini, S. Spinsante, and E. Gambi, "mmwave radar features extraction of drones for machine learning classification," in *2021 IEEE 8th International Workshop on Metrology for AeroSpace (MetroAeroSpace)*. IEEE, 2021, pp. 259–264.

[73] A. Chovancová, T. Fico, Ľuboš Chovanec, and P. Hubinsk, "Mathematical modelling and parameter identification of quadrotor (a survey)," *Procedia Engineering*, vol. 96, pp. 172–181, 2014, modelling of Mechanical and Mechatronic Systems. [Online]. Available: https://www.sciencedirect.com/science/article/pii/S1877705814031981

[74] H. M. Hashemian, "State-of-the-art predictive maintenance techniques," *IEEE Transactions on Instrumentation and Measurement*, vol. 60, no. 1, pp. 226–236, 2011.

[75] K. Faulkner, J. M. W. Brownjohn, Y. Wang, and F. Huseynov, "Tracking bridge tilt behaviour using sensor fusion techniques," *Journal of Civil Structural Health Monitoring*, vol. 10, no. 4, pp. 543–555, 2020.

[76] K.-S. Son, H.-S. Jeon, G.-S. Chae, J.-S. Park, and S.-O. Kim, "A fast high-resolution vibration measurement method based on vision technology for structures," *Nuclear Engineering and Technology*, vol. 53, no. 1, pp. 294–303, 2021. [Online]. Available: https://www.sciencedirect.com/science/article/pii/S1738573320303260

[77] F. Pérez, B. Santhanam, T. Atwood, R. Dunkel, A. W. Doerry, and M. M. Hayat, "Detection of vibrating objects in sar images," in *Radar Sensor Tech-*

nology XXIII, vol. 11003. International Society for Optics and Photonics, 2019, p. 110030P.

[78] M. Liu, K.-l. Ding, X. Liu, and Z. Song, "High-speed railway bridge dynamic measurement based on gb-insar technology," in *International Conference on Intelligent Earth Observing and Applications 2015*, vol. 9808. International Society for Optics and Photonics, 2015, p. 98083C.

[79] O. Monserrat, M. Crosetto, and G. Luzi, "A review of ground-based sar interferometry for deformation measurement," *ISPRS Journal of Photogrammetry and Remote Sensing*, vol. 93, pp. 40–48, 2014. [Online]. Available: https://www.sciencedirect.com/science/article/pii/S0924271614000884

[80] M. Pieraccini, N. Casagli, G. Luzi, D. Tarchi, D. Mecatti, L. Noferini, and C. Atzeni, "Landslide monitoring by ground-based radar interferometry: a field test in valdarno (italy)," *International Journal of Remote Sensing*, vol. 24, no. 6, pp. 1385–1391, 2003.

[81] D. Tarchi, N. Casagli, R. Fanti, D. D. Leva, G. Luzi, A. Pasuto, M. Pieraccini, and S. Silvano, "Landslide monitoring by using ground-based sar interferometry: an example of application to the tessina landslide in italy," *Engineering Geology*, vol. 68, no. 1, pp. 15–30, 2003, remote sensing and monitoring of landslides. [Online]. Available: https://www.sciencedirect.com/science/article/pii/S0013795202001965

[82] J. B. Campbell, F. Pérez, Q. Wang, B. Santhanam, R. Dunkel, A. W. Doerry, T. Atwood, and M. M. Hayat, "Remote vibration estimation using displaced-phase-center antenna sar for strong clutter environments," *IEEE Transactions on Geoscience and Remote Sensing*, vol. 56, no. 5, pp. 2735–2747, 2018.

[83] T. Sparr and B. Krane, "Micro-doppler analysis of vibrating targets in sar," *IEE Proceedings-Radar, Sonar and Navigation*, vol. 150, no. 4, pp. 277–283, 2003.

[84] L. Piotrowsky, J. Siska, C. Schweer, and N. Pohl, "Using fmcw radar for spatially resolved intra-chirp vibrometry in the audio range," in *2020 IEEE/MTT-S International Microwave Symposium (IMS)*. IEEE, 2020, pp. 791–794.

[85] J.-M. Muñoz-Ferreras, J. Wang, Z. Peng, C. Li, and R. Gómez-García, "Fmcw-radar-based vital-sign monitoring of multiple patients," in *2019 IEEE MTT-S International Microwave Biomedical Conference (IMBioC)*, vol. 1. IEEE, 2019, pp. 1–3.

[86] M. He, Y. Nian, and Y. Gong, "Novel signal processing method for vital sign monitoring using fmcw radar," *Biomedical Signal Processing and Control*, vol. 33, pp. 335–345, 2017.

[87] G. Ciattaglia, L. Senigagliesi, A. De Santis, and M. Ricciuti, "Contactless measurement of physiological parameters," in *2019 IEEE 9th International Conference on Consumer Electronics (ICCE-Berlin)*. IEEE, 2019, pp. 22–26.

[88] C. Li, J. Cummings, J. Lam, E. Graves, and W. Wu, "Radar remote monitoring of vital signs," *IEEE Microwave Magazine*, vol. 10, no. 1, pp. 47–56, 2009.

[89] E. Gambi, G. Ciattaglia, and A. De Santis, "Automotive radar application for structural health monitoring," *WIT Transactions on The Built Environment*, vol. 189, pp. 79–89, 2019.

[90] A. Broquetas, A. Aguasca, A. Martinez, and R. Tomás, "Structural health monitoring with 94 ghz radar," in *IGARSS 2018-2018 IEEE International Geoscience and Remote Sensing Symposium*. IEEE, 2018, pp. 7982–7985.

[91] R. E. Alva Bañuelos, J. R. González Drigo, G. Luzi, J. O. Caselles Magallón, L. Pujades Beneit, Y. F. Vargas Alzate, and L. Pinzón Ureña, "Remote ambient vibration measurements with real aperture radar to estimate buildings dynamic properties," in *COMPDYN 2019: Computational Methods in Structural Dynamics and Earthquake Engineering: proceedings of the 7th International Conference on Computational Methods in Structural Dynamics and Earthquake Engineering held in Crete, Greece 24-26 June 2019*. Institute of Structural Analysis and Antiseismic Research School of Civil ..., 2019, pp. 1797–1808.

[92] T. Nakagawa, A. Hyodo, K. Kogo, H. Kurata, K. Osada, and S. Oho, "Contactless liquid-level measurement with frequency-modulated millimeter wave through opaque container," *IEEE Sensors Journal*, vol. 13, no. 3, pp. 926–933, 2012.

[93] A. Prabhakara, V. Singh, S. Kumar, and A. Rowe, "Osprey: a mmwave approach to tire wear sensing," in *Proceedings of the 18th International Conference on Mobile Systems, Applications, and Services*, 2020, pp. 28–41.

[94] F. Coppi, C. Gentile, and P. Paolo Ricci, "A software tool for processing the displacement time series extracted from raw radar data," in *AIP Conference Proceedings*, vol. 1253, no. 1. American Institute of Physics, 2010, pp. 190–201.

[95] H. Kim and J. Jeong, "Non-contact measurement of human respiration and heartbeat using w-band doppler radar sensor," *Sensors*, vol. 20, no. 18, p. 5209, 2020.

[96] J. Moll, K. Bechtel, B. Hils, and V. Krozer, "Mechanical vibration sensing for structural health monitoring using a millimeter-wave doppler radar sensor," in *EWSHM-7th European Workshop on Structural Health Monitoring*, 2014.

[97] N. Malešević, V. Petrović, M. Belić, C. Antfolk, V. Mihajlović, and M. Janković, "Contactless real-time heartbeat detection via 24 ghz continuous-wave doppler radar using artificial neural networks," *Sensors*, vol. 20, no. 8, p. 2351, 2020.

[98] M. Nosrati and N. Tavassolian, "Accurate doppler radar-based cardiopulmonary sensing using chest-wall acceleration," *IEEE Journal of Electromagnetics, RF and Microwaves in Medicine and Biology*, vol. 3, no. 1, pp. 41–47, 2018.

[99] Y. Xiong, Z. Peng, G. Xing, W. Zhang, and G. Meng, "Accurate and robust displacement measurement for fmcw radar vibration monitoring," *IEEE Sensors Journal*, vol. 18, no. 3, pp. 1131–1139, 2017.

[100] A.-J. Jang, I.-S. Lee, and J.-R. Yang, "Vital signal detection using multi-radar for reductions in body movement effects," *Sensors*, vol. 21, no. 21, p. 7398, 2021.

[101] C. Gouveia, J. Vieira, and P. Pinho, "A review on methods for random motion detection and compensation in bio-radar systems," *Sensors*, vol. 19, no. 3, p. 604, 2019.

[102] P. Pierleoni, S. Marzorati, C. Ladina, S. Raggiunto, A. Belli, L. Palma, M. Cattaneo, and S. Valenti, "Performance evaluation of a low-cost sensing unit for seismic applications: field testing during seismic events of 2016-2017 in central italy," *IEEE Sensors Journal*, vol. 18, no. 16, pp. 6644–6659, 2018.

[103] L. Ding, M. Ali, S. Patole, and A. Dabak, "Vibration parameter estimation using fmcw radar," in *2016 IEEE International Conference on Acoustics, Speech and Signal Processing (ICASSP)*. IEEE, 2016, pp. 2224–2228.

[104] E. Schires, P. Georgiou, and T. S. Lande, "Vital sign monitoring through the back using an uwb impulse radar with body coupled antennas," *IEEE transactions on biomedical circuits and systems*, vol. 12, no. 2, pp. 292–302, 2018.

[105] G. Ciattaglia, S. Spinsante, and E. Gambi, "Slow-time mmwave radar vibrometry for drowsiness detection," in *2021 IEEE International Workshop on Metrology for Automotive (MetroAutomotive)*. IEEE, 2021, pp. 141–146.

[106] L. Senigagliesi, M. Ricciuti, G. Ciattaglia, A. D. Santis, and E. Gambi, "Comparison of video and radar contactless heart rate measurements," in *International Conference on Information and Communication Technologies for Ageing Well and e-Health*. Springer, 2020, pp. 96–113.

[107] H. Lee, B.-H. Kim, J.-K. Park, and J.-G. Yook, "A novel vital-sign sensing algorithm for multiple subjects based on 24-ghz fmcw doppler radar," *Remote Sensing*, vol. 11, no. 10, p. 1237, 2019.

[108] T. Murakami and Y. Ishida, "Fundamental frequency estimation of speech signals using music algorithm," *Acoustical Science and Technology*, vol. 22, no. 4, pp. 293–298, 2001.

[109] X. Sun and L. Sun, "Harmonic frequency estimation based on modified-music algorithm in power system," *The Open Electrical & Electronic Engineering Journal*, vol. 9, no. 1, 2015.

[110] C. Wang, T. Pun, and G. Chanel, "A comparative survey of methods for remote heart rate detection from frontal face videos," *Frontiers in bioengineering and biotechnology*, vol. 6, p. 33, 2018.

[111] E. Gambi, M. Ricciuti, and S. Spinsante, "Sensitivity of the contactless videoplethysmography-based heart rate detection to different measurement conditions," in *2018 26th European Signal Processing Conference (EUSIPCO)*. IEEE, 2018, pp. 767–771.

[112] S. Spinsante, M. Ricciuti, and L. Scalise, "Contactless measurement of heart rate for exergames applications," in *2018 IEEE International Symposium on Medical Measurements and Applications (MeMeA)*. IEEE, 2018, pp. 1–6.

[113] K. Mannapperuma, B. D. Holton, P. J. Lesniewski, and J. C. Thomas, "Performance limits of ica-based heart rate identification techniques in imaging photoplethysmography," *Physiological measurement*, vol. 36, no. 1, p. 67, 2014.

[114] H. Rahman, M. U. Ahmed, and S. Begum, "Non-contact heart rate monitoring using lab color space." in *pHealth*, 2016, pp. 46–53.

UNIVERSITÀ
POLITECNICA
DELLE MARCHE